

10
Research Summary 36-2,
Vol. I, Part 2.
1 Feb - 1 Apr, 1960

W
68P

SN-32926-5

NASA - CR - 51024

AN68 85326
code 5

Research Summary No. 36-2 Volume I, Part Two

for the period February 1, 1960 to April 1, 1960



JET PROPULSION LABORATORY
CALIFORNIA INSTITUTE OF TECHNOLOGY
PASADENA, CALIFORNIA

April 15, 1960

SINGLE COPY ONLY CASE FILE COPY

NATIONAL AERONAUTICS AND SPACE ADMINISTRATION

(*NASA* CONTRACT NO. NASW-6)

T
Research Summary No. 36-2
Volume I, Part Two³

for the period February 1, 1960 to April 1, 1960

(*NASA CR-51024*)

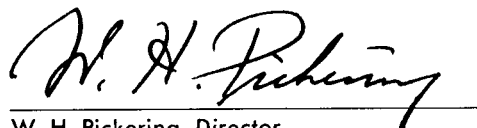


JET PROPULSION LABORATORY
CALIFORNIA INSTITUTE OF TECHNOLOGY
PASADENA, CALIFORNIA

auth April 15, 1960 *68 p* *ref*

Preface

The *Research Summary* is a report of supporting research and development activities at the Jet Propulsion Laboratory, California Institute of Technology. This bimonthly periodical is issued in two volumes. *Volume I, Part One*, contains unclassified information concerning the deep space instrumentation facilities, spacecraft communication techniques, satellite and interplanetary trajectories, and guidance and control techniques. *Volume I, Part Two*, contains unclassified information on instrumentation, computers, materials, propulsion techniques, gas dynamics, physics and mathematics. *Volume II* contains the information classified Confidential about propulsion systems and wind tunnel development testing.



W. H. Pickering, Director
Jet Propulsion Laboratory

Copyright © 1960
Jet Propulsion Laboratory
California Institute of Technology

Contents

I. Instrument Development	1
A. Strain-Gage Measurement of Venturi-Throat Pressure	1
II. Computer Research	3
A. Numerical Analysis	3
B. Orbit Computation Methods	3
III. Materials Research	6
A. Solid State	6
B. Ceramics	7
C. Graphite	9
D. Nozzle and Endothermal Materials	10
E. Pressure Vessel Materials	11
IV. Space Environment Simulation	14
V. Solid Propellant Propulsion	16
A. Basic Investigations of Resin Binders	16
B. Thrust Vector Control of Solid Propellant Rockets	21
C. Materials Evaluation for Solid Propellant Rockets	23
VI. Liquid Propellant Propulsion	28
A. Combustion and Injection	28
B. Thrust Chambers	42
C. Heat Transfer and Fluid Mechanics	44
VII. Gas Dynamics Research	51
A. Stability of Compressible Laminar Boundary Layer	51
B. New Method to Measure Sphere Drag in Rarefied Supersonic Gas Flows	51
C. Stability of One-Dimensional Flow of a Real Continuous Fluid	54
VIII. Hypersonic Wind Tunnel	55
IX. Physics Research	58
A. Upper Atmosphere Reactions	58
B. Efficiency of Fission Electric Cell	60
C. Physics of Rotating Plasmas	61
References	63

I. INSTRUMENT DEVELOPMENT

A. Strain-Gage Measurement of Venturi Throat Pressure

Propellant flow measurements in the rocket-motor injector research program are being made by use of venturi meters in which electrical differential-pressure transducers are used to measure the pressure difference between the venturi throat and the closely adjacent propellant tank. These flow measurements have frequently shown large fluctuations which are not believed to be representative of actual flow variations, and which have been attributed either to the sensitivity of the transducers to acceleration, or to the effect of the venturi ports, manifolding, and relatively long transducer connecting lines in producing false responses in the transducer output. The transducer output data are also used to obtain measurements of average flow rate, but the correct average is difficult to obtain because it is uncertain whether the recorded fluctuations really represent flow oscillations.

Since the average flow rates are also obtainable from turbine flowmeters installed downstream of the venturi meters in the same propellant lines, an attempt is being made to extend the frequency response range of the venturi pressure measurements in order better to determine the existence and nature of the flow fluctuations,

even if this substantially reduces the accuracy of the average flow rate measurements obtained from the venturis. The venturi meter now being developed has a large area ratio with a throat consisting of a thin-walled steel spool sealed to the contracting and expanding sections of the meter by Neoprene O-rings (Figs 1 and 2). A circumferential average of the throat pressure is measured by use of axial and longitudinal strain gages cemented to the spool. The Kel-F rings used initially required excessive axial loading in order to seal satisfactorily, whereas the Neoprene rings seal satisfactorily at 3% of this value. A rigid support structure prevents transmission of propellant line stresses and vibrations to the spool.

At nominal flow rates, the throat static pressure of the present venturi is about 300 psi below tank pressure, a pressure drop about 10 times larger than the usual drop in metering applications. This provides for a reasonably accurate differential pressure measurement when taking the difference in readings between the tank pressure transducer and the throat pressure measured by strain gages. It may also be practicable to make a differential-pressure recording directly from the two transducer outputs by suitable adjustment of the relative transducer sensitivities (by adjustment of excitation voltages, for example) and the use of a high-response differential amplifier. However, the possibility of using a differential

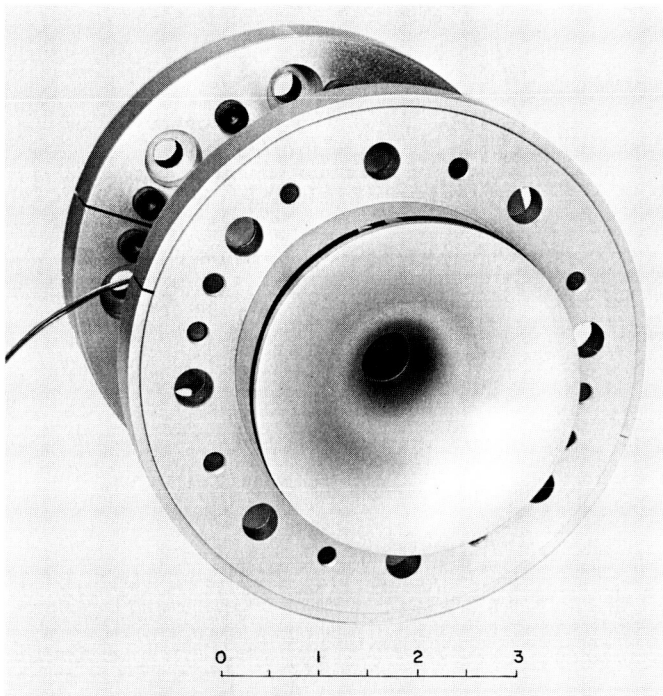


Figure 1. Venturi meter entrance section

strain gage transducer in which one half-bridge is located at the propellant tank and the other is located at the venturi throat does not appear promising, at least from the standpoint of accurate average measurements, because the separately located half-bridges must be equalized both in their sensitivity to applied pressure and to temperature changes. The latter requirement appears difficult to satisfy, since the mechanical restraints and temperatures of the two transducer sections will probably be different. The high value of zero-shift of the

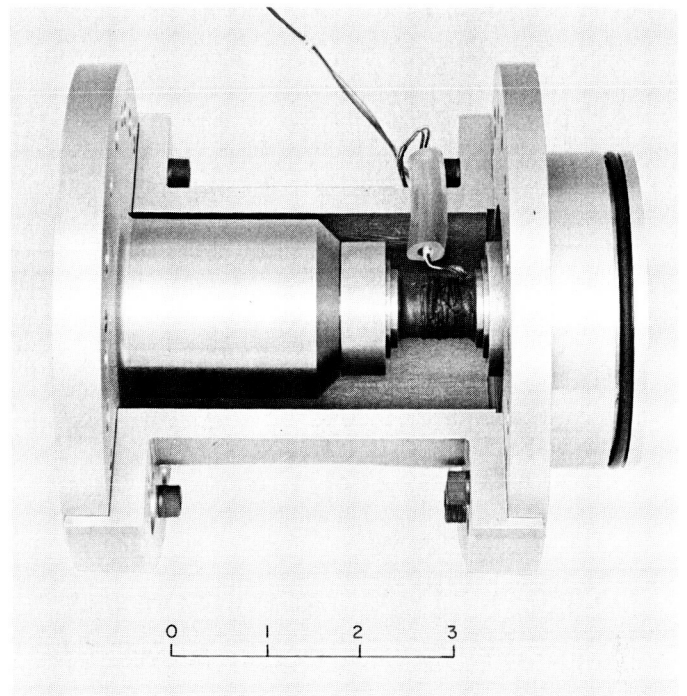


Figure 2. Venturi meter showing spool and strain gages for measuring throat pressure

half-bridge strain gage installation now used for throat pressure measurement, caused by temperature drift and possible mechanical interferences, is expected to be reduced by using a full 4-arm bridge on the spool and by increasing the clearances between the spool and venturi body.

The flow coefficient for the first venturi has been determined from water flow tests and calibrations of the strain gage system with direct pressures, but it has not yet been used in a rocket engine static test.

II. COMPUTER RESEARCH

A. Numerical Analysis

An investigation into the control of certain recurrence systems under a certain criterion has been completed (RS 36-1). The results are presented below in abstract form.

The asymptotic behavior of a particular class of control systems was studied, with particular emphasis being placed on the questions of convergence and the steady-state forms of the loss function and of the system itself. The class referred to above is the class of linear, first-order matrix difference equations with quadratic loss criterion, symbolized by S, where S is represented mathematically by the equations

$$X_{n+1} = AX_n + Y_n \quad X_1 = C \quad n = 1, 2, \dots, N \quad (1a)$$

$$L_N(C, Y) = \sum_{n=1}^N X_n' X_n + \delta \sum_{n=1}^N Y_n' Y_n \quad \delta > 0 \quad (1b)$$

S is also referred to as an N-stage process.

To clarify the notation, (1) X_n is a $p \times 1$ vector which denotes the state of the system at step n . That is, S is described by p components, and the i th component, X_{in} , of X_n , $n = 1, 2, \dots, N$, denotes the state of the i th component of S on step n ; (2) A is a $p \times p$ constant matrix; (3) Y_n is a $p \times 1$ vector which denotes the amount of control that

will be forced on S at step n , and a choice of vectors Y_n , $Y: \{Y_n\}_{n=1}^N$ is called a *policy*, and (4) C is a $p \times 1$ vector which denotes the initial state of the system.

If the system were allowed to run without control, then Equation (1a) would reduce to

$$X_{n+1} = AX_n \quad X_1 = C \quad n = 1, 2, \dots, N \quad (2)$$

The criterion function originates from the desire to control (2) so that $X_n = 0$ (the zero vector); the cost of deviation from this state is $X_n' X_n$, $n = 1, 2, \dots, N$. Likewise, the cost of control is $\delta Y_n' Y_n$, $\delta > 0$. Then, for a particular policy Y , the cost of operating this N-stage system S becomes Equation (1b).

The theory of dynamic programming is used to give us the loss function under optimal policy, where optimal policy is defined as that policy which makes $L_N(C, Y)$ a minimum,

$$L_N^*(C) = \min_Y L_N(C, Y) \quad (3)$$

Theorem 1:

$$L_N^*(C) = C' R_N C$$

where

$$R_1 = I \text{ (the identity matrix)}$$

$$R_{N+1} = I + A' [R_N^{-1} + (1/\delta) I]^{-1} A \quad N = 1, 2, \dots$$

Corollary 1: R_N is a symmetric, non-singular and positive definite matrix for $N = 1, 2, \dots$

Let X_i^* denote the state vector of S on step i under optimal policy, then $Y_{i,N}^*(C)$ the i th vector in the optimal policy for S is

Theorem 2:

$$Y_{i,N}^*(C) = Y_{1,N-i+1}^* \quad i = 1, 2, \dots, N$$

Corollary 2:

$$Y_{1,N}(C) = -[\delta I + R_{N-1}]^{-1} R_{N-1} A C$$

$$Y_{N,N}^*(C) = 0$$

Substitution of the optimal policy into Equation (1a) results in

Theorem 3:

$$X_i^* = \delta^{i-1} T_{N-i+1} T_{N-i+2} \cdots T_{N-1} C$$

$$X_1^* = C \quad i = 2, 3, \dots, N$$

where

$$T_j = [T + R_j^{-1}] A$$

For asymptotic results, we first look at the convergence of $L_N^*(C)$.

Theorem 4:

$$L_N^*(C) \rightarrow L(C, A) \text{ for all } C \text{ and } A \text{ as } N \rightarrow \infty$$

Theorem 5:

$$L_N^*(C) \text{ converges exponentially}$$

To further characterize the convergence, notice that under optimal policy, the loss function, state vector, optimal policy itself, all depend directly on R_N . This is rather unfortunate since R_N is highly nonlinear, and its asymptotic properties are rather difficult to study in this form. If we write $R_N = U_N V_N^{-1}$, and solve for U_N and V_N in such a way that R_N is decomposed into two simultaneous linear difference equations with constant coefficients, then studying this new set of equations we obtain the asymptotic characterization of R_N . That this decomposition can be carried out may be demonstrated, both theoretically and by example.

These results also furnish the basis for a study of similar systems perturbed by noise. It has been shown that if the noise distribution is independent of the system state at time n , the noisy system is equivalent in control policy to a deterministic system as above with the expected values of the state replacing the state. The actual losses incurred will of course differ from expected loss under optimal policy; the distribution of deviation of actual loss from expected loss is being determined.

A recurring problem in numerical computations is the fitting of data to some prescribed functional form over a stated interval in the independent variable. If the data represent observations of a function of known form perturbed by random errors of observation or other noise, it is

customary to use the least squares criterion for fitting. A problem at the other extreme is to replace a known, but complicated, function with a more tractable approximation; an elementary example is the use of a truncated Taylor series for calculating $\exp(x)$. It is necessary to know the maximum error which might occur in using the approximation, so that the criterion of fit is that the maximum error be minimum; fitting under this criterion is called Tchebyscheff approximation, or more simply, T -approximation.

As part of a project of developing a comprehensive systems library for functional approximation, an algorithm for a quite general linear T -approximation method due essentially to Stiefel (Ref 1) has been developed and is being programmed. The essentials of the algorithm are as follows:

Let x be a variable. (Whether x is a linear variable or a vector in p -dimensional space is not material for the algorithm.) Let $f(x)$ be the function to be approximated by a linear combination of $\phi(x) = y_1 \phi_1(x) + y_2 \phi_2(x) + \cdots + y_n \phi_n(x)$ of the n functions $\phi_i(x)$, $i = 1, \dots, n$; and let $S = \{x_1, \dots, x_m\}$ where $m > n$ is a discrete set of x 's over which the approximation is based. Define the deviation $h_i = \phi(x_i) - f(x_i)$ of approximation from actual function at the point x_i for $i = 1, \dots, m$. Then the T -approximation is obtained by choosing the coefficients y_1, \dots, y_n so that $\max(|h_1|, \dots, |h_m|)$ is minimum; the resulting minimum value is called the reference deviation h . If one writes $a_{ij} = \phi_j(x_i)$, $c_i = f(x_i)$, the preceding problem is equivalent to the geometric problem in n dimensions of finding the center of the largest hypersphere which can be inscribed in the simplex defined by the m hyperplanes

$$\sum_{j=1}^n a_{ij} y_j = c_i \quad i = 1, \dots, m$$

The algorithm consists of two parts. First, a reference set of $n+1$ of the points x_i is chosen, and the T -approximation over the reduced problem determined; this is accomplished by a single Gauss reduction of a system of $n+1$ linear equations in $n+1$ unknowns with two back substitutions. Deviations at the remaining points x_i not included in the reference set for the tentative T -approximations are calculated; if none of these deviations are significantly greater than the reference deviation, the problem is solved. Otherwise, the point, say x_k , which resulted in the maximum deviation is abstracted and replaces one of the points in the original reference set. The choice of the replacement is made by application of the exchange theorem of Stiefel, and consists of very short series of tests. The system after exchange is solved as before and the process repeated until all deviations are no longer than the reference deviation of the last reference set.

B. Orbit Computation Methods

1. Recorded Master Tables of Ephemerides

The computational methods for space trajectories used at JPL involve tables of ephemerides for the Moon, planets, and Sun. Since the beginning of the emphasis on space trajectory calculations 2 years ago, confusion has been found in the origin of various ephemerides and the availability of tables for use on the IBM 704 with the trajectory computation programs. A set of master tables consisting of rectangular coordinates in both Earth-centered and helio-centered rectangular coordinate systems for the Moon and all of the planets along with second and fourth central differences is being collected and recorded on magnetic tape. Along with the tables will be a set of programs for printing, punching on cards, or writing on another tape the selected subsections of the master tapes for use in particular problems. The master tapes will cover the period 1960 through 1970, and all are referenced to the beginning of the Besselian year 1950. The information is obtained from the Naval Observatory and is believed to be the best currently available.

2. Satellite Trajectory Computer Programs

An Encke scheme for lunar or Earth satellite trajectories was programmed for the IBM 704 to evaluate the effectiveness of the method and to isolate and formulate the problems which would have to be solved before a useful model could be obtained for production work (RS 6). The following two types of trajectories were investigated, using a Milne method for numerical integration.

a. Lunar trajectory, 66 hours. Starting near perigee and an altitude of 230 km, the lunar trajectory was terminated about 1 Earth radius from the Moon. A definitive Cowell trajectory was also run from the same time points, and the Encke integration step sizes were adjusted so that there was less than 1 km disagreement in position near the Moon. As the Cowell integration took almost 2 minutes of machine time while the Encke integration consumed approximately 70 seconds, the latter method appeared to have justified itself. It was felt that even better results could be obtained by refining the

techniques used in transforming Cartesian coordinates to elements and elements to Cartesian coordinates.

b. Earth satellite trajectory. A high-altitude satellite trajectory (period of 134 minutes, eccentricity of 0.2) was computed and compared to a Cowell integration. Here it was found that frequent rectification was necessary to permit large integration step sizes so that the conic transformation yielded cumulative errors which made a full evaluation of the Encke method versus the Cowell method impossible. Having attributed any differences to the above cause, it was found that the Encke trajectory could be run at least twice as fast as the Cowell trajectory; thus the Encke method was found feasible, but further development of the conic routines would generate greater accuracy. A precise set of routines for calculating osculating orbital elements from rectangular coordinates and back is now under development. A complete Encke routine for space trajectories will be completed in the near future.

3. Interplanetary Trajectory Computer Programs

A general interplanetary trajectory program is presently under development for the IBM 704 and later the IBM 7090. This program will use the Gauss-Jackson second-sum method for solving the n -body orbit problem using a Cowell (RS 6) or the Encke method described earlier. The general program will have provisions for integrating the equations in a coordinate by a triaxial ellipsoid and the Earth by an oblate spheroid. The ability to transform coordinates during computation, such as from an Earth-centered system to a lunar-centered or planet-centered system, will be included in order to calculate lunar satellite or planet satellite trajectories. Provisions will be included for powered flight during any portion of the flight so that a complete lunar or planet landing and return mission can be simulated with midcourse or terminal guidance maneuvers. The program will then be coupled with the complete booster simulation program now available to provide a complete launch mission simulation. Automatic search modes will be available to determine values of selected parameters which will result in a particular type trajectory, such as a lunar hit or a planet near miss.

III. MATERIALS RESEARCH

A. Solid State

1. Anelastic Measurements, Tungsten

The anelastic properties of tungsten at high temperatures are being investigated with a vacuum torsion pendulum in which a 0.015-inch diameter wire specimen is heated directly by passing an electric current through it.

The results reported previously (*RS 1* through *4*) were obtained using a pool of mercury covered with Octoil S to make electrical connection to the free end of the pendulum. This arrangement had two difficulties. The Octoil contributed to carbon contamination of the specimen, and the mercury contributed appreciable background and anomalous damping effects. This mercury contact has now been replaced with a spring contact fabricated from 0.005×0.25 -inch soft copper strip.

The torsion constant of the system is increased by about 30% by the copper spiral. Preliminary measurements with the modified equipment indicate a much lower background damping level, as shown in Figure 3. Curve A is typical of data obtained with the mercury contact, and Curve B was obtained on a similar specimen using the spring contact. The broken portion of Curve A is the region in which anomalous damping effects made results uncertain. Anomalous decay curves are not observed with the spring contact, though a small amount of amplitude dependence remains. This amplitude dependence is a characteristic of the damping behavior of tungsten. Experiments in which the tungsten wire is maintained at room temperature while the copper spiral

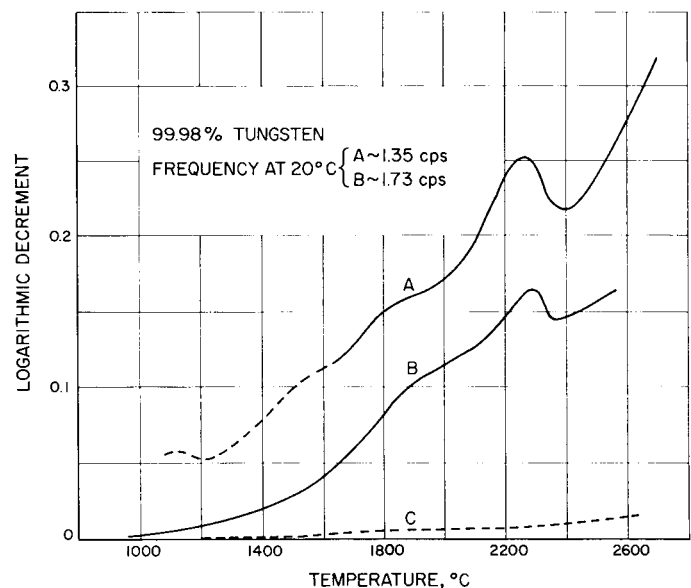


Figure 3. Damping of tungsten measured with apparatus modifications; A, mercury electrical contact; B, copper spring contact; C, damping contributed by copper spring

is heated through its operating range show that the spiral contributes no amplitude dependence. The damping contributed by the spiral is shown in Curve C of Figure 3.

Some test spirals of silver foil are also being fabricated. The higher electrical conductivity and lower elastic modulus of silver should permit a spring contact of much lower stiffness than the copper one. This will result in an even smaller contribution of the contact to the modu-

lus and damping measurements. One difficulty remains to be corrected in the modified equipment. There is no provision for damping out lateral oscillations, and these modes interfere at the higher frequencies (above 1.5 cps). Ways to remedy this are being investigated. The goal of this work is to develop a torsion pendulum suitable for operation in a small ultrahigh-vacuum system.

The peak occurring near 2300°C in the tungsten damping curves appears to be due to some form of contamination which occurs when the wires are heated in vacuum (RS 3 and 4), but the contaminant has not been definitely identified. X-ray diffraction analysis indicates that some W_2C forms on the wire even when a liquid-nitrogen cooled trap and the spring contact are used. This W_2C may be responsible for the peak. Skaupy (Ref 2) and Becker (Refs 3, 4) have reported a polymorphic phase transformation in W_2C in the temperature range 2200 to 2400°C.

2. Anelastic Measurements, Fe-Al Alloys

Anelastic techniques are being employed to obtain information on the rate of interstitial and substitutional atom movement and certain magnetic properties of iron-rich Fe-Al alloys. Anelastic effects are being measured as a function of temperature, frequency, composition and magnetic state using a torsion pendulum apparatus.

An interpretation of the magnetic damping behavior of Fe-Al alloys in the composition range 0 to 22 at. % Al was proposed earlier (RS 6). The minima observed in the magnetoelastic damping at low strain amplitude on the low-temperature side of the Snoek (interstitial) and Zener (substitutional) relaxation peaks were attributed to stabilization of the magnetic domain configuration by directional ordering (Ref 5) of the appropriate atom species. The magnetoelastic relaxation peak observed on the high-temperature side of the Snoek and Zener relaxations was ascribed to a mechanism in which the anelastic strain is magnetoelastic and the rate determining process is rearrangement of the directional order as the domain walls are oscillated about their equilibrium positions by the oscillating stress.

Additional data obtained recently has confirmed this model in general and has further elucidated some features of it. It was stated previously that the magnetic peak height increased approximately as the square of the aluminum percentage. This is incorrect. The peak height might be expected to be proportional to the ΔE effect (the change in elastic modulus on magnetization) instead, but data to check this hypothesis is not available.

Although the activation energies for the magnetic peak and for the decay of damping following demagnetization in the minimum damping region are approximately the

same as the activation energy for the Zener (stress-induced ordering) relaxation, the relaxation times are quite different. Relaxation times for the magnetic peak are higher than those for the Zener relaxation by approximately an order of magnitude, whereas the times for decay of damping are about two orders of magnitude less than the Zener values. In the simplest case, in which the mechanism of directional ordering is the same as that for stress-induced ordering, these relaxation times might, at first thought, be expected to be the same. It is not necessary, however, that these ordering mechanisms be the same. In fact, the detailed mechanism is not known in either case. In addition to possible differences in the detailed atomic arrangement, there is another difference between the magnetic peak and the Zener peak. In the case of the Zener relaxation, the ordering is a volume process in which individual atoms move independently. In the case of the magnetic peak, the change in order occurs at an interface (domain wall) whose motion is determined by the rate at which ordering occurs. This should have the effect of increasing the number of atom jumps required and therefore increase the relaxation time. The very fast relaxation of damping following demagnetization is more difficult to explain. All measurements have been made at strain amplitudes appreciably smaller than those required to tear the domain wall free (under equilibrium order conditions). Thus appreciably less than the equilibrium degree of order should be required to pin the domain walls. This would cause a low apparent relaxation time. In addition, the decay of damping is quite sensitive to small magnetic, mechanical, and thermal disturbances and the sample is continually perturbed by the measurements, making accurate determinations difficult.

B. Ceramics

1. Magnesium Oxide Thermal Conductivity Specimens

Dense high-purity magnesium oxide specimens were required for use in the thermal conductivity measurement furnace described in RS 6. The specimens consist of a thick-walled tube with a 1.75-inch outside diameter and 0.75-inch inside diameter. For the temperature measurements, five axial holes are radially placed in 0.0625-inch steps in the specimen tube wall. The holes are spiraled uniformly in the circumference so that the

temperature drop through the wall can be measured (RS 6, Fig 9).

Fused magnesium oxide of 98 to 99% purity with grain sizes from 40 to 325 mesh was obtained from the General Electric Company. Precipitated magnesium oxide 99% pure was obtained from Fisher Chemical Company. The precipitated material was in the form of agglomerates with an ultimate particle size of 0.1 micron. A 1.2 gm/cc gaging solution of $MgCl_2$ was made using Baker reagent grade $MgCl_2 \cdot 6H_2O$ crystals.

To facilitate fabrication, a body with enough green strength to withstand machining and drilling was desired. Magnesium oxychloride cement bond was tested for the effect of (1) the material limits, i.e., fused vs precipitated, (2) the grain size, and (3) the percentage of gaging solution. It was found that with the fused material good forming, good strength, and good machining properties could be developed with as little as 2.5% magnesium chloride gaging solution. When more than 20% of the fine precipitated magnesium oxide was mixed with the fused material, dry pressing became more difficult.

The precipitated MgO forms a strong oxychloride bond, but it is difficult to fabricate. Because of the fine particle size, the very large surface area absorbs the gaging solution, making distribution difficult. When 100% precipitated material was used, the forming properties were unsatisfactory even when 35% of the gaging solution was added.

The machinability and strength was satisfactory for all of the fused material mixes and for the precipitated material. The coarse-grained material chipped when machined, but was still satisfactory.

The specimens were sintered at 2800°F in air. The shrinkage at this temperature for the fused material was less than 1%, and no increase in density was observed. The oxychloride bond volatilizes at about 300 to 400°F but does not damage the specimen. The specimens have high enough unbonded strength to hold together until they are sintered. Pressed densities ranged from 2.6 to 2.8 gm/cc (70 to 80% theoretical density) with pressing pressures of 10,000 to 20,000 psi.

Future studies of the thermal conductivity will require controlled grain size and density of the pure MgO . The magnesium oxychloride bond will be useful as a fabrication technique for the development of specimens formed by dry-pressing, hydrostatic-pressing, and slip-casting.

2. Zirconium Oxychloride Bond

Since the magnesium oxychloride bond method proved so useful, the possibility of a zirconium oxychloride bond was investigated. Probe tests were conducted using 325-mesh lime-stabilized zirconium oxide. Powdered zirco-

nium tetrachloride (Fairmount Chemical Co.) and zirconyl chloride (Fisher Scientific Co.) were used as the chloride sources. The dry chloride powders were added in the amount of 10 wt % to the zirconium oxide in two ways: (1) by mixing the chloride first with an equal weight of water, and (2) by mixing the chloride powder with the ZrO_2 and then adding the water just before pressing.

From the tests it was found that (1) the zirconium tetrachloride formed a stronger bond than the zirconyl chloride, and (2) the mixing of the dry powders was superior to the solution mixing. The bond was not as strong as the magnesium oxychloride bond, but it was much stronger than the unbonded zirconium oxide. The bond gave good machinable strength when the specimens were air-dried, and also when they were heat-treated between 400 to 1200°F in air. One disadvantage to this bond method is the evolution of HCl and Cl_2 fumes when water is added to the mixture.

3. Zirconium Oxide Stabilizers

Due to the fluxing of aluminum oxide with the lime stabilizer in commercial zirconium oxide at 1400°C, a search was made for a more suitable stabilizer. For the preliminary study, the known stabilizers of zirconium oxide were listed with their aluminum oxide solidus or liquidus temperature, depending upon the information available. The liquidus will always be somewhat higher than the solidus. This data is listed in Table 1.

Table 1. Zirconium oxide stabilizers

Ion	Cubic structure formation	Lowest melting point* with Al_2O_3 ion, °C	Remarks
ZrO_2	No	1900 l	Unstabilized
CaO	Yes	1400 s	Standard commercial stabilizer
MgO	Yes	1925 s	Highest refractoriness
BaO	No data	1660 s	
TiO_2	No	1715 s	Large amount of TiO_2 required to suppress the transition temperature
UO_2	No	1900 s	Large amount of UO_2 to suppress the transition temperature
ThO_2	No	1900 l	Does not stabilize ZrO_2
Ce_2O_3	No	1800 l	Suppress the transition temperature
La_2O_3	Yes	1900 l	
Nd_2O_3	Yes	No data	
Y_2O_3	Yes	No data	

*The symbol l = liquidus, and s = solidus or temperature where first liquid forms.

From this study, the stabilizers Y_2O_3 , CeO_2 , and MgO were chosen for further study. Specimens using these stabilizers were fabricated along with CaO stabilized, unstabilized, and Metro ZrO spray powder for comparison. Magnesium oxide as a stabilizer appears to be the most promising. Some of the stabilizers were not considered in this preliminary study because they were unavailable or hazardous to use. Melting temperature with Al_2O_3 and Al with the ZrO_2 specimens will be measured in future studies using the arc-image furnace.

C. Graphite

1. Graphite Tension Testing

The effects of processing variables on the high-temperature mechanical properties of graphite is one of the areas in which reliable information is lacking. To provide such information, a series of special made-to-order grades of graphite has been obtained from one of the carbon producers. In processing these grades, special care was taken to measure and hold constant just as many of the processing variables as possible with the commercial equipment used. All of the blocks were made from one lot of starting ingredients, i.e., petroleum coke and coal tar pitch. The processing variables which were changed one at a time were: coke particle size and particle size distribution, coke-to-pitch ratio, molding pressure, reimpregnation, and graphitizing temperature. Approximately sixty different graphites were made using different combinations of these processing variables. These are now available for various mechanical and thermal property testing.

Since previous results (RS 1) have shown that some high-temperature tensile properties are affected by the testing strain rate, it was decided to determine these effects before proceeding with a comprehensive testing program on these special grades. Three blocks which were thought to be representative were selected, and tensile tests were run at strain rates in the range of 5×10^{-5} to 10^{-2} sec^{-1} using the testing techniques previously described (Ref 6). Table 2 lists the processing variables for the three blocks selected for these tests. Figure 4 shows the ultimate strength, elongation, and reduction of area at 5000°F determined at the various strain rates for these blocks. In these figures, the vertical lines show the

Table 2. Processing variables for special graphites

Block No.	Petroleum coke particle size	Coke-to-pitch ratio	Molding pressure, T/in. ²	Reimpregnation	Graphitizing temperature, °C
5703	60% < 74 micron (200 mesh)	100/41	1	None	3000
8303	60% < 74 micron (200 mesh)	100/41	4	None	3000
11603	99% < 125 micron (115 mesh); 96% > 61 micron (250 mesh)	100/36	4	None	3000

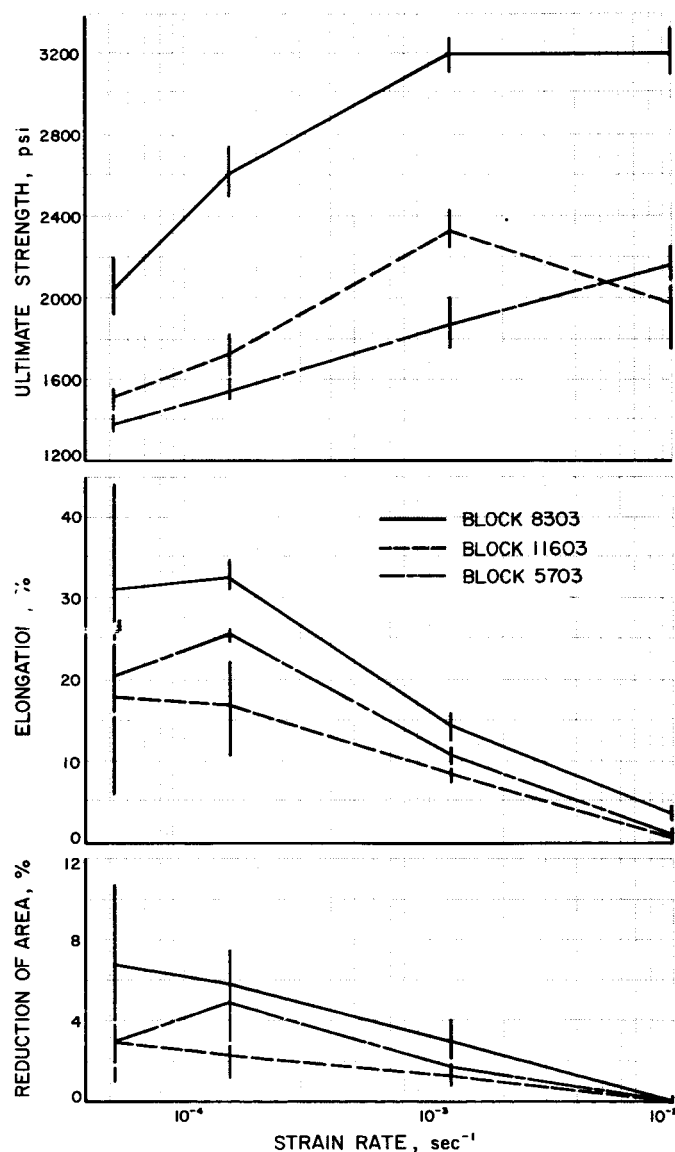


Figure 4. Ultimate strength, elongation, and reduction of area vs strain rate at 5000°F , stress parallel to grain

range of individual data points, and the curves are drawn through the average values.

These results show some of the same effects reported previously (*RS 1*), i.e., that the ductility as measured by the elongation and reduction of area decrease markedly with increasing strain rate, and reach very low values (less than 2%) at a strain rate of 10^{-2} sec $^{-1}$.

While the ultimate strength results are not as consistent for these three blocks, in general the strength is higher at the higher strain rates. This differs from previous results (*RS 1*) where the strength showed no consistent change with strain rate.

These tests are just the initial portion of the first phase of a complete testing program, the results of which will be used to determine testing procedures for further tests to be conducted utilizing these made-to-order grades of graphite.

D. Nozzle and Endothermal Materials

The present data on graphite nozzle materials are a continuation of previously reported work on the applicability of this material in solid rocket motors having burning durations up to 60 seconds at chamber pressures below 500 psia. In this series of tests, graphite nozzles supplied by National Carbon Company are being employed. They are composed of graphite CS 312, with the nozzle axis parallel to the grain, and NT 0005, with the axis perpendicular. Coatings of silicon nitride of single and double thickness were also supplied on these designated grades of graphite.

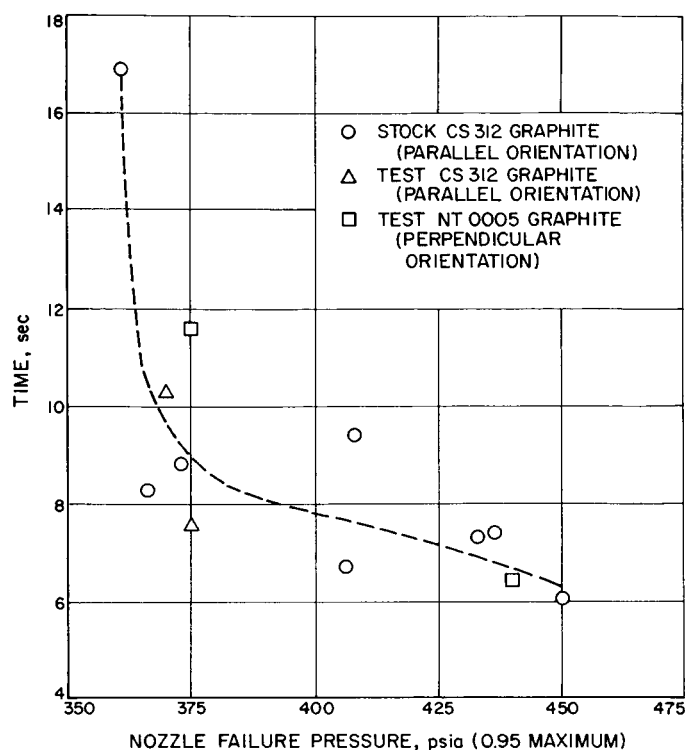


Figure 5. Chamber pressure at nozzle failure vs time for graphite nozzles

The purpose of the preliminary testing with uncoated nozzles is, first, to establish the degree of similarity of both grades of material with nozzle tests previously performed with graphite CS 312 having the parallel grain orientation, and secondly, to determine the relative merit of the coatings. The results obtained to date are given in Table 3. Two tests of CS 312 nozzles were sufficient to indicate the desired properties. The first test of an NT 0005 nozzle, however, was anomalous in that the erosion effects at the throat were not compatible with

Table 3. Graphite nozzle test data

Test ^a No.	Nozzle material designation ^b	Final throat dia, ^c in.	Maximum chamber pressure P_{max} , psia	Time for pressure to reach $0.95 \times P_{max}$, sec	Remarks
34	CS 312	0.348 to 0.357	390	10.3	Irregular throat erosion
35	NT 0005	0.348 to 0.364	383	No dropoff from P_{max}	Irregular throat erosion
36	CS 312	0.348 to 0.368	395	7.5	Irregular throat erosion
37	NT 0005	0.375 to 0.420	463	6.4	Irregular throat erosion
38	NT 0005	0.320 to 0.341	395	11.6	Irregular throat erosion
39	CS 312 With single coating of silicon nitride	0.311 to 0.313	405	No dropoff from P_{max}	No observable erosion

^aFiring duration of tests: 16 to 18 seconds.
^bFor grade CS 312 nozzle axis was parallel to grain; for NT 0005, nozzle axis perpendicular to grain.
^cInitial throat diameters were 0.318 to 0.319 inch except for coated nozzle in Test 39 which was 0.311 to 0.313 inch.

the flat pressure-time curve. Two further tests were therefore required. Nozzle tests 34 to 38 appear to have pressure-time characteristics, as indicated by the pressure drop criterion, fairly similar to that produced before by parallel grain CS 312 graphite. The data comparison is shown graphically in Figure 5, revealing no pronounced differences in the uncoated materials.

The single coating of silicon nitride tested at approximately 400 psia (Test 39) proved to be resistant throughout the burning duration (18 sec). It was subsequently retested in the 425-psia pressure range, but restrictor failure prevented evaluation of the results.

The final evaluation of silicon nitride as a coating material will be determined when several more tests are completed.

E. Pressure Vessel Materials

1. Brittle Fracture of Metallic Sheet Materials

A recently developed heat-treating process^a is claimed by the developer to increase the ultimate tensile strength of presently used steel and titanium alloys by 50,000 to 100,000 psi without a corresponding decrease in ductility. If such claims can be substantiated by more extensive

testing, this would have a marked effect on the use of such alloys in the design of space vehicles because of the higher strength-to-weight ratios which would result.

To obtain some additional information, preliminary tension tests were run on heat-treated specimens of 4130 and 4340 low-alloy steel supplied by the developer. As supplied, the specimens were approximately 0.125-inch thick with a 0.5-inch wide by 21 inch long gage section. Since elongation was one of the important properties to be measured, a series of grid lines spaced at 0.1-inch intervals was applied to the gage section. A specimen with these grid lines is shown in Figure 6. Using this technique, it was possible to determine the final elongation over 0.1-inch gage lengths for the entire gage section. A load-deformation curve was recorded to a deformation of approximately 0.04 inch, using a 2-inch extensometer at a magnification of 250 \times . The load was applied with a 300,000-pound testing machine at a crosshead movement of approximately 0.01 in./min. The tensile results obtained are given in Table 4.

Typical engineering stress-strain curves for these alloys are shown in Figure 7. It is interesting to note that all of these curves have a flat portion in the region of the 0.2% offset yield point, so that the ultimate strength and the 0.2% yield strength have the same value. It should also be noted that shortly after the 0.2% offset is reached, instability occurs and the load drops suddenly to a lower value after which the load decreases gradually to fracture. This is not normal behavior for these alloys when heat treated by conventional techniques.

The elongation of these specimens in either 2 inches or in 4.5A^{0.5} inches as shown in Table 4 is lower than that found after conventional heat treatment of these alloys. The elongations determined for the 0.1-inch intervals in the region near the fracture are shown in Figure 8. It

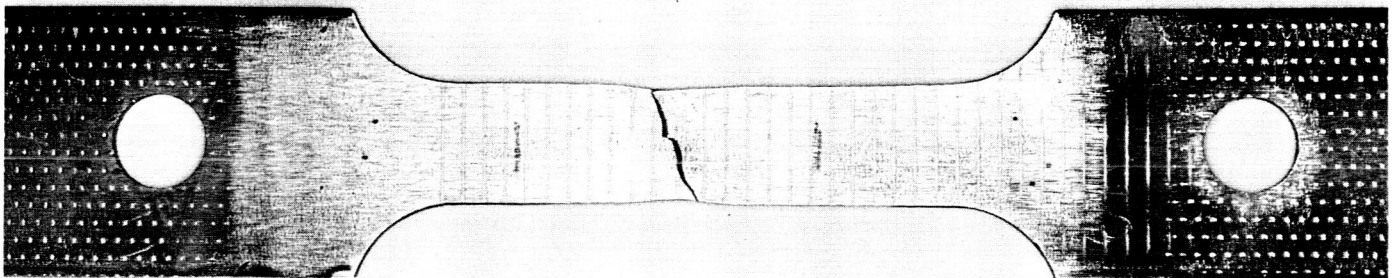


Figure 6. Tensile test specimen

^a The Basset Process was developed by the Research Development Corporation of America.

Table 4. Tensile properties of low-alloy steel

Alloy	Spec. No.	Gage section, in.	0.2 % offset yield strength, psi	Ultimate tensile strength, psi	Elongation in 2 in., %	Elongation in 4.5A ^{0.5} , %	Reduction ^a of thickness, %	Reduction ^a of area, %	Hardness, Rc	
									Before	After ^b
4130	D-1	0.118 × 0.496	285,000	285,000	4.00	6.34	22.20	26.4	45.0	—
	D-2	0.115 × 0.492	288,500	288,500	4.25	7.27	16.10	22.1	45.7	—
	D-3	0.116 × 0.502	279,000	279,000	4.00	6.80	21.80	26.1	45.5	—
	D-4	0.113 × 0.498	285,000	285,000	4.65	7.74	17.70	22.4	45.6	—
	D-5	0.115 × 0.494	282,000	282,000	4.10	6.80	26.10	29.4	44.6	—
	D-6	0.112 × 0.495	296,000	296,000	4.40	7.73	22.30	26.7	48.0	—
		Average	285,900	285,900	4.23	7.11	21.03	25.5	45.7	—
4340	AE-7	0.125 × 0.548	327,000	327,000	4.00	5.57	11.20	17.5	52.2	51.7
	AE-8	0.129 × 0.548	334,500	334,500	4.00	5.57	15.40	21.8	53.9	51.9
	AE-9	0.128 × 0.548	330,000	330,000	3.60	4.78	9.30	15.7	56.1	51.9
	AE-10	0.126 × 0.549	328,000	328,000	3.45	5.33	9.87	15.1	54.6	51.8
	AE-11	0.127 × 0.547	324,000	324,000	4.05	5.57	11.80	17.3	55.2	51.9
	AE-12	0.126 × 0.549	316,500	316,500	5.65	7.53	13.60	21.2	52.5	51.6
		Average	326,700	326,700	4.13	5.73	11.86	18.1	54.1	51.8

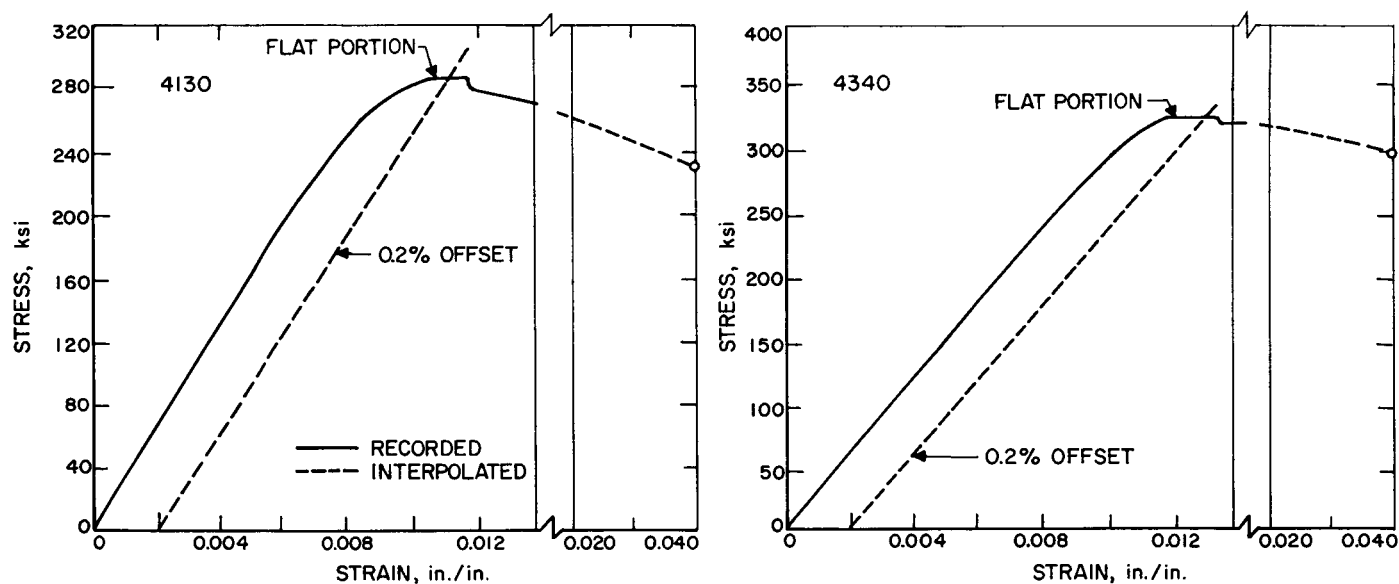
^aMaximum value.^bTaken in strained portion.

Figure 7. Typical engineering stress-strain curves

can be seen that for the 4130 alloy most of the plastic deformation occurred in a region about 0.3 inch long. For the 4340 alloy this region was about 0.5 inch long. The maximum elongation measured was greater for the 4130 alloy than for the 4340 alloy. This concentration of plastic deformation to a narrow region of the gage section is not normal behavior for these alloys, and is initiated at the point of instability on the stress-strain curve.

From the results of these tests, it would appear that this heat treating process not only increases the ultimate tensile strength of these alloys, but also affects the plastic behavior in ways that are not fully understood. On the basis of these results additional testing will be done which will allow better comparison with conventional heat treatments and which will also provide some information on the resistance of such alloys to brittle fracture.

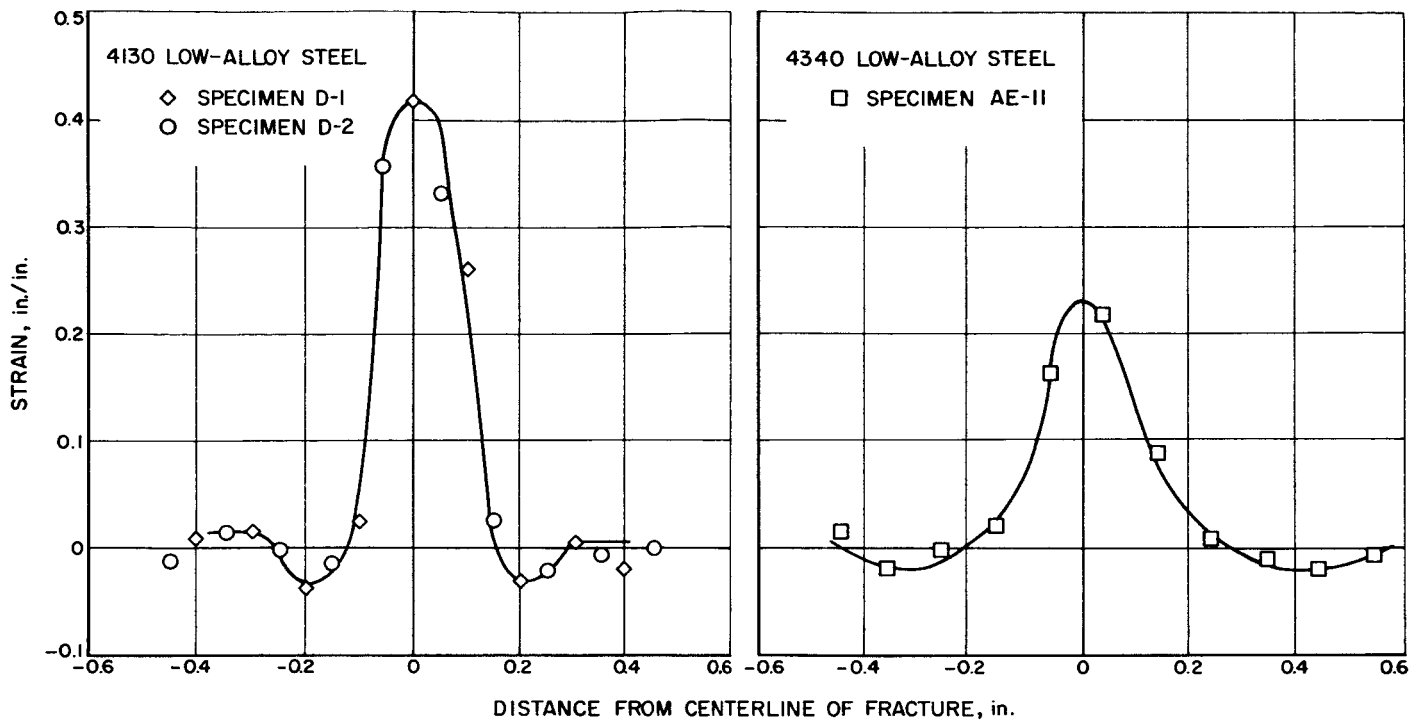


Figure 8. Longitudinal strain distribution in region of fracture

IV. SPACE ENVIRONMENT SIMULATION

In *Research Summary No. 6*, the plans for modifying the 6×7 -foot vacuum chamber to a deep-space environment simulator were discussed. These modifications are scheduled to be completed in June 1960. Preliminary *Ranger* spacecraft testing is to begin at that time. A major concern in the *Ranger* program is the adequacy of the passive temperature control system. Tests scheduled for November on the *Ranger* proof-test model are to be run in the space environment simulator. These will provide verification of the *Ranger S-1* system design.

Figure 9 is a sketch of the proposed deep-space simulator with its shroud, consisting of a cylindrical section of plate coils and a spherical dished top and bottom. Four National Ventarc lamps (carbon arc lamp) will be positioned on top of the chamber and will shine through quartz windows onto the payload to simulate sunlight. These lights will be used alternately during a run. Three will continually illuminate the payload; whenever one is shut down to change carbon rods, the fourth will be

turned on to take its place. The power of these lamps is such that three of them will give enough energy over a 42-inch diameter circle to duplicate the solar constant at the radius of the Earth's orbit from the Sun.

Figure 10 shows a National Ventarc lamp during a window evaluation test. This test was run to determine whether Vicor windows (quartz was not available for this run) will withstand the heat from an arc light. It was also run to determine whether *Sergeant* flat black paint (MIL-E-10687A), a possible method of blackening the inner surface of the shroud, could withstand the combined environments of arc-light radiation, changes in temperature, and vacuum.

The adequacy of the liquid-nitrogen cooled shroud as a simulation of the heat sink capacity of outer space has been considered. Figure 11 shows that with a sink at 75°K (approx LN_2 temperature), rather than 3°K of outer space, the error in heat transfer simulation for the conditions assumed in this calculation is less than 0.5%.

V. SOLID PROPELLANT PROPULSION

A. Basic Investigations of Resin Binders

1. Stress as a Reduced Variable: Stress Relaxation of SBR Rubber at Large Strains

The reduced variable concept for linear viscoelastic behavior covering the effects of time, temperature, and concentration (for solutions) proposed by Ferry (Ref 7) 10 years ago has proved eminently successful as a method of showing the interactions between these parameters. This concept has been used frequently in the past to study and correlate the mechanical properties of polymers and composite solid propellants over wide ranges of time and temperature (Ref 8, CBS 52, 53, 54, 64, and 66). In principle, this treatment is limited to deformations sufficiently small for the stress-strain relationship to be considered linear. However, it has been found that ultimate properties have the same time and temperature dependence as small deformation properties.

This restriction is now examined, and a method of circumventing it is proposed. The most general expression of the tensile stress-strain law simply states that the stress based on the initial cross-sectional area S is proportional to the strain e through some function f of time t , absolute temperature T , and extension ratio $\alpha = e + 1$.

$$S = e f(t, T, \alpha) \quad (1)$$

For small deformations, the effects of time and temperature are factorable, though interrelated through the Ferry shift factor a_T . Thus Equation (1) can be rewritten as

$$S = e f(\alpha) g(T) h(t/a_T) \quad (2)$$

where for small deformations, $f(\alpha)$ is unity and it is known that $g(T)$ is just T and $h(t/a_T)$ equals $T^{-1} E(t/a_T)$, the time and temperature dependent Young's modulus E . But if the effects of large strains are also factorable, then at any given temperature there results a modified Hooke's law

$$S = E(t) e f(\alpha) \quad (3)$$

Therefore, this equation can be linearized by defining a strain-reduced stress S^* as $S/f(\alpha)$, and the resulting expression can be used in the standard equations for viscoelastic behavior derived for spring-dashpot arrays. This factorization is tacitly assumed but not explicitly demonstrated by Mason (Ref 9). Previously (Ref 10 and RS 1), a study was made of the applicability of seven stress-strain equations to tensile curves of polyurethane and styrene-butadiene rubbers obtained under varying experimental conditions of strain rate and temperature. It was concluded that only the empirical expression discovered by Martin, Roth, and Stiehler (MRS equation, Ref 11)

$$S = E(t) e \left[\frac{1}{\alpha^2} \exp A \left(\alpha - \frac{1}{\alpha} \right) \right] \quad (4)$$

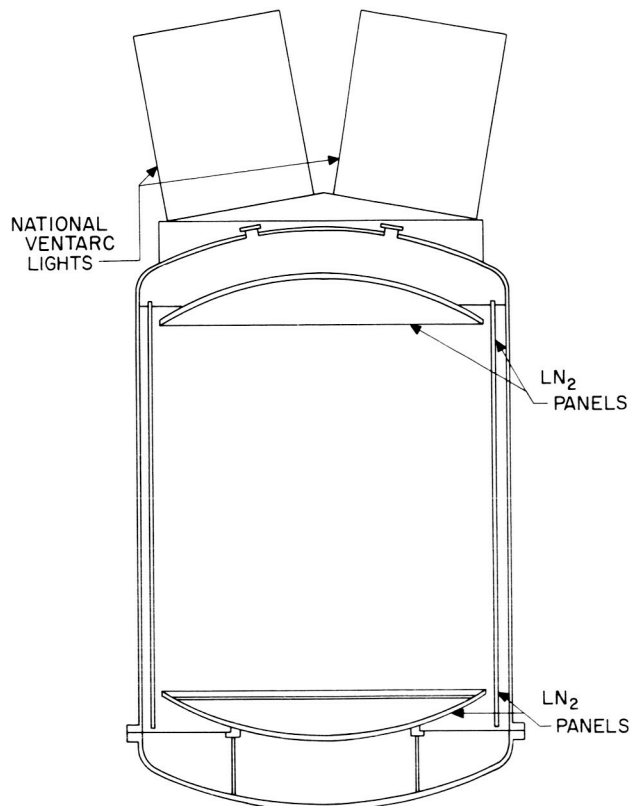


Figure 9. Vacuum chamber space environment simulator, 6 × 7 feet

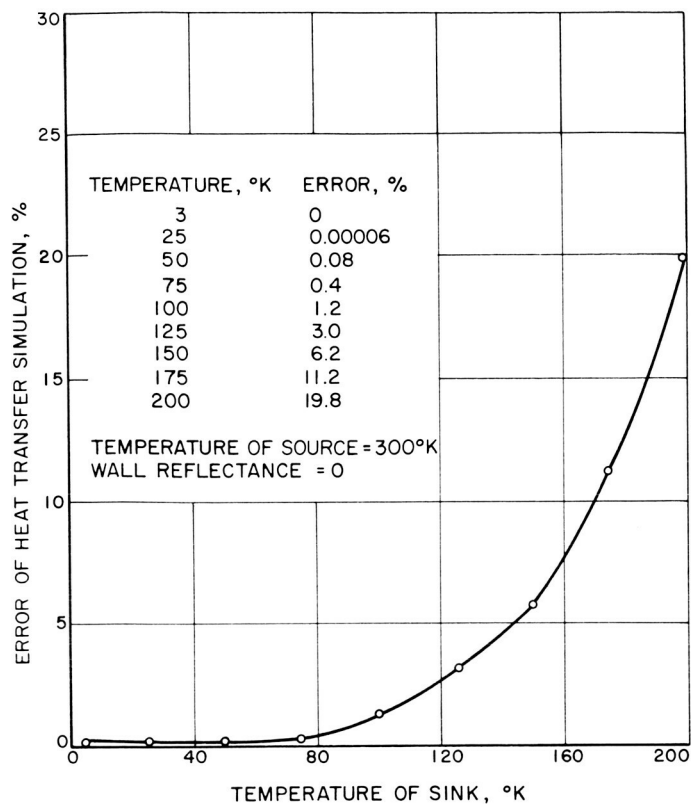


Figure 11. Error of radiant heat transfer simulation vs temperature

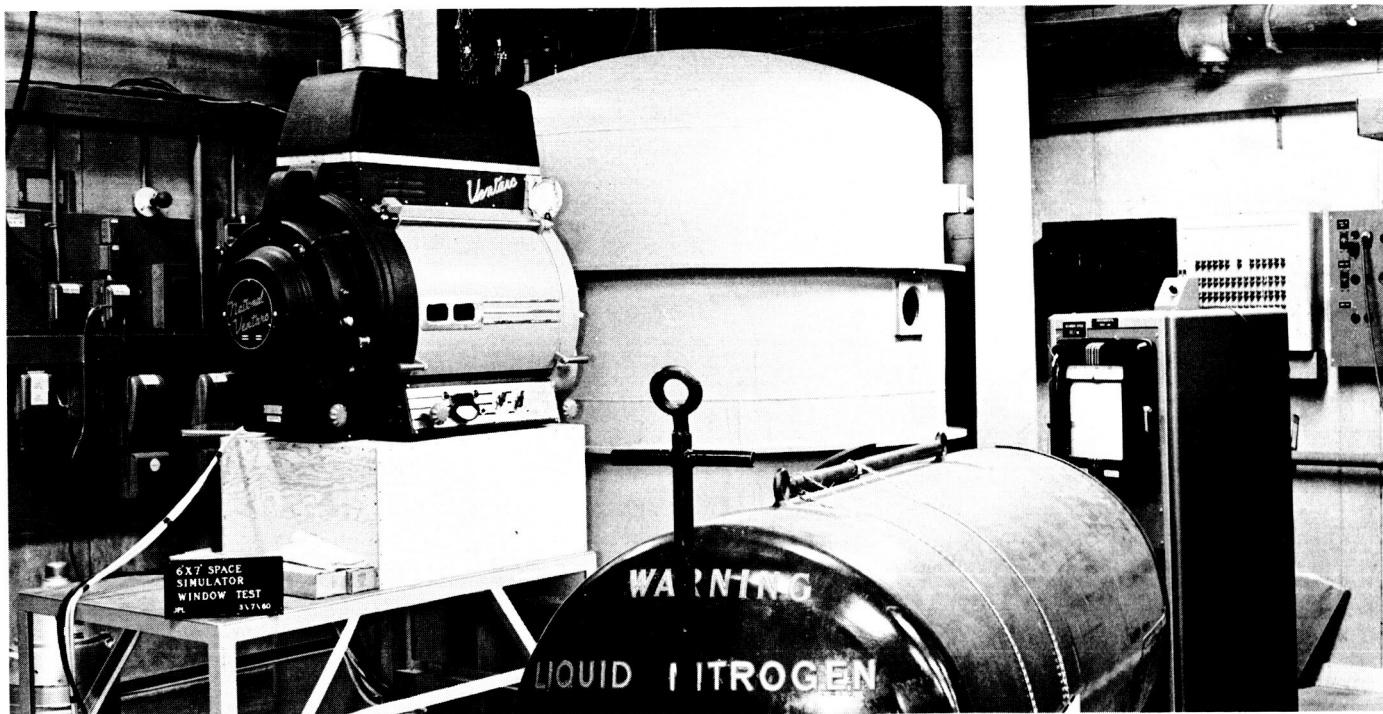


Figure 10. Window test of 6 × 7-foot space environment simulator

adequately represented experimental results over large ranges of deformations. Therefore $f(\alpha)$ is given by the bracketed expression of Equation 4. However, in these constant strain rate studies the value of A was found to lie somewhere between 0.4 and 0.5, whereas the MRS value obtained in isochronal studies was about 0.38. The present work confirmed the validity of this equation and also provided data for an experimental test of the reduced variable concept.

a. Experimental. The stress-relaxation data employed in this study were obtained simultaneously with data on ultimate properties, which were partially presented earlier (RS 4). The styrene-butadiene rubber (SBR; formerly designated GR-S) and the specially constructed apparatus were also previously described (RS 4). Stress-relaxation experiments were carried out at eight temperatures between -5 and $+60^\circ\text{C}$ and at several strains between 50 and 525%, as indicated in Table 5. The overall accuracy of the results was limited by several factors: (1) the sample-to-sample variability; (2) the variation in strain rate employed during the initial elongation; (3) the sensitivity and drift of the load-measuring system, including the recorder; and (4) temperature fluctuation. For any given stress-relaxation experiment, the precision is estimated to be $\pm 5\%$ while the overall accuracy at any given temperature is estimated to be ± 10 to 20% . In addition, a limited number of constant strain rate tensile tests were made in order to apply the MRS equation to tensile data for this same rubber. The constant A was calculated by this method for comparison with that obtained from isochronal data. A reduced stress-strain curve was also constructed in the manner of Smith (Ref 12). The latter is important because $E(t)$ can be calculated from such a curve and should serve as a basis of comparison with $E(t)$ obtained directly from the stress-relaxation data.

b. Determination of the MRS constant A . Typical stress-relaxation curves measured at 1.7°C are shown in Figure 12. The constant A was evaluated from these data

Table 5. Initial strains applied at the various temperatures

$t, ^\circ\text{C}$	Strain range, %
-5	275 to 550
1.7	325 to 525
7.2	325 to 525
12.8	200 to 500
18.3	150 to 450
40	100 to 350
50	50 to 300
60	50 to 300

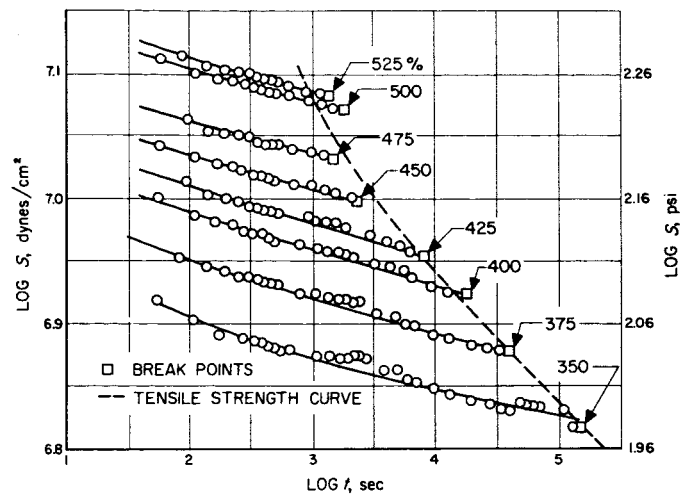


Figure 12. Typical stress-relaxation curves at 1.7°C ; the numbers indicate the strain initially applied; the dashed line indicates the breaking stress

by interpolating the stress values at times of 1, 5, 10, and 100 minutes and cross-plotting as required by the MRS equation. The results are shown in Figure 13, and the values of A thus obtained are given in the figure. The value of A cannot be determined with precision.

The results for the determination of A at all test temperatures and six relaxation times are given in Table 6. It can be seen that there is a slight dependence of A on both the temperature and on the time at which readings are taken. Figure 14 compares the temperature dependence of the average value of A given in Table 6 with that obtained in the constant strain rate experiments. Although the data, when taken together, apparently indicate a uniform increase of A with temperature,

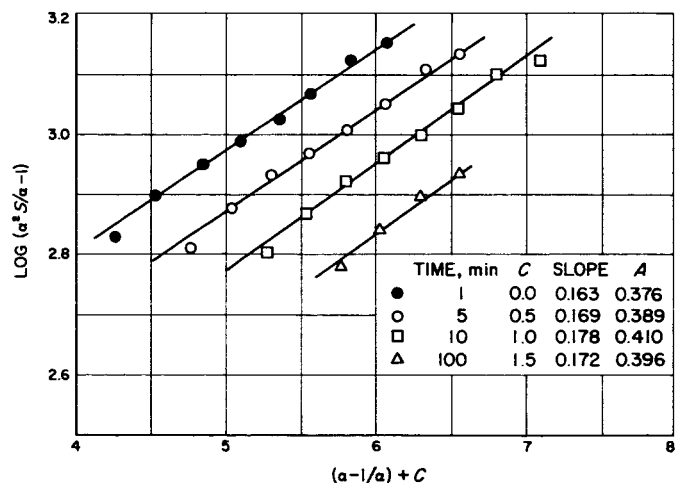


Figure 13. Determination of MRS Constant A at 1.7°C

Table 6. Values of Constant A in MRS equation

Temp, °C	S ₁	S ₅	S ₁₀	S ₁₀₀	S ₁₀₀₀	S _{10,000}	Average
-5.0	0.40	0.42	0.42	0.42	0.43	0.45	0.42
1.7	0.38	0.39	0.41	0.40	—	—	0.39
7.2	0.40	0.41	0.40	0.41	0.39	0.39	0.40
12.8	0.35	0.35	0.36	0.36	0.37	0.37	0.36
18.3	0.39	0.40	0.40	0.41	0.43	0.44	0.41
40.0	—	0.43	0.43	0.44	—	—	0.43
50.0	—	0.40	0.40	0.39	0.44	—	0.41
60.0	—	0.42	0.43	0.42	0.46	—	0.42
Average	0.38	0.41	0.41	0.41	0.42	0.41	0.40 0.41

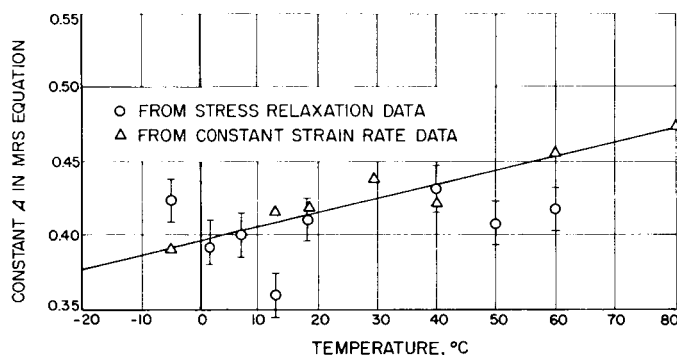


Figure 14. Temperature dependence of the average values of the MRS Constant A

the constant strain rate data are suspect at lower temperatures because the necessary assumption of equilibrium behavior and of constant $E(t)$ is not correct under

these conditions. If $\log E(t)$ is decreasing while the stress-strain curve is being measured, then the effect will be to decrease the apparent value of A with decreasing temperature, as observed. The values obtained in the stress-relaxation experiments do not suffer from such a defect, but the experimental scatter is so great that it is difficult to decide whether or not A is truly temperature dependent.

The average values of A at each temperature also show a slight increase with log time. If true, this would represent a serious drawback to the utility of the MRS equation. However, in view of the experimental error in A, it seems reasonable to use an average value of 0.40 for subsequent calculations.

c. Reduced variable treatment in terms of strain-reduced stress. Assuming that the required function of α is given by the MRS equation and taking the value of A to be 0.40, the expression for the strain-reduced stress-relaxation modulus is given by

$$E(t) = \frac{S^*}{e} = \frac{\alpha^2 S}{e} \exp - 0.40 \left(\alpha - \frac{1}{\alpha} \right) \quad (5)$$

Figure 15 shows the results calculated from the data of Figure 12. The line represents an average curve through the results at all eight strains. The points deviate from this line by only $\pm 6\%$. Thus the family of stress-relaxation curves obtained at different constant elongations is compressed into a single modulus curve. Figure 16 shows this average curve and the corresponding curves for other temperatures. The sharp drop in $\log E(t)$ between 10^5 and 10^6 seconds at 50 and 60°C is attributed to oxidative degradation of the rubber.

These averaged curves can be superposed into a single composite curve by first converting the measured modu-

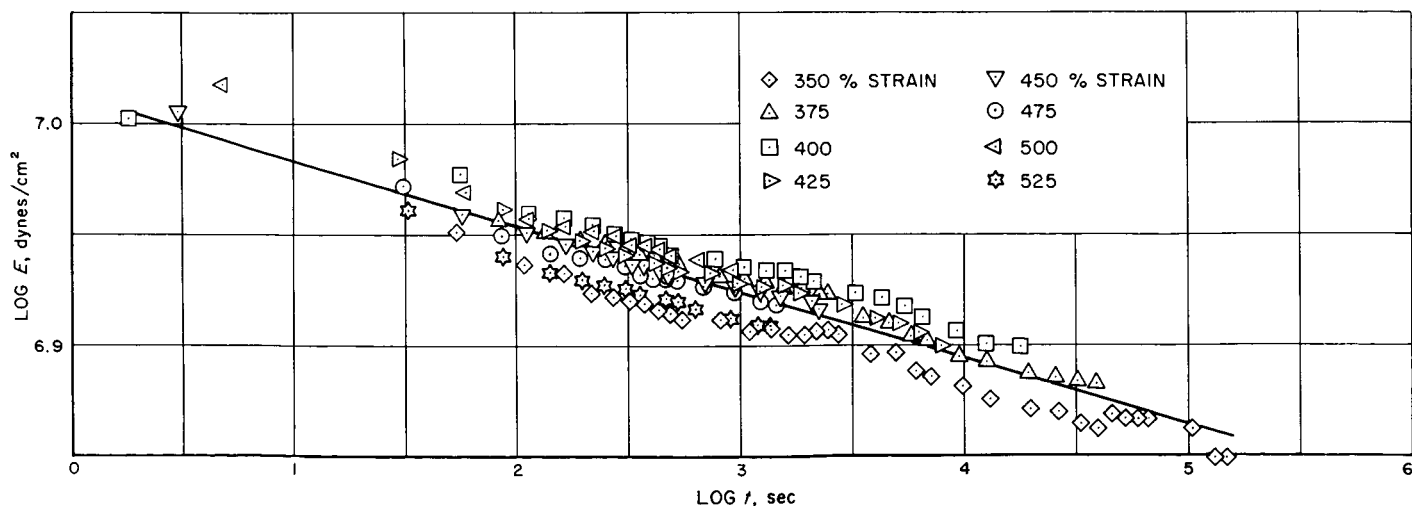


Figure 15. Strain-reduced stress-relaxation modulus at 1.7°C

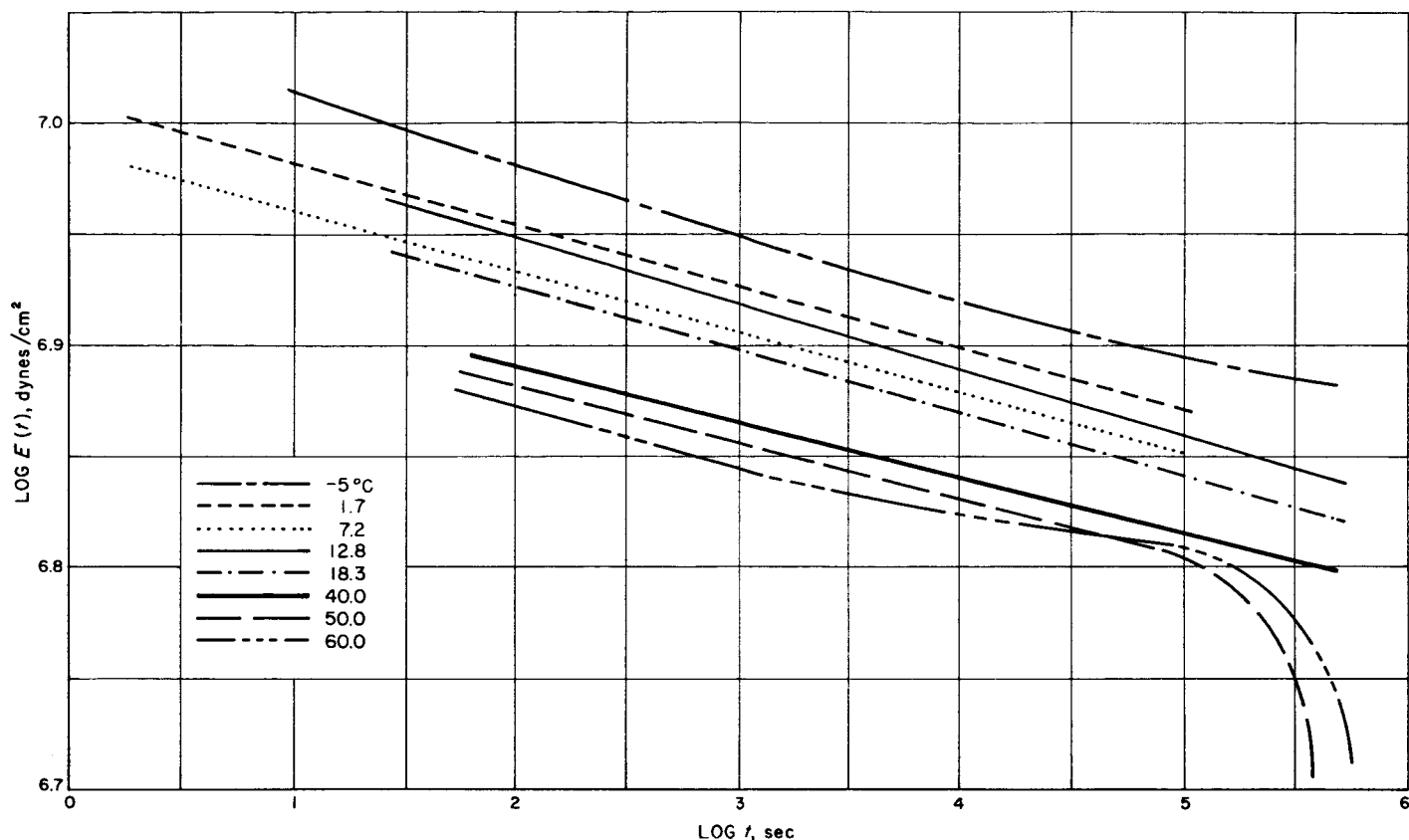


Figure 16. Strain-reduced stress-relaxation modulus at various temperatures

lus to the reduced modulus $E_r(t) = E(t) 286^\circ\text{K}/T$ and then subjecting the reduced modulus plots to suitable horizontal translation along the time scale. The extent of the translation is defined as $1/a_T$. Values of a_T so obtained, as well as values from the time-to-break data which will be reported in a later *Summary*, are shown in Figure 17, where they are compared with the values predicted by the WLF equation (Ref 13):

$$\log a_T = \frac{-8.86(T - T_g)}{101.6 + T - T_g} \quad (6)$$

where T_g is the glass transition temperature. The agreement is rather good for the modulus data, but poor for the points from ultimate property data. The latter show a much greater dependence on T than does the WLF function. Since the reason for this discrepancy has not yet been established, the WLF curve is drawn for a best fit to the modulus results. T_g is estimated by this procedure to be -55°C vs an experimental determination of -59°C based on linear thermal expansion measurements.

Average $\log a_T$ values were read from Figure 17 and used to superpose the data of Figure 16 with the results

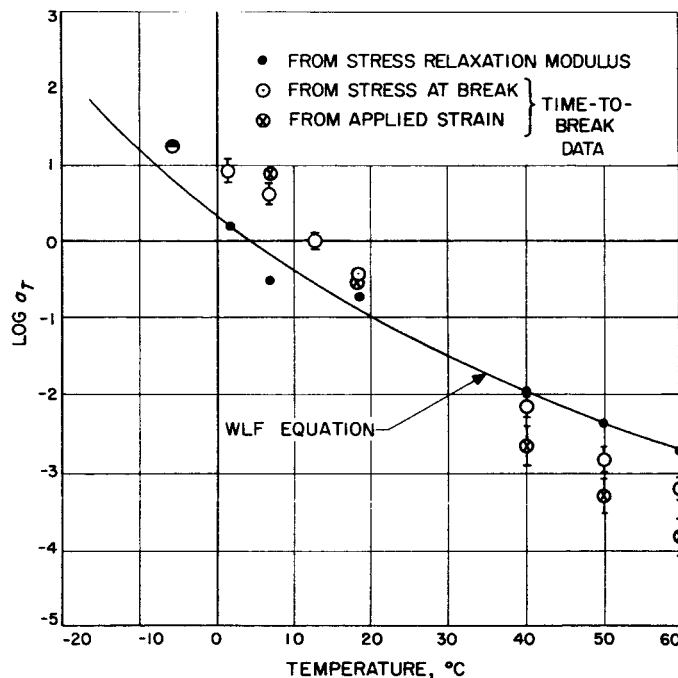


Figure 17. Comparison of experimentally determined shift factor a_T with values from WLF equation

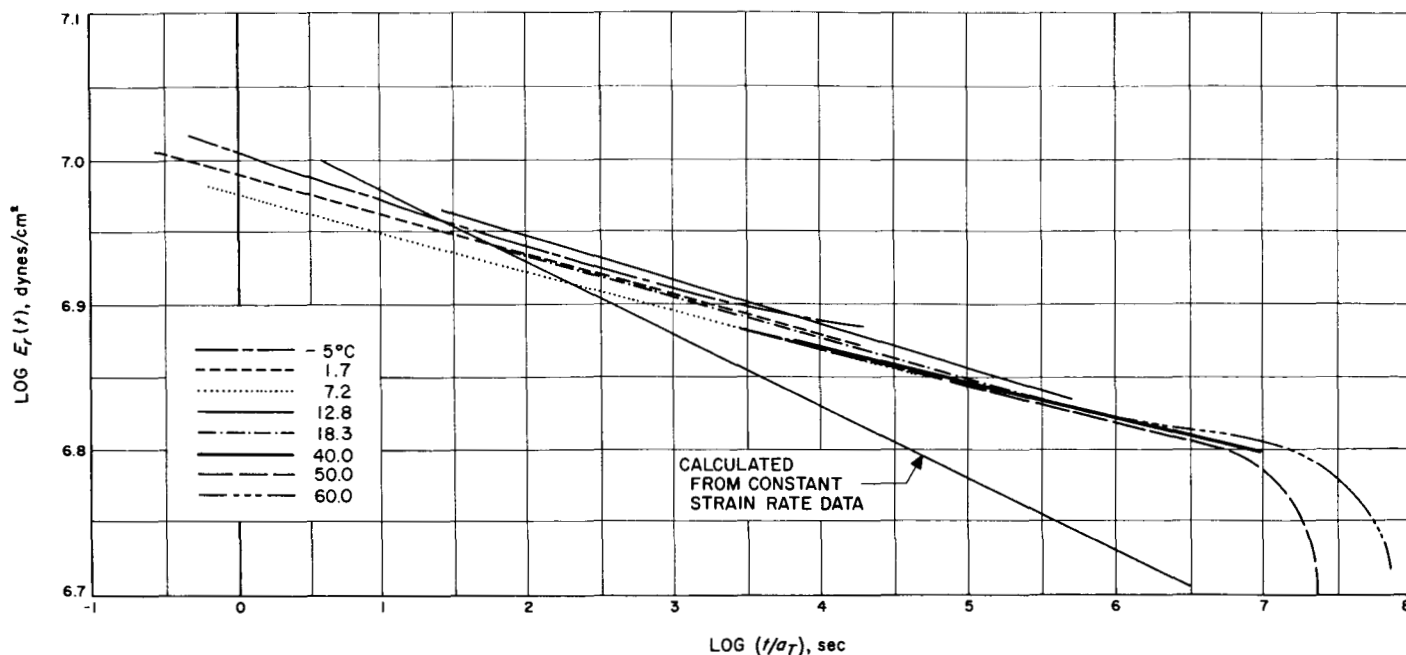


Figure 18. Superposed strain-reduced stress-relaxation modulus for SBR, reference temperature $T_0 = 286.0^\circ\text{K}$

shown in Figure 18. The sharply decreasing portions of the 50 and 60°C curves do not superpose, as indeed they cannot if the effect is due to degradation. The curves are too flat to afford a positive test of superposition. A better test can be made by comparing modulus data obtained at different ranges of the real time scale. The stress-relaxation modulus calculated from reduced constant strain rate data is included in Figure 18 for this purpose.

The stress-strain data can be superposed in the original manner of Smith (Ref 12) to give a composite stress-strain curve by plotting $\log \alpha S T_0 / R a_T T$ vs $\log e / R a_T$, where R is the strain rate. Thus the strain-reduced stress is αS . Figure 19a shows the results from such a superposition, using a_T values calculated from the WLF equation, with $T_0 = 59^\circ\text{C}$. The individual stress-strain curves are concave upward and their initial portions define the envelope of all the curves, as previously noted by Smith. In the present instance, the envelope is essentially a straight line over this region of the reduced time scale.

The MRS equation can be used similarly to reduce the data, except of course that $f(\alpha)$ in the reduced stress is equal to $(1/\alpha^2) \exp 0.40 (\alpha - 1/\alpha)$. The superposed plot thus obtained is shown in Figure 19b. The MRS function has now converted all of the stress-strain curves into straight line segments, and practically all of the points lie on a single line. This line is the same as the envelope in Figure 19a since, at low strains, $f(\alpha)$ is unity. The stress-relaxation modulus $E(t)$ can be obtained from the slope

of either of these plots at any desired value of reduced time $t_r = e / R a_T$, as

$$E(t) = (S^* / t_r) (d \log S^* / d \log t_r) \quad (7)$$

If the use of the reduced stress concept and the MRS equation is correct, then these values of the stress relaxation modulus should fall on the superposed curve of Figure 18. Instead, the results from constant strain rate data cross over and fall progressively below the superposed curves. When it is considered, however, that the maximum discrepancy between the two results is 0.1 log unit, no more than the diameter of the data points shown in Figure 19, then the agreement can be considered to be satisfactory.

d. Conclusions. Since experimental data obtained at quite different times, temperatures, and strains showed reasonable agreement, it may be concluded that the concept of strain-reduced stress as a reduced variable is generally valid. Thus Ferry's method of reduced variables may be extended to large deformations by employing a strain-reduced modulus $E(t) f(\alpha)$, where $f(\alpha)$ is an appropriate function of the strain. Such a function was obtained from the Martin-Roth-Stiehler equation, but the validity of its use in this reduction was not definitely established. The constant A in the MRS equation is clearly related to the finite extensibility of polymer chains, since its magnitude controls the rate of rise of stress at higher strains. The implications of a possible time and temperature dependence of A are not clear at this time.

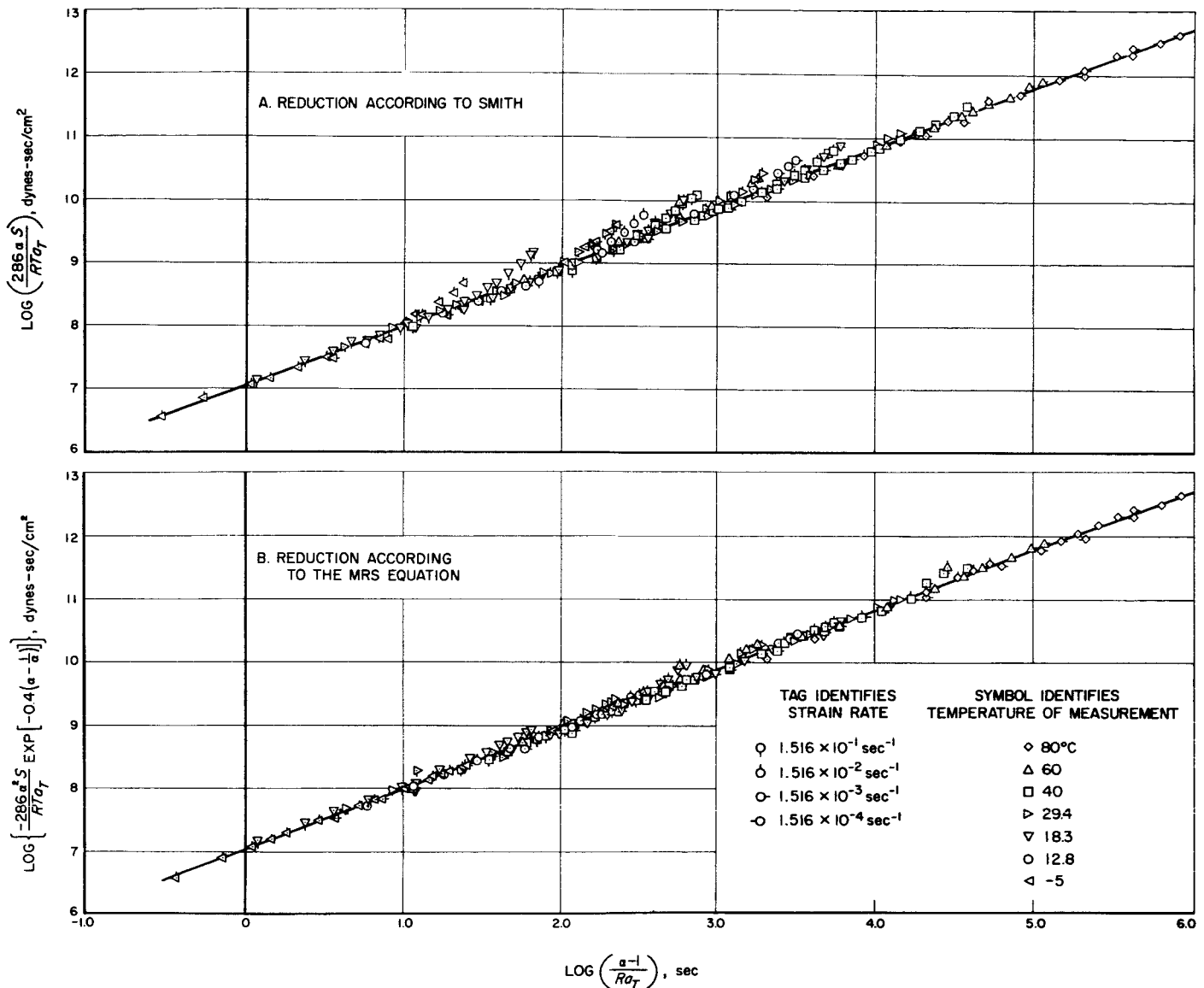


Figure 19. Composite stress-strain curves for SBR, reference temperature $T_0 = 286.0^\circ\text{K}$

B. Thrust Vector Control of Solid Propellant Rockets

One of the major problem areas in solid-propellant rocketry has been that of providing command control of the thrust vector. The Laboratory has initiated a research and development program to reduce to engineering practice a promising method for thrust vector control.

1. Methods of Thrust Vector Control

A brief consideration was given to the various means of vectoring a solid propellant rocket. Devices which have been developed, are being developed, or can be conceived to effect vector control, include the following:

- (a) Jet vanes
- (b) Jetavators
- (c) Swivel nozzle with 1-degree freedom
- (d) Swivel nozzle with 2-degree freedom
- (e) Secondary fluid injection, such as hot gas injection, cold gas injection, or liquid injection

- (f) Venting of main chamber gas through fixed ports located at nozzle end, at nozzle entrance section, or at nozzle divergent section
- (g) Auxiliary cold gas jets
- (h) Auxiliary hot gas jets from a solid propellant or liquid propellant
- (i) Eccentric rotating nozzle
- (j) Venting of main chamber gases through steering nozzles
- (k) Shifting vehicle center of gravity
- (l) Compound pendulum mounting of motor and payload
- (m) Jet paddles
- (n) Deflection by magnetic or electrical forces

2. Secondary Fluid Injection

In the process of selecting a fruitful area of investigation of the problem of vectoring solid propellant rockets, consideration was given to the fact that most presently anticipated spacecraft applications of solid propellant units will require only small vectoring angles. The purpose generally would be to correct for thrust axis misalignments because of such eventualities as ablating nozzle throats or spacecraft pointing errors at the time of motor ignition. Large angle maneuvering will probably not be done with main thrust on.

The attempt to deflect the main jet by injecting a fluid into the divergent portion of the nozzle has been tried by various agencies and industries with erratic results during the past decade. Most recently, the Naval Ordnance Test Station at China Lake has done extensive work with the secondary injection of liquids and has demonstrated the practicality of this method of vector control (Ref 14). Secondary injection is ideally suited to applications where relatively small vectoring angles (5 deg or less) are required. By proper design and development, it is also possible to obtain roll control with injection into a single nozzle. Furthermore, unlike jet vanes, jetavators, and jet paddles, the injection of secondary fluids involves no hardware to be exposed to the blast of the nozzle exhaust. Therefore this system is not limited in its applicability in the near future when propellant combustion gases are of ever higher flame temperatures and have contaminating and condensable atmosphere. Lightness in component weight and simplicity of control and operation are other merits of secondary injection. Secondary injection, therefore, appears at present to be the best method to investigate, develop and advance to the stage of applicability.

3. Tentative Secondary Injection Program

The tentative plans are to complement and extend the types of secondary injection experiments that have been conducted at NOTS. Effort will be made to acquire more engineering design data (such as injection geometry and the optimum operating parameters), and to study injectants of higher specific impulse. Furthermore, roll control will be investigated.

A two-component thrust stand has been designed and constructed for the measurement of axial and one-side forces (Fig 20). Early testing with the injection of water has been done with this stand. In the near future, a six-component stand will be available for more complete thrust measurements. A scale-*Sergeant*-sized motor will be used which provides a nominal thrust level of 1200 pounds at a chamber pressure of 250 psia and a burning time of approximately 10 seconds.

A bread-board fluid injection system has been fabricated, and two successful firings have been conducted using water as the secondary fluid. A digital computer program is currently being written to reduce the data and present it in a useful format. Tests will be run in the

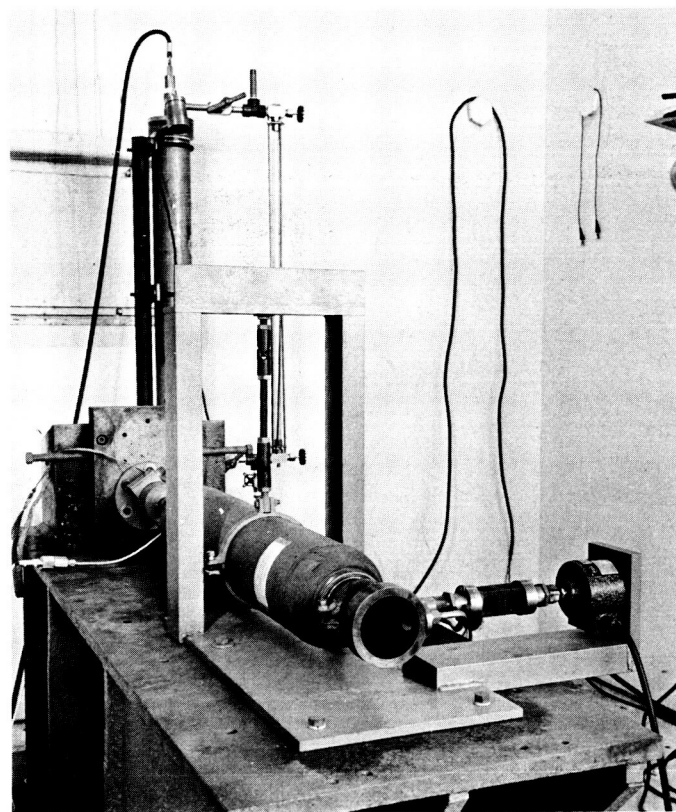


Figure 20. Thrust stand for measuring axial and one-side forces

near future utilizing Freon 12 as the injectant. Later experiments will test the injection of a liquid monopropellant like hydrazine. Results of the tests conducted and some associated theoretical considerations will be presented in future *Research Summaries*.

C. Materials Evaluation for Solid Propellant Rockets

1. Ablative Throat Materials (Dumont)

An investigation of ablative materials to determine the feasibility of ablative nozzle throats has been initiated as a joint effort by the Laboratory and the Dumont Corporation. Ablative materials, in both the compression-molded and the grain-oriented form, are attractive for solid rocket applications, being light in weight and having low thermal conductivity. Six promising compositions were selected by the Dumont Corporation for the initial phase of this program.

An ablative material, to be acceptable for a nozzle throat application, has to conform to the following requirements: (1) The material must *swell* or *erode* uniformly causing a minimum of thrust vector malalignment; (2) the *swelling* or *eroding* must not be excessive and should be predictable and uniform from part to part; and (3) the material must also be capable of withstanding thermal shock and pressure forces in a flight design configuration.

a. Testing methods and type of data collected. The test motor used in testing the various phenolic-filled materials consisted of general heavy hardware fixtures. These fixtures included a 13.5-inch-long 5-inch-ID section of Shelby tubing threaded at both ends, a heavy head-end plate, and a nozzle retaining fixture. The nozzle (Fig 21) was held in the nozzle retainer by using a steel ring and set screws. The Shelby tubing was lined to 0.1-inch thickness with a polyurethane liner. A solid charge was then cast into this chamber, trimmed to length, and flush-plugged on one end. This end-burning motor was designed to operate at approximately 260 psia for about 44 seconds. A 2% aluminized propellant with a flame temperature of 4850°F was used in all tests. Test conditions, except for duration, were chosen to correspond to those of the *Starfinder* motor, into which the most successful material will be incorporated.

All nozzles tested were inspected both prior to and after firing. Linear erosion rate data was taken at Stations 1, 2, and 3 (Fig 21) by measuring diameters of each station

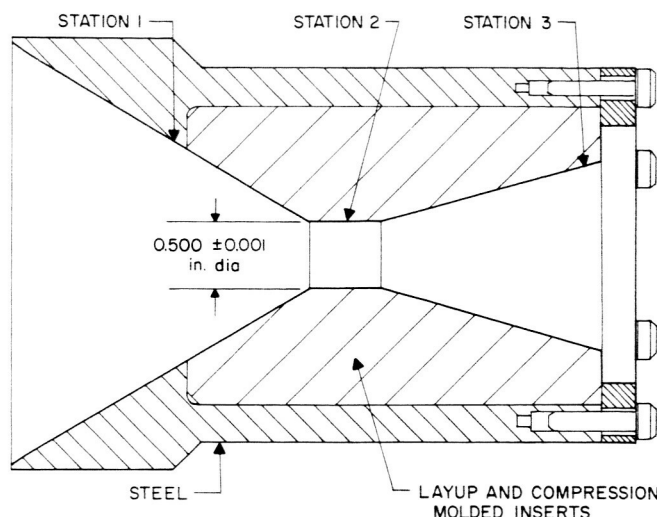


Figure 21. Cross-section view of Dumont test fixture

before and after firing and dividing the differences by the motor burning time. The nozzles were sectioned to determine the depth of char in the material (Fig 22). The

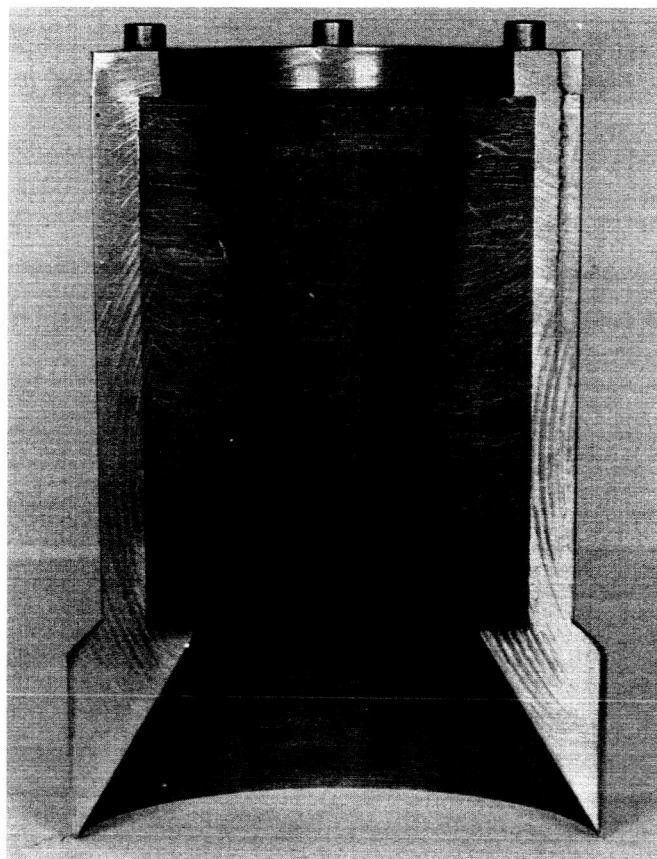


Figure 22. Typical char layer on Astrolite ablative test throat using 2% aluminized propellant

nozzles were weighed prior to and after firing to determine the weight of material ablated. Particular emphasis was placed on throat inspection to determine any ovality caused by unsymmetrical ablation.

b. Test results and conclusions. All of the materials tested retained structural integrity for the complete firing. Aluminum oxide was not present on the surface of any of the materials at the end of the tests. Eccentricity of the nozzle throat after firing was evident when the nozzles were shadowgraphed. This eccentricity was very slight and could not be measured accurately because of nozzle design. The char layer was not clearly defined in any of the materials. This layer for the Astrolite materials was approximately 3/16 inch at the throat and of slightly less

depth both upstream and downstream (Fig 22). The materials containing graphite appeared to have a greater depth of char. No correlation between linear erosion rate and weight ablated could be determined. Materials 1 through 4 were selected for further testing on the basis of throat erosion rate (Table 7). These four materials will be tested in the same type nozzle under similar conditions. Thermocouples will be imbedded to different depths of the material at several stations along the nozzle. The comparison of erosion rates between the above tests and the proposed tests will give an indication of the reproducibility of the material. The thermocouple data will allow the determination of the thickness of material required for an optimum design.

Table 7. Erosion data for ablative throat materials by Dumont

No.	Material	Specific gravity	Resin, wt %	Erosion rate, ^a in./sec			Change in A_{10}	Material ablated, lb	Change in weight, %	Test duration, sec	Average pressure, psia
				Station 1 $M_0 = 0.06$	Station 2 $M_0 = 1.0$	Station 3 $M_0 = 3.08$					
1	120 deg laminated Astrolite F120 on C100-28	1.91	35.9	-0.00040	-0.00038	0.00000	-6.13	0.015	2.63	41	280
2	120 deg laminated (alternate layers) F120 on C100-28 & 91-LD graphite fabric	1.63	34.9	-0.00011	0.00016	0.00009	+2.96	0.020	4.08	44	260
3	120 deg laminated 91-LD graphite fabric	1.46	45.3	-0.00037	-0.00028	0.0002	-4.82	0.020	4.54	43	270
4	Astrolite chopped SC1008 on C100-28	1.82	30.0	-0.00017	-0.00046	-0.00002	-8.24	0.010	1.83	45	265
5	Fiberite X2626, Materite graphite with Refrasil	2.05	27.5	-0.00085	-0.00093	0.00000	-15.08	0.035	5.78	42	310
6	U.S. Polymeric XA-0-16-13 chopped graphite filled on graphite fabric	1.63	40.5	-0.00043	0.00079	0.00008	+15.15	0.025	5.15	46	240

^aMinus signs indicate negative erosion or swelling of material; M_0 is Mach number based on original area ratios.

Table 8. Composition and cure of ablative materials furnished by Hughes

No.	Material	Specific gravity	Resin, wt %	Phenolic filler composition	Cure data ^a	
					Cure temp, °F	Oven postcure ^b
1	Fiberite FM-1344-67	1.75	33	Quartz fibers, 67% quartz	300	17 hr at 275°F
2	Durez 16771	1.83	33	1-inch-long glass fibers	300	A-1 ^b
3	Fiberite FM-2549	1.91	—	Zirconia, graphite, and quartz fibers	300	A-1 ^b
4	Durez 19387	1.53	45	Quartz fibers	300	A-1 ^b
5	Fiberite OPX-197	1.69	—	1-inch-long glass fiber	300	17 hr at 275°F
6	Fiberite 4035	1.86	—	0.5-inch-long glass fibers	300	17 hr at 275°F
7	Fiberite FM-1801	1.63	—	Ceramic fibers	300	17 hr at 275°F
8	Fiberite FM-6500	1.70	—	Asbestos	320	17 hr at 275°F
9	Coast F-122	1.96	26	Chopped-glass fabric	320	17 hr at 275°F
10	U.S. polymeric 14802/101	1.79	34	Chopped-glass fabric	300	17 hr at 275°F
11	U.S. polymeric 14802/91-LD	1.76	37	Chopped-glass fabric	300	17 hr at 275°F

^aAll parts were press-cured for 15 minutes; molding pressure was 4000 psi for the convergent cone and 11,000 psi for the divergent cone.

^bPostcure A-1 consists of 17 hours at 275°F followed by a gradual temperature rise to 400°F at a rate of 50°F/hr.

2. Compression-Molded Ablative Materials (Hughes)

An investigation of ablative materials in the compression molded form was instituted by the Laboratory and Hughes Aircraft Company. The objectives of this investigation were (1) to evaluate materials which can either insulate metal cases and nozzles effectively or else be used in their stead, and (2) to support the *Starfinder*, a high-performance motor now under development by the Laboratory.

a. Testing methods and type of data collected. The motor used in testing the various compression-molded materials (Table 8) consisted of the same heavy hardware fixtures and type of propellant charge described in the preceding section. A special nozzle assembly having a 0.465-inch-diameter throat was specifically designed for this test program (Figs 23 and 24). The motor was to operate at 280 psia for 42 seconds. A 2% aluminized propellant with a flame temperature of 4850°F was used in all tests.

The cones that were tested were weighed before and after firing to determine the weight and percentage of material ablated (Table 9). The linear erosion rate was determined at seven stations by measuring the thickness of the station before and after firing and dividing the differences by the motor burning time. Each station was inspected at two points 180 degrees apart, resulting in the two linear erosion rates reported for each station (Table 10). The test nozzle was equipped with thermocouples which monitored the temperature profile along the outer surface of the cones during firing.

b. Test results and conclusions. All materials performed well in the subsonic region. The glass-fiber-filled materials are less desirable, as indicated by the linear erosion

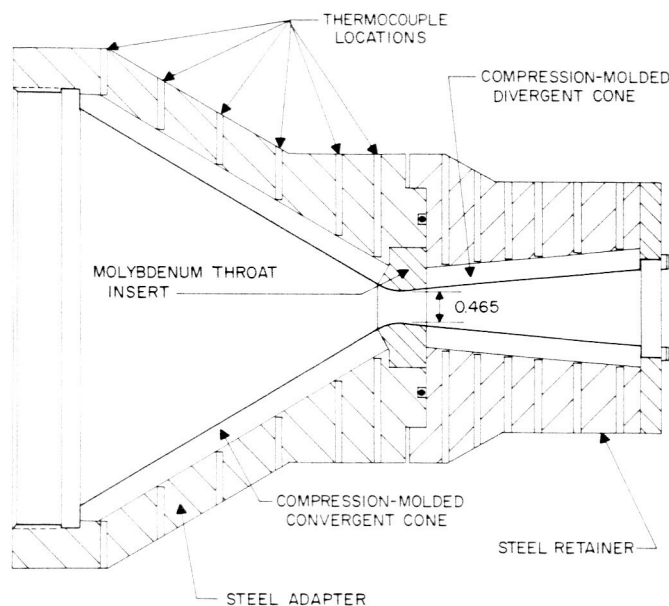


Figure 23. Cross-section view of Hughes test fixture

rate data (Table 10). This data shows that all but one of the glass-fiber-filled divergent cones failed. The linear erosion rate at $M_0 = 1.86$ and $M_0 = 2.21$ shows the effect of a change in material downstream of the throat for the glass-fiber-filled divergent cones (Fig 25). It is noted that this change in material (molybdenum throat insert to ablative divergent cone) did not cause an irregular erosion rate for any of the other materials. On the basis of this data, Materials 1, 3, 4, 7 and 8 appear to be the most desirable. Materials 1 and 3 *swelled* and gave a reasonably constant linear erosion rate for the full Mach number

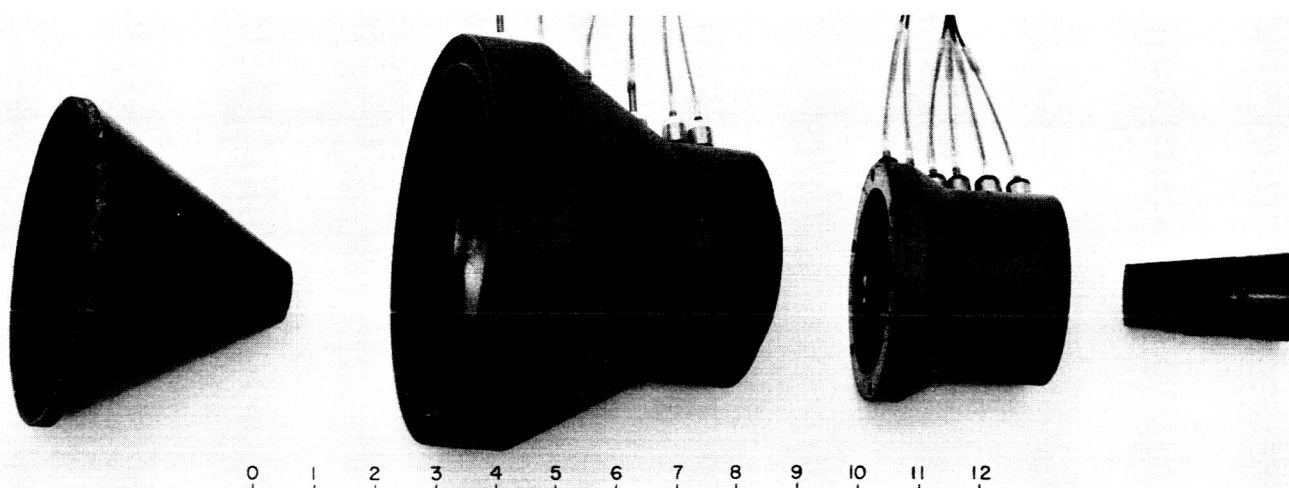


Figure 24. Nozzle assembly for testing ablative throat materials

Table 9. Erosion data for ablative throat materials by Hughes

No.	Material	Entrance cone weight			Exit cone weight			Average pressure, psia	Duration, sec
		Before, gm	After, gm	Loss, %	Before, gm	After, gm	Loss, %		
1	FM-1344-67	279.98	244.86	12.54	61.00	54.58	10.52	305	37
2	16771	283.87	236.92	16.54	64.12	45.16	29.57	325	37
3	FM 2549	303.61	273.95	9.77	68.51	59.79	12.73	285	43
4	19387	245.00	100.00	18.37	53.50	44.67	16.50	285	43
5	OPX-197	254.00	196.87	22.49	57.30	41.30	27.92	290	41
6	4035	284.00	219.15	22.83	65.80	32.82	50.12	320	40
7	FM-1801	261.00	211.41	19.00	58.60	50.26	14.23	285	41
8	FM-6500	263.00	314.64	18.39	61.50	48.55	21.06	325	37
9	F-122	306.00	256.00	16.34	68.40	29.45	56.94	360	38
10	14802/101	281.00	227.08	19.19	62.90	24.50	61.05	350	37
11	14802/91-LD	277.00	224.52	18.95	61.60	24.40	60.39	325	39

Table 10. Linear erosion rates at different nozzle stations

No.	Material	Erosion rate, ^a 10 ⁻³ in./sec							Appearance at end of run
		M ₀ = 0.019	M ₀ = 0.037	M ₀ = 0.145	M ₀ = 1.860	M ₀ = 2.210	M ₀ = 2.472	M ₀ = 2.687	
1	FM-1344-67	-0.08 -0.04	-0.14 -0.04	-0.14 -0.10	-0.05 -0.12	-0.05 0.12	-0.08 -0.02	-0.10 0.02	Relatively smooth contours, entrance cone cracked on removal from test fixture
2	16771	0.55 0.44	0.97 0.66	2.04 1.50	1.71 2.32	3.97 3.41	0.72 0.68	0.25 0.52	Bubbly surface in entrance cone, very erosive in low supersonic region
3	FM-2549	0.05 0.01	-0.01 -0.03	-0.02 -0.03	-0.04 0.00	-0.03 -0.01	-0.06 -0.01	-0.06 -0.02	Relatively smooth contours
4	19387	-0.13 -0.02	0.34 0.00	0.06 0.02	0.68 0.64	0.13 0.16	0.12 0.27	0.41 0.11	Relatively smooth contours
5	OPX-197	0.69 0.21	0.71 1.01	1.39 1.47	1.63 1.60	1.74 3.17	0.85 0.92	0.54 0.57	Bubbly surface in entrance cone, erosive in low supersonic region
6	4035	0.60 0.95	1.17 1.15	2.30 2.48	2.41 3.08	2.41 3.08	3.08 3.00	0.99 1.07	Bubbly surface in entrance cone, partial failure of exit cone
7	FM-1801	0.41 0.45	0.39 0.46	0.52 0.58	0.34 0.24	0.27 0.35	0.28 0.31	0.13 0.21	Relatively smooth contours
8	FM-6500	0.12 0.12	0.13 0.14	1.14 0.50	0.22 0.26	1.10 1.63	0.22 0.17	0.11 0.17	Relatively smooth contours
9	F-122	-0.10 0.21	0.07 0.36	1.60 0.44	3.84 3.86	5.34 6.55	2.65 4.11	1.68 1.67	Bubbly surface in entrance cone, complete exit cone failure
10	14802/101	0.44 0.37	0.44 0.37	1.39 1.47	3.53 3.25	7.90 7.90	3.99 3.87	2.63 1.29	Bubbly surface in entrance cone, complete exit cone failure
11	14802/91-LD	0.15 0.39	0.51 0.31	0.93 2.27	3.27 3.20	7.84 7.84	2.98 3.38	2.12 1.63	Bubbly surface in entrance cone, complete exit cone failure

^aNegative erosion indicates swelling of ablative material.

range tested. There was generally good correlation between the weight of material ablated and the linear erosion rate. The thermocouple data was reduced, and the temperatures recorded were below 300°F except for thermocouples which were exposed by a divergent cone failure. The temperatures recorded did not conform to the shape predicted by a typical heat transfer rate dis-

tribution. A proposed change in the installation of the thermocouples should yield reliable data.

Further testing will continue with the five materials which performed well. Additional testing of different materials will continue. Materials 1 and 3 are presently being incorporated into test nozzle exit cones for the *Starfinder*, *Mule*, and constant-pressure motors.

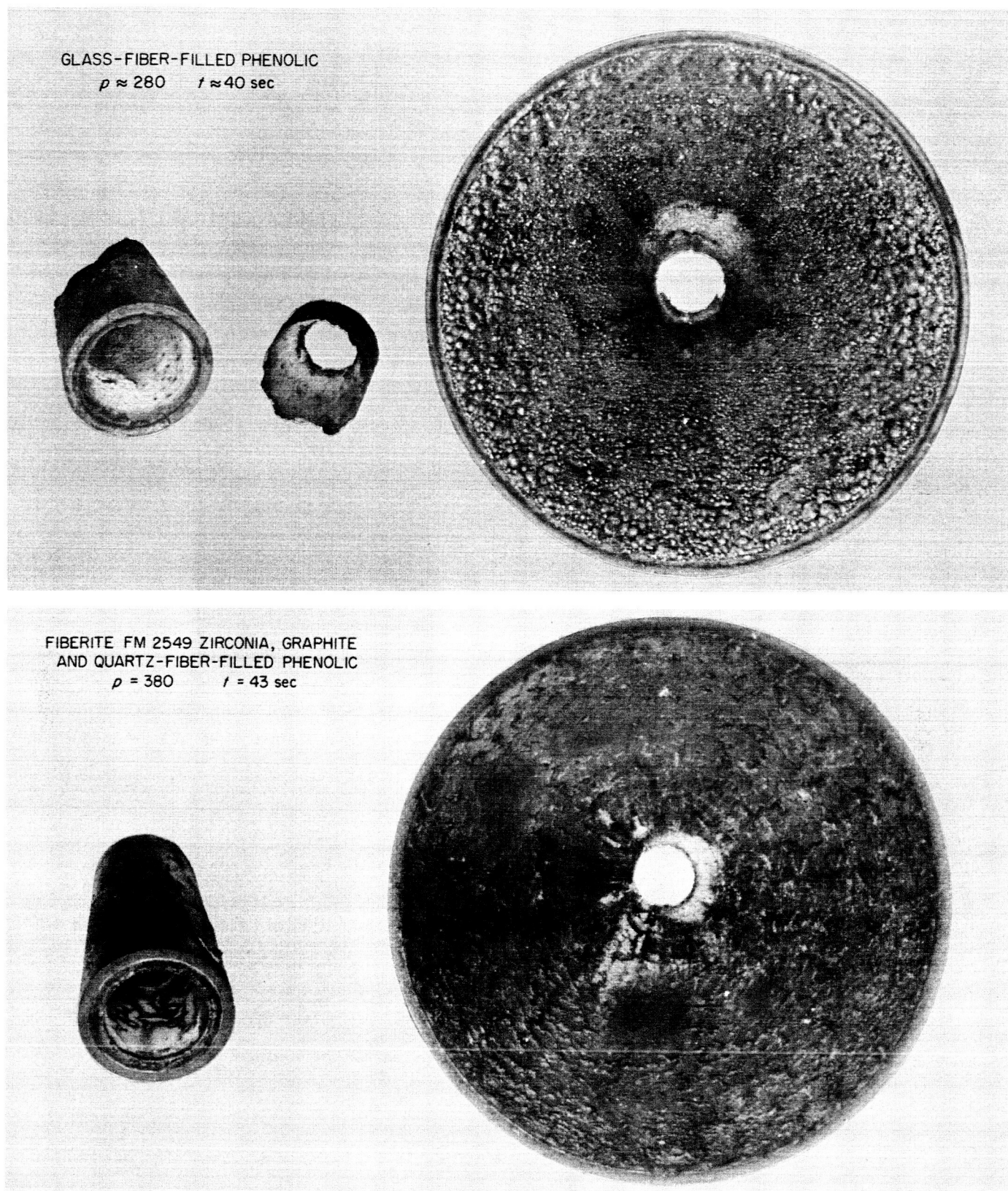


Figure 25. Typical surface and erosion pattern for filled-phenolic throats using 2% aluminized propellant

VI. LIQUID PROPELLANT PROPULSION

A. Combustion and Injection

1. Rocket Motor Injector Research

The experimental performance of Injector 5 of the rocket motor injector research program (CBS 66) has been obtained with a third propellant combination, i.e., $\text{N}_2\text{O}_4 + \text{UDMH}$. This series of data was obtained in an effort to further substantiate the applicability of non-reactive spray data as a basis for injector design (RS 1 to 6, CBS 66 and 68, and Ref 15). This is permissible since this particular injector design is near-optimum from the standpoint of producing uniform mass and mixture ratio distribution with these propellants at near peak performance mixture ratios, as required by the uniformity criteria (Ref 16). As a point of reference, it is noted that the injector configuration was actually optimized for *Corporal* propellants at a mixture ratio of 2.80. The data as presented in Figure 26 include the actual experimental results for thrust coefficients, specific impulse, and c^* , without correction for heat transfer or nozzle characteristics, as a function of mass fraction ratio. The c^* and I_s values are compared to theoretical data, taken from Reference 17; the expected value for thrust coefficient, 1.362, is based on a constant value for γ of 1.25, optimum expansion to 13.5 psia (ETS), and $\lambda \times C_D$ correction of 0.970.

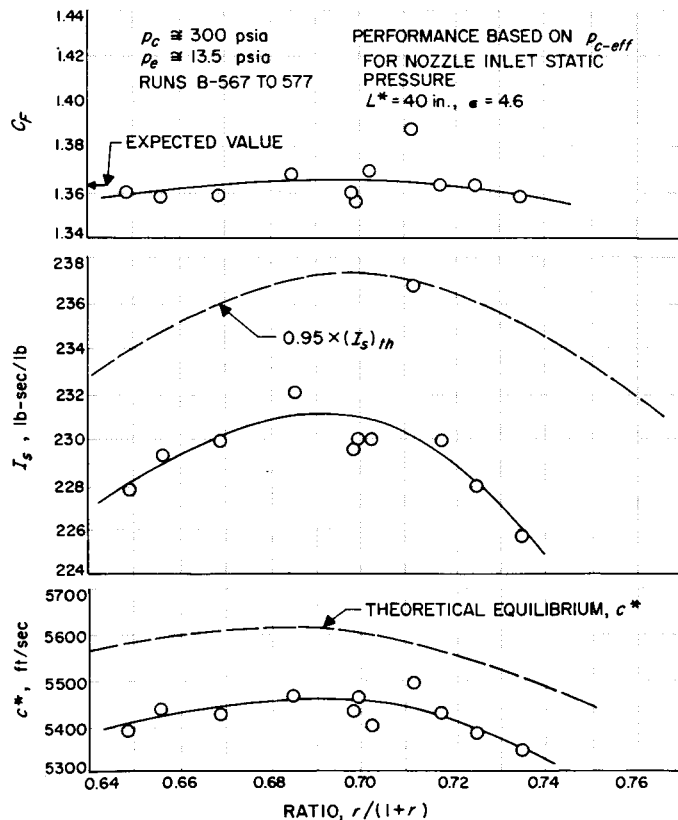


Figure 26. Experimental performance of Injector D-911206, i.e., Injector 5, with $\text{N}_2\text{O}_4 + \text{UDMH}$

Theoretical data for c^* and I_s for equilibrium conditions are also included for comparison, and it can be seen that the experimental values very nearly parallel these curves at levels of about 97.5 and 92.5%, respectively, for c^* and I_s . Thus, the level of performance achieved with this propellant system is essentially identical to that obtained with SFNA + UDMH (RS 6) and is only about 0.5% lower than that obtained with *Corporal* propellants for which the injector was designed. The data do, therefore, substantiate the conclusion that nonreactive data can serve as a logical basis for injector design and, further, that near-optimum conditions are achieved with near-uniform mass and mixture ratio distributions.

It was previously noted that these demonstrations would be conducted on the *Corporal* system in order to utilize the available background information and test hardware (CBS 66). This approach is permissible since the nonreactive data do not include the supplementary effects on mass and mixture ratio distributions that will be introduced by the chemical characteristics of a propellant system. These effects must include phenomena such as liquid phase reactions, liquid-to-liquid heat transfer, and as postulated in Reference 18 and in CBS 68, the influence of gas evolution at a liquid-liquid interface produced by a pair of unlike impinging streams composed of *extremely reactive* propellants.

As noted in CBS 68, this latter postulate was generated in order to rationalize certain difficulties that were encountered at this Laboratory in 1957 and 1958 in the course of developing a high-performance injector of the impinging stream type for the propellant systems $N_2O_4 + N_2H_4$ or $ClF_3 + N_2H_4$. Initial testing with these systems yielded poor performance and unstable combustion and led to a series of open flame tests which provided the basis for the following conclusion: "The successful operation of the very reactive systems $N_2O_4 + N_2H_4$ and $ClF_3 + N_2H_4$, however, appears to require special techniques for obtaining uniform penetration of the hydrazine into the oxidizer. . . . With impinging streams, this effect can be accomplished through the use of a splash plate or by means of some other method of forced secondary mixing" (p 26 of Ref 18). This resulted in abandonment of the impinging stream idea as the basis for an injector design for that development program.

The fact that these conclusions and their results implied a significant limitation on the use of nonreactive data as the basis of injector design precipitated a re-evaluation of the data upon which they were based. Some additional experiments were performed with open flames of $N_2O_4 + N_2H_4$. As a result of this re-evaluation, it was concluded that open flame tests (1) are not conclusive with respect to the combustion effects at the impingement

point, (2) are subject to individual physiological interpretation, and (3) do indicate that the resultant distribution is, at least in some instances, similar to an analogous nonreactive spray. Thus it appeared that the conclusions suggested in Reference 18 might be premature and, further, that there was some justification in believing that nonreactive information could serve as a logical design basis.

Therefore, a new injector design has been completed which utilizes nonreactive spray data as the basis for achieving uniform axial mass flow rate and uniform mixture ratio distribution at the peak performance mixture ratio for the propellant system $N_2O_4 + N_2H_4$. It is noted that a new design was necessary in order to satisfy the uniformity criteria (Ref 16) for this system since there is a substantial change in peak performance mixture ratio and, therefore, Injector 5 is not suitable. The new physical design that evolved (Fig 27) is similar to that of Injector 5 (RS 4) since the same design concepts which incorporate 100 L/D orifices and flexible orifice-to-manifold coupling lines were used in both cases. On the other hand, the axial mass flow rate distribution that is inferred from nonreactive data and is presented in Figure 28 is significantly different from that produced by Injector 5. This is to be expected since the geometrical details that are required to give near-uniform mass and mixture ratio distribution at the model plane are significantly different. The pertinent geometrical properties of the new injector (identified as Injector 7) and its elements can be summarized as follows:

- (a) Propellant system, $N_2O_4 + N_2H_4$
- (b) Design mixture ratio, 1.203 for peak equilibrium I_s
- (c) Total nominal thrust, 20,000 pounds
- (d) Number of elements, 47
- (e) Thrust per element, 425 pounds
- (f) Orifice diameters for both fuel and oxidizer, 0.173 inch
- (g) Orifice L/D ratio for both fuel and oxidizer, 100
- (h) Impingement angle, 45 degrees

In an effort to obtain an earliest possible evaluation of the performance characteristics of this injector, the bulk of the usual hydraulic evaluation was bypassed. A series of four tests was conducted at Edwards Test Station utilizing the same uncooled *Corporal*-like hardware as had been used for previous tests.

The performance data obtained in these four tests are summarized in Table 11. Although the data do not establish a complete curve and are subject to later verification (i.e., after the hydraulic properties are verified), it can be seen that reasonable performance levels were achieved.

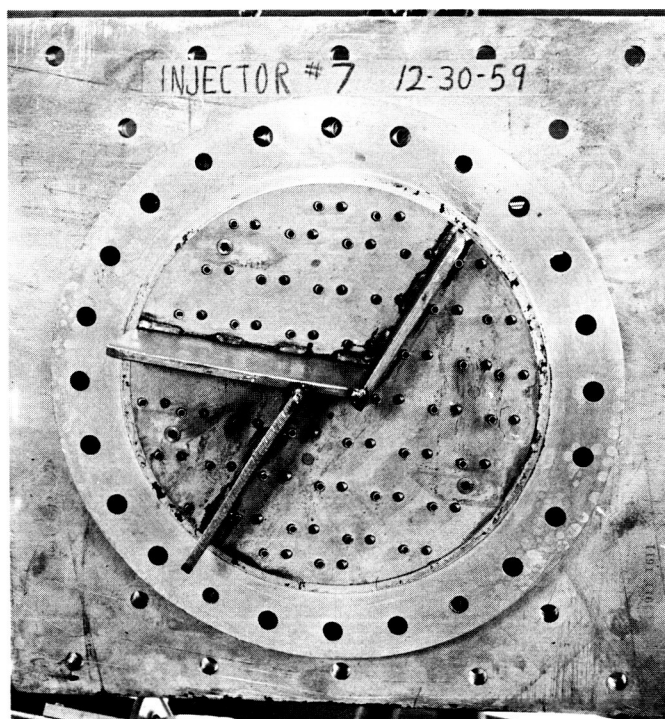
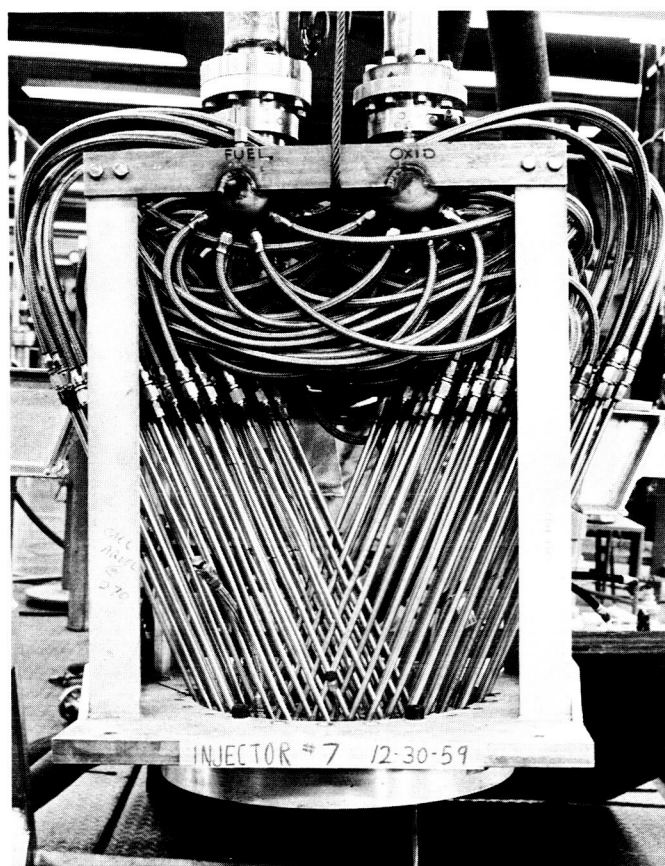


Figure 27. Injector 7 with vanes added, D-9111607

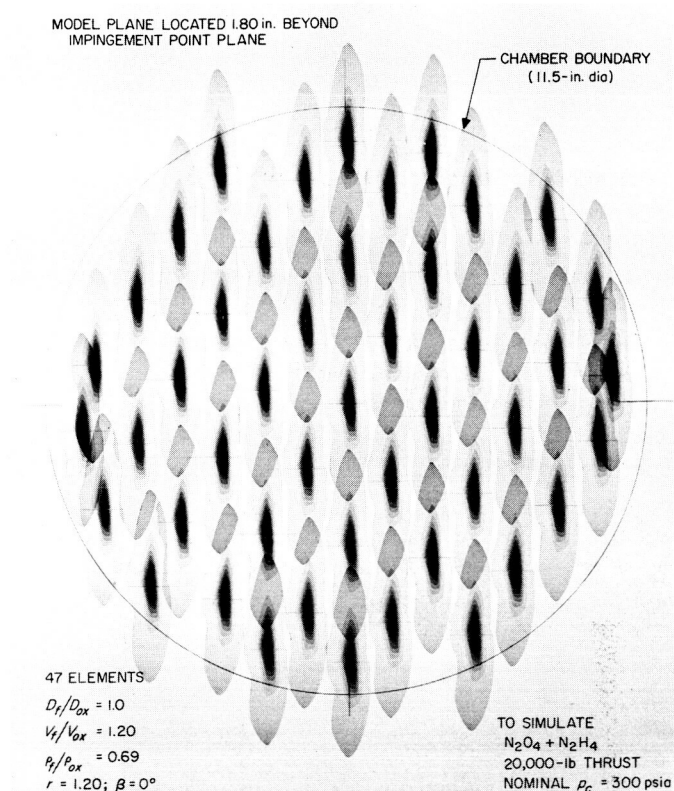


Figure 28. Composite model of near-uniform mass distribution obtained with Injector 7, D-9111607

In particular, it is noted that the maximum observed c^* and I_s are 97.0 and 92.5%, respectively, of the peak theoretical value for shifting equilibrium (Ref 17) without correction for heat transfer or nozzle characteristics. It is interesting to note that these values are within 0.5% of the relative performance levels achieved with the previous injector-propellant systems.

Table 11, Experimental performance^a of Injector D-9111607, Mod 1, i.e., Injector 7 with vanes using $N_2O_4 + N_2H_4$

Run ^a No.	<i>r</i>	<i>c</i> [*]	<i>I_s</i>	<i>C_f</i>	% <i>c</i> _{<i>t h</i>} [*]	% <i>I</i> _{<i>s, t h</i>}
B-578	1.081	5596	237.4	1.366	96.0	92.6
B-579	1.084	5584	237.5	1.369	95.9	92.6
B-580	1.176	5570	234.7	1.356	95.6	91.3
B-581	1.003	5638	236.2	1.348	96.8	92.6

Test conditions: $(P_c)_{eff} = 300$ psia, $P_v = 13.5$ psia, $L^ = 40$ inches, $\epsilon = 4.6$, $F = 20,000$ pounds; performance based on $(P_c)_{eff}$ for nozzle inlet static pressure; $(C_f)_{th} \times 0.97 = 1.362$ for $\gamma = 1.25$; c^* and I_{sp} not corrected for losses; theoretical equilibrium performance from Ref 17.

The heat transfer rates observed for these $\text{N}_2\text{O}_4 + \text{N}_2\text{H}_4$ tests indicated a significant increase in the average q to the chamber to approximately 3.5 Btu/in.²-sec, as compared to approximately 1.0 for $\text{N}_2\text{O}_4 + \text{UDMH}$ with Injector 5. There was also an increase in chamber pressure fluctuations to approximately 20 or 30 psi peak-to-peak as compared to 3 to 5 psi peak-to-peak for $\text{N}_2\text{O}_4 + \text{UDMH}$. This increase in chamber heat transfer can account for the 0.5% decrease in performance level as compared to the other systems that have been evaluated.

It has, therefore, been demonstrated (1) that at least in one particular design the unlike impinging stream element is suitable for injectors intended for use with the highly reactive propellant system $\text{N}_2\text{O}_4 + \text{N}_2\text{H}_4$; (2) that the performance level achieved during a *first test* at the 20,000-pound thrust level with a completely new injector design was very near the theoretical value, if appropriate corrections for losses are allowed, and (3) that nonreactive spray data *can* serve as a logical basis for injector design, even for the highly reactive propellant systems.

2. Chlorine Trifluoride-Hydrazine Motor Tests at 5000-Pound Thrust

Additional performance and heat transfer data for the ClF_3 (chlorine trifluoride)- N_2H_4 (hydrazine) system have been obtained in pursuit of the objectives described in

RS 36-1. Five 1.5-second tests were made using a motor having a 13-inch long mild steel combustion chamber and an uncooled copper nozzle. Four 5-second tests were made using a sectionally cooled thrust chamber assembly, shown in Figure 29, consisting of ten 1-inch cooled chamber sections, a 1-inch cooled mounting flange, and a nozzle having 16 separate water-coolant passages. The gas-side dimensions of the uncooled and the cooled thrust chambers were identical except for the combustion chamber length and a minor difference in the exhaust nozzle exit area. The injector used for this series of tests was a variation of the all-aluminum *multi-element modified showerhead* injector tested previously and described in RS 36-1, Figures 126 and 129.

Injector 62721 was used for the nine tests reported above (Figs 29 and 30). This injector has 14 cylindrical injector elements; each element has 12 fuel streams which are directed against the inside surface of a 1-inch diameter cylindrical splash plate, or cup, and 12 oxidizer streams which are directed against a central deflection post. The propellant streams are deflected to form sheets, as well as incidental spray, which partially mix and react in the protected area within the cup, and the propellant emerges in a predominantly axial direction. This variation of the injector element is designed to protect and cool each metal surface with a thin film of one propellant, with mixing occurring in the space between the cup and

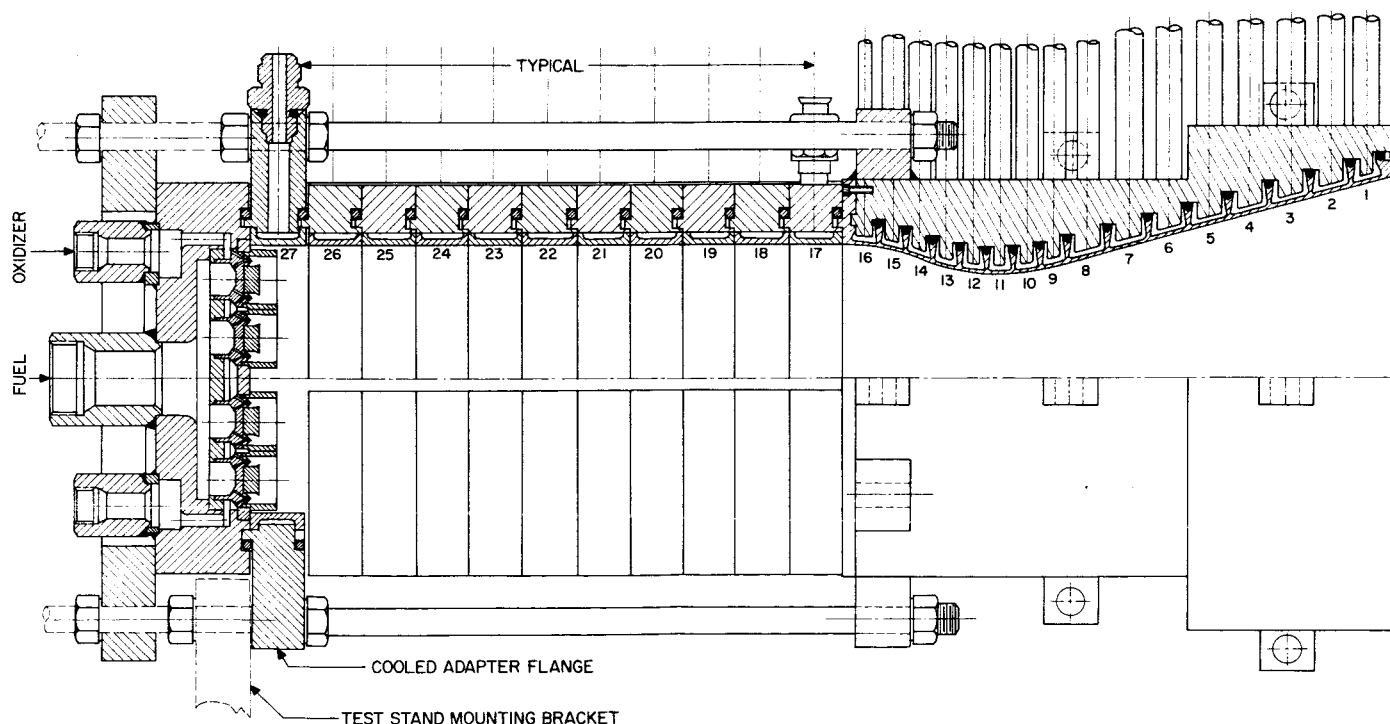


Figure 29. Assembly of sectional water-cooled motor and nozzle with multi-element Injector 62721

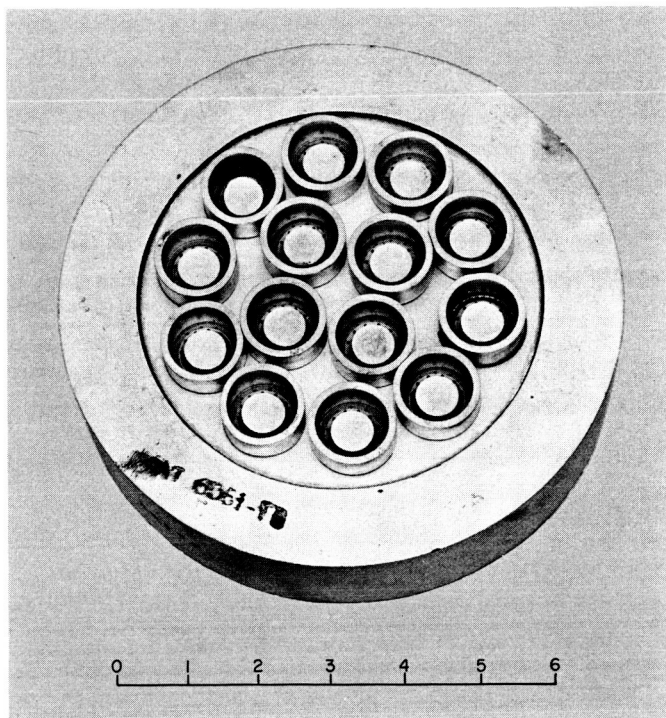


Figure 30. Fourteen-element Injector 62721 with central deflection posts in cylindrical combustion cups

the post. The nine tests thus far have not produced any burning of the type that caused failure of the two previous injectors (RS 36-1), though there is evidence of a slight surface attack on the ends of some of the aluminum cups.

The nine tests were made at a chamber pressure of approximately 300 psia, and covered a mixture ratio range of 1.79 to 2.27. Preliminary calculations of the performance obtained indicate specific impulse in the range of 235 to 241 seconds, with no appreciable difference between the cooled and the uncooled motor. Previous tests with the original version of the *multi-element modified showerhead* injector (RS 36-1) had given specific impulses as high as 245 to 250 seconds. The calculated shifting equilibrium performance of the $\text{ClF}_3\text{-N}_2\text{H}_4$ propellant is $I_s = 258.3$ seconds at $r = 2.6$ and 300 psia. It is believed that the major portion of the difference in performance obtained with the two injectors in similar thrust chambers is due to difficulties in measuring propellant flow rates. An extensive investigation of the techniques and instrumentation used in calibrating both cavitating and non-cavitating venturi flowmeters is now being carried out.

For the cooled tests, the water flow through and the temperature rise in each coolant passage in the combus-

tion chamber and exhaust nozzle was measured. From this data and the surface area of each section which was exposed to the combustion gases, the heat transfer rate to each section was determined. The temperature rise of the water passing through Sections 11, 16, and 26 (see Fig 29; the nozzle throat, the entrance to the nozzle, and the upstream section of the chamber, respectively) was measured directly on separate Speedomax recorders. Thermocouple outputs representing the temperature rise of the water passing through the other coolant passages were amplified and switched intermittently to two galvanometer elements of a CEC recording oscillograph. Because of difficulties in shielding the leads in the thermocouple wires, only the last of the four cooled motor tests yielded a near-complete set of heat transfer data. The heat flux distribution obtained on this test, made at a mixture ratio of 1.99, is shown in Figure 31. The heat flux in the downstream portion of the cylindrical combustion chamber is approximately 6 Btu/in.²-sec. The highest measured heat flux, 8.7 Btu/in.²-sec, was obtained two sections upstream of the nozzle throat; no data was obtained on this test from the section immediately upstream of the throat, where maximum nozzle heat flux is usually measured. The little usable data obtained from the Speedomax records of the first three cooled tests is in agreement with the data shown on Figure 31.

The heat transfer data for $\text{ClF}_3\text{-N}_2\text{H}_4$, which was obtained previously and reported in RS 5 (p 55 and Fig 68) and in RS 36-1, Vol I, was found to be incorrect

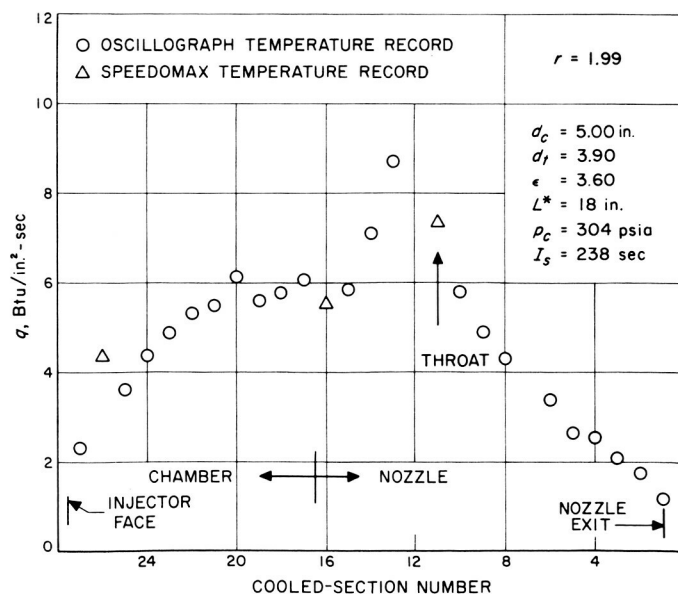


Figure 31. Experimental heat flux results obtained with sectional water-cooled motor, shown in Figure 29, using $\text{ClF}_3\text{-N}_2\text{H}_4$ propellant at $r = 1.99$

because of an error in the data reduction procedure employed. These data have been recomputed, and the corrected heat flux is shown in Figure 32. The previous tests were made with a similar, though not identical, injector and cooled motor, shown in Figure 33, and the heat transfer over the mixture ratio range of $r = 1.60$ to 2.02 ($5.2 \text{ Btu/in.}^2\text{-sec}$ in the chamber and $8.5 \text{ Btu/in.}^2\text{-sec}$ in the cooled section just upstream of the nozzle throat) is now seen to be consistent with the most recent data.

Heat transfer from $\text{ClF}_3\text{-N}_2\text{H}_4$ combustion products to the combustion chamber and to the nozzle throat of the thrust chamber shown in Figure 29 has been computed according to the enthalpy potential method pre-

sented in CBS 59 for propellant mixture ratios of 1.6 and 2.0 and chamber pressure of 300 psia. The computed values of heat flux, $q = 5.75$ and $8.60 \text{ Btu/in.}^2\text{-sec}$ to the chamber and throat, respectively, for $r = 1.6$ and $q = 6.20$ and $9.36 \text{ Btu/in.}^2\text{-sec}$ for $r = 2.0$, are in excellent agreement with the experimental data shown in Figures 31 and 32.

The thermocouple instrumentation and flowmeter calibration difficulties mentioned herein are being remedied, and additional performance and heat transfer data will be obtained in the next period, using both cooled and uncooled motors and injectors similar to the ones described here.

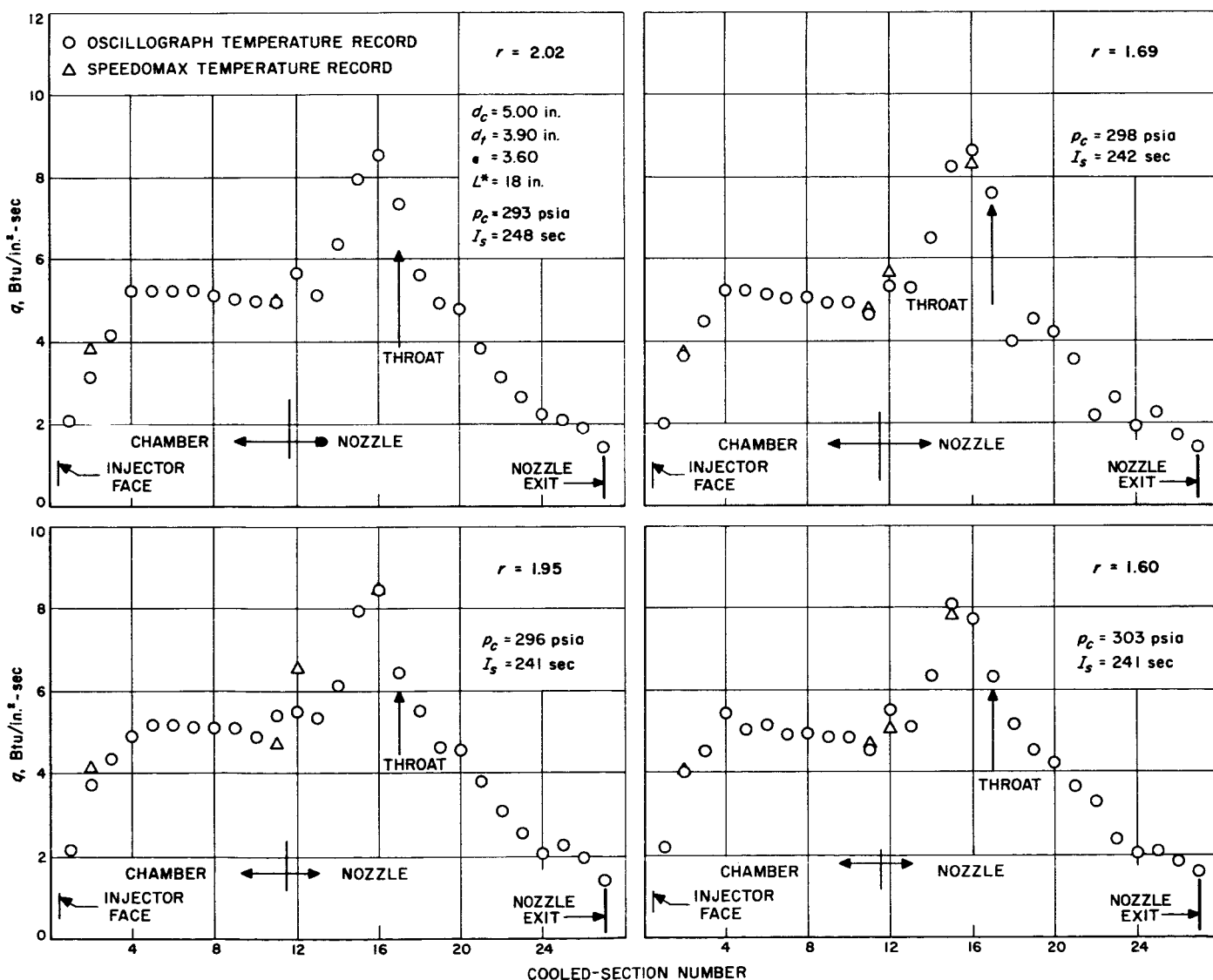


Figure 32. Recomputed experimental heat flux results obtained with sectional water-cooled motor shown in Figure 33, using $\text{ClF}_3\text{-N}_2\text{H}_4$ propellant at various mixture ratios

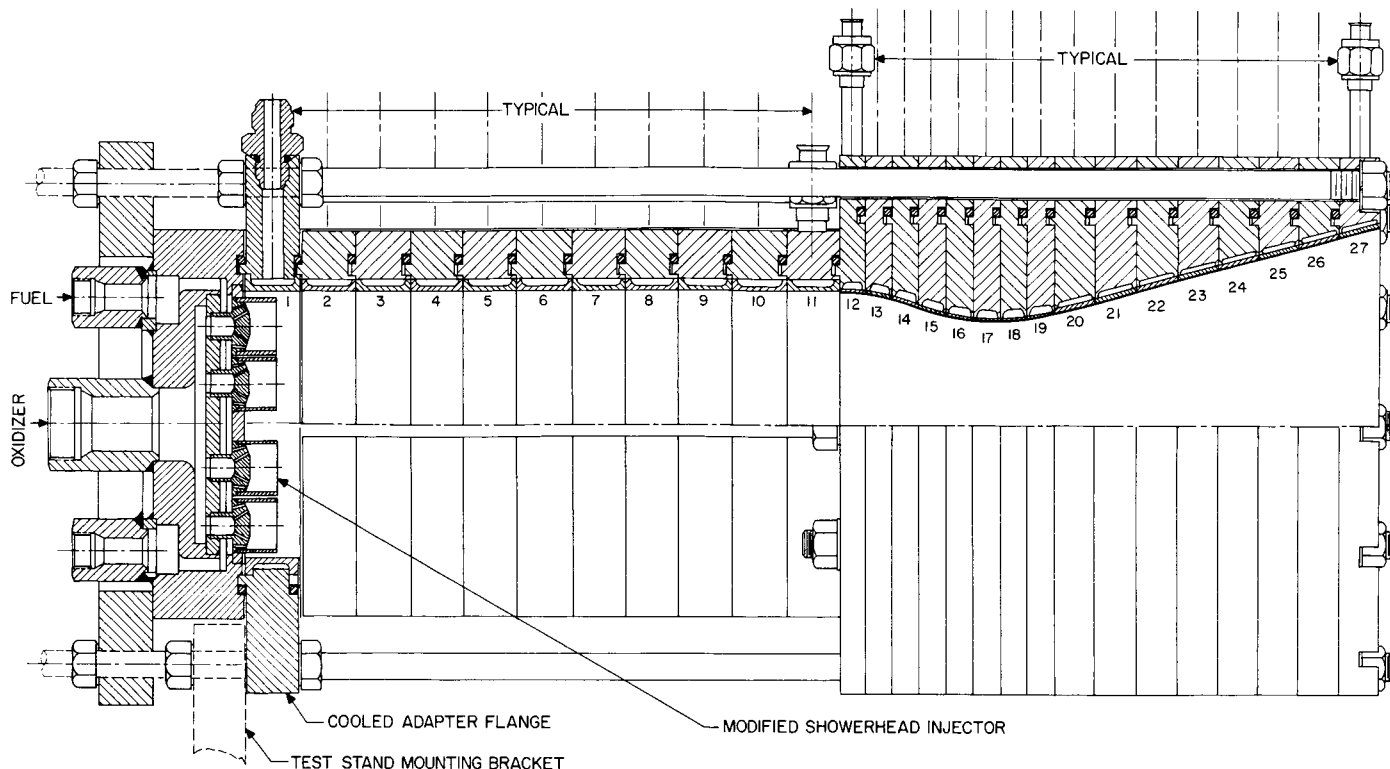


Figure 33. Assembly of sectional water-cooled motor and modified showerhead injector used in obtaining heat flux data shown in Figure 32

3. Nitrogen Tetroxide-Hydrazine Injector Elements

The program of advanced injector development has been primarily concerned with injector elements for the nitrogen tetroxide-hydrazine ($\text{N}_2\text{O}_4\text{-N}_2\text{H}_4$) propellant combination. The objective of the study has been to develop individual injector elements of low thrust which produce stable combustion chamber pressure, which have low overall injection pressure drop and reasonable heat transfer rates to the injector face and combustion chamber walls, and which produce high combustion efficiency in relatively short chamber length. It is intended that injector elements which show promise of meeting these requirements would be combined in a repetitive pattern to obtain larger thrust injectors.

Test results with the cylindrical-splash type of injector element under investigation at a sea-level thrust of 265 pounds have been reported in RS 6 (p 52) and RS 36-1. Tests of several modifications of these injector elements indicated that performance improved with increasing liquid propellant injection velocity, increasing splash-cylinder length, increasing number of injection orifices, and with the liquid propellant relative injection velocity (defined as the liquid fuel injection velocity minus the liquid oxidizer velocity, $V_f - V_o$) approaching zero. The

random, maximum combustion chamber pressure fluctuations decreased with increasing propellant injection velocity.

The experimental optimization program for the 265-pound sea-level thrust cylindrical-splash type of injector element has been concluded, and test results are reported here for the recent modifications tested. Injector element design parameters for these modifications are listed in Table 12 (for illustration of injector elements and design parameters, see RS 6, Fig 49). The objective of these modifications was to determine if satisfactory performance could be obtained with reduced overall injection pressure drop. To reduce liquid propellant injection pressure drop, all injector modifications listed in Table 12 incorporated contoured jet entrances. (Previous designs utilized sharp-edge entrances which required high liquid pressure drop for a given injection velocity.) Also, to reduce injection pressure drop, the liquid propellant injection velocity was reduced to 90 ft/sec for Injector Elements 1935-8, 1935-10, and 1936-8, and 75 ft/sec for Injector Element 1935-9. Since it was determined previously that performance falls off with reduced liquid propellant injection velocity, additional modifications to Injector Elements 1935-10 and 1936-8 were incorporated

Table 12. Cylindrical splash type injector element parameters^a

Injector	Propellant injection velocity, ft/sec	Impingement ^b angle, deg		Jet diameters, in.		Relative position of oxidizer and fuel jets
		Oxidizer	Fuel	Outer set, 8, oxidizer	Inner set, 8, fuel	
1935-8	90	10	30	0.039	0.047	Staggered
1935-9	75	10	30	0.043	0.052	Staggered
1935-10	90	15	40	0.039	0.047	Staggered
1936-8	90	10	30	0.039	0.047	In line

^aAll jets with contoured approach entrances.^bRS 6, Fig 49.

in the design in an effort to offset the expected loss in performance associated with the reduction of liquid injection velocity. The additional design modifications are as follows:

Injector Element 1935-10. The liquid jet impingement angles, with respect to the splash cylinder inner wall, were increased from 30 degrees to 40 degrees for the fuel and from 10 degrees to 15 degrees for the oxidizer.

Injector Element 1936-8. The fuel and oxidizer liquid jets impinge at the same point on the splash-cylinder inner surface; consequently, maximum liquid-phase mixing is promoted.

A schematic of Injector 1936-8 in Figure 34 illustrates the relative locations of fuel and oxidizer jets. All injector-element designs other than Injector 1936-8 utilize a staggered type of positioning of oxidizer and fuel jets (RS 6, Figs 49 and 50).

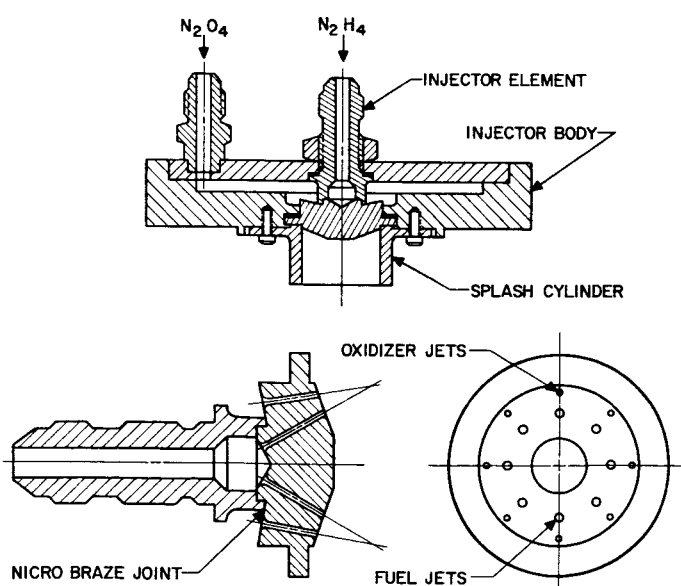


Figure 34. Schematic arrangement of 1936-8 injector element

A series of tests of 11-second duration over a range of mixture ratios r was made with the 1935-8, -9, and -10 injector elements and with the 1930-2, -3, and -4 splash cylinders (lengths of 0.45, 0.60, and 0.80 inch, resp; see RS 6, Fig 51a) using heated hydrazine (230 to 330°F) obtained by passing the hydrazine through a coil heat exchanger situated downstream of the nozzle exhaust. All tests were conducted at a chamber pressure of 150 psia using an uncooled chamber and nozzle. The characteristic chamber length L^* was 23.5 inches, and the nozzle contraction ratio ϵ_c was 2.78. It was found that the configuration modifications employed in Elements 1935-8 and -9 did not succeed in producing satisfactory performance with reduced pressure drop, whereas the performance of Element 1935-10 was found to be marginally satisfactory. The performance as measured by the characteristic exhaust velocity c^* , uncorrected for heat loss, for the Injector Elements 1935-8, -9, and -10 is presented in Figure 35. The characteristic exhaust velocities obtained for Injector Elements 1935-8, -9, and -10, all with the 1930-4 splash cylinder, at a mixture ratio of 1.0 were 4935, 5135, and 5440 ft/sec, respectively. The overall injection pressure drops from propellant manifold to chamber pressure at a total propellant flow rate of 1.05 lb/sec and a mixture ratio of 1.0 are given in Table 13 along with the individual liquid injection pressure drop and gas pressure drop across the splash cylinder. Random, peak-to-peak chamber pressure fluctuations observed for the injector elements were as follows: 1935-8 injector, 16 psi; 1935-9 injector, 16 psi; 1935-10 injector, ranging 10 psi ($r = 1.1$) to 30 psi ($r = 0.9$).

From the test results presented in Figure 35 and Table 13 it is seen that the performance obtained with Injector Elements 1935-8 and 1935-9 differs little from that previously obtained with the 1930-9 injector element with contoured approach jets (RS 36-1). The expected reduction in overall pressure drop was not realized primarily due to the increased gas pressure drop across the splash cylinder. This offset the reduction in liquid pressure drop accomplished by velocity reduction. The

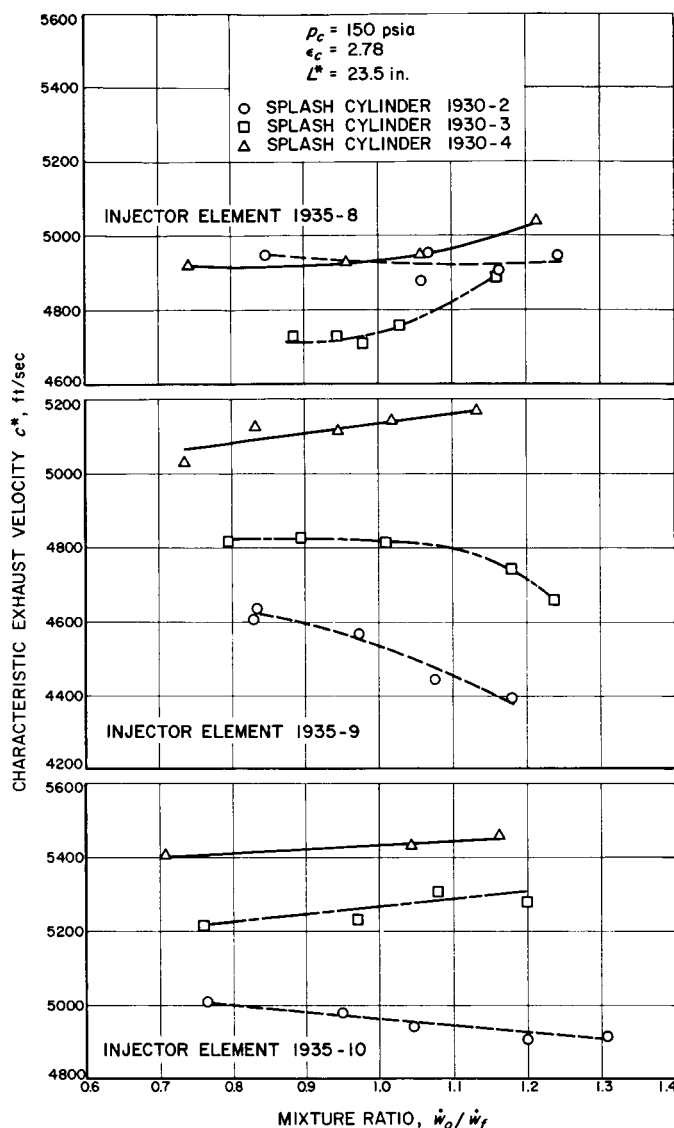


Figure 35. Experimental performance vs mixture ratio of 1935-8, -9, -10 injector elements with various splash cylinders using heated hydrazine at 230 to 330°F

increase in gas pressure drop was due primarily to more liquid phase reaction inside the splash cylinder. It was not possible to decrease this pressure drop by using a shorter splash cylinder length without also decreasing the performance substantially.

It can also be seen from Figure 35c for Injector 1935-10 that increasing the jet impingement angles to 15 and 40 degrees for oxidizer and fuel, respectively, had improved performance even though overall injection pressure drop was essentially equivalent to that of Injector 1935-8.

The 1936-8 injector element was tested with a 1930-3 and 1930-4 splash cylinder, and severe burning and melting of the splash cylinder and chamber walls occurred.

Table 13. Measured liquid and gas pressure drops for splash cylinder type injector elements with a 1930-4 splash cylinder^a

Injector	Liquid injection pressure drop, psi		Splash cylinder gas pressure drop, psi	Overall injection pressure drop, psi	
	Oxidizer	Fuel		Oxidizer	Fuel
1935-8	90	70	43	133	113
1935-9	65	45	40	105	85
1935-10	90	70	39	129	109
1936-8	90	70	70	160	140

^aValue of $r = 1.0$, $\dot{w}_{total} = 1.05$ lb/sec.

The pressure drop along the splash cylinder was exceptionally high compared to the pressure drops obtained with the other injectors; in Table 13 are shown the experimentally measured pressure drops across the splash cylinder and injection orifices. The characteristic exhaust velocities obtained with the 1936-8 injector using the 1930-3 and 1930-4 splash cylinders were 5520 ft/sec ($r = 0.85$) and 5320 ft/sec ($r = 0.73$), respectively. The higher performance obtained with the short splash cylinder is probably due to the higher gas pressure drop across that splash cylinder (87 psi compared to 70 psi; see Table 13). It has generally been observed that increased performance is associated with a high pressure drop across the splash cylinder, probably due to the improved mixing obtained through recirculation eddies in the main chamber. As a result of the severe splash-cylinder burning obtained with this injector element, no further tests beyond those mentioned above were attempted.

Tests of the 1930-9 injector element (RS 6 and 36-1) with the contoured jet entrances 1930-4 splash cylinder for combustion chamber lengths of 8, 12, and 16 inches are presented in Figure 36. These tests with a relatively low-performing injector element (as judged by the standard chamber, $l_c = 8.0$ in.) were made to determine the rate of performance increase with chamber length. This would indicate the maximum chamber length required at a given performance level for a multielement injector composed of these injector elements. The actual chamber length required would probably be less due to the expected performance gains from interaction between injector elements within the chamber. From Figure 36 it is seen that the c^* increase was 400 ft/sec, as chamber length was increased from 8 to 16 inches. A cross-plot of the data is shown in Figure 37 at selected mixture ratios to illustrate the variation of c^* with chamber length.

The overall results of the 265-pound-thrust splash cylinder type of injector element investigation can be sum-

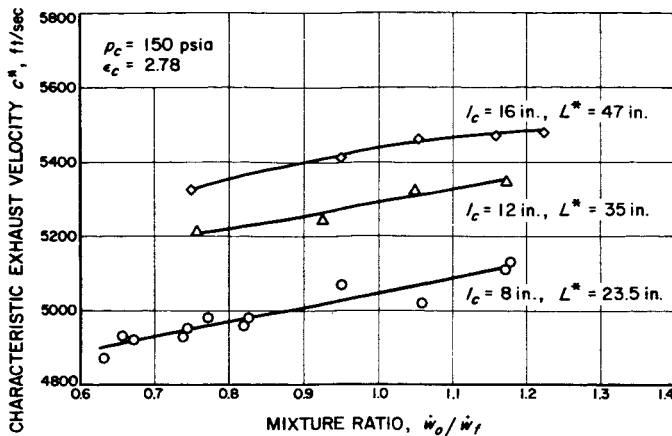


Figure 36. Experimental performance of 1930-9 (contoured jets) injector element using 1930-4 splash cylinder at various chamber lengths with heated hydrazine at 230 to 330°F

marized as follows concerning the importance of the parameters evaluated:

- Injection of the propellants in either the inner set or outer set of jets was unimportant as long as the relative velocity ($V_f - V_o$) was held approximately equal to zero. Oxidizer was injected through the outer set of jets for this investigation to enable cooling of the injector face of a multi-element injector with that propellant.
- High splash cylinder pressure drops improved performance through the mechanism of inducing

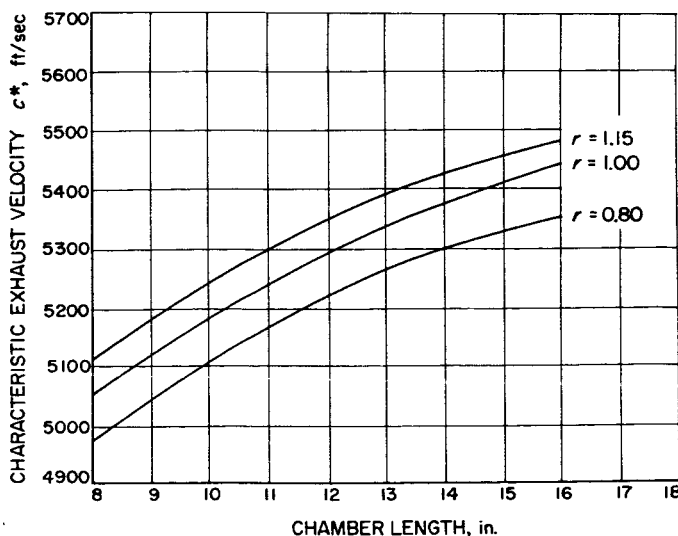


Figure 37. Chamber length vs c^* for 1930-9 injector element (contoured jets) using 1930-4 splash cylinder with heated hydrazine at 230 to 330°F

recirculation eddies in the main chamber. Splash cylinder length was important only insofar as it increased gas pressure drop across the splash cylinder. Longer liquid propellant residence times are obtained with long splash cylinders and, consequently, higher gas pressure drops due to increased chemical reaction. Conditions which promote increased mixing within the splash cylinders (i.e., *in-line* impingement, large impingement angles α and β) can provide equivalent gas pressure drops in shorter splash cylinder lengths.

- Increased turbulence level of the liquid jet (accomplished by providing sharp orifice entrances) for a given injection velocity increases performance significantly; large liquid pressure drops, however, are required.
- Increasing the number of injection orifices increased performance significantly for a given velocity level of propellant injection. This parameter was found to be the most important parameter investigated.

Due to the large number of variables affecting injector element performance (including fabrication tolerance), it was found that injector element performance could not be predicted in advance for a given set of design conditions. For incorporation into a multi-element injector of higher thrust, it is recommended that an injector element among the many configurations already tested be selected, since combustion instability or burning of the splash cylinder may be encountered with designs which fall outside the limits investigated. In particular, Injector Element 1937-8, reported in RS 36-1, is recommended since it yielded high performance (5640 ft/sec using heated hydrazine) and favorable combustion stability (average chamber pressure fluctuations, 10 psi peak-to-peak). The overall injection pressure drops for the 1937-8 injector element were 146 psi for oxidizer and 111 psi for the fuel. The important difference between this injector element and all others tested is that it injects propellant through twice as many injection orifices (32) as employed in all other designs. This injector element possibly would assure high performance when integrated into a multi-element injector (assuming no unusual combustion instability occurs). A multi-element injector of lower overall injection pressure drop than required by the 1937-8 injector element may be possible in the event that mutual interaction between injector elements was found to significantly aid performance. Then injector elements of lower performance and with low injection pressure drop could be employed.

In RS 1 (p 58) it was found that baffle plates attached to the injector face and extended some distance into the chamber had significantly reduced combustion instability.

The splash cylinder employed by the injector elements described above would also serve to isolate the initial liquid injection zones of each element in similar manner; consequently combustion instability may be prevented when these injector elements are employed in a multi-element injector.

4. Combustion Stability

During the early development phase of the 6K propulsion system, two regeneratively cooled runs of the engine were terminated by detonation of the hydrazine in the cooling jacket. These explosive decompositions took place well after the engine had reached steady-state operation (and was ostensibly operating smoothly), i.e., at 24 and 39 seconds. The failures occurred without apparent warning, the total coolant flow rate and chamber pressure being normal prior to burnout.

a. Possible causes of detonation. From an analysis of these tests it was postulated that one possible mechanism for the type of failure observed was transient flow instability in one or more of the cooling tubes. The instability is such that the flow rate through some of the cooling passages is reduced for a sufficient length of time to permit film boiling and subsequent decomposition of the hydrazine to occur. It was further postulated that this flow instability was induced by the low pressure drop (low damping factor) of the cooling jacket, which could permit severe coupling between the tubes of the thrust chamber. This coupling could lead to long-period beating so that flow cessation of appreciable magnitude, at relatively long time intervals, might occur. A theoretical and experimental program was developed to study the validity of the above postulates. If proven to be valid, criteria would be established for the specification of cooling-jacket pressure drop as a function of system parameters.

b. Experimental program. In order to quantitatively study the behavior of a multitube bundle configuration, a simplified model was constructed rather than attempting to instrument the actual cooling jacket. In the actual engine, four equally spaced entrance tubes feed the inlet manifold at the injector end of the thrust chamber. This manifold in turn feeds the 111 tubes comprising the cooling jacket, whose flow feeds a second manifold at the exit end of the expansion cone. The efflux from this manifold is fed through four equally spaced tubes (rotated 45 deg from the entrance feed tube positions), which terminate at the injector of the engine.

A model of this flow system was constructed with tubes having a hydraulic configuration equivalent to a 6K engine with a 3.5 expansion area ratio. However, rather than having 111 tubes the simulated jacket had only seven equally spaced tubes. The choice of seven tubes was

based upon the contention that any fewer would not represent a reasonable dynamic model due to the presence of the four inlet and four outlet tubes and their orientation, whereas a greater number would present increasingly difficult experimental and computational problems. The manifolds were sized to the same dimensions as in the actual engine, and the bundle tubes were dimensioned to yield approximately the same dynamic characteristics as those in the actual engine. Figure 38 shows the manifolds used in the program. Pressure taps were provided at all junctions of the bundle and feed tubes with the manifold. The completed bundle is shown in Figure 39.

As will be noted in Figure 39, an electromagnetic flowmeter (EMFM) is mounted in one of the bundle tubes at a position the throat would occupy in the actual engine. This region is of interest as the maximum heat flux occurs here and, therefore, it is most sensitive to flow disturbances.

In order to simulate chamber pressure oscillations, the outlet flow of the tube bundle is split. Part is dumped through a valve, while the rest is flowed through the siren shown in Figure 40. This siren produces a pressure oscillation which approximates a sine wave (from 0 to 3500 cps). By manipulation of the dump valve and a valve in the line to the siren, control is exercised over the amplitude of the pressure oscillation imposed upon the tube bundle. The inlet pressure to the bundle is maintained at a relatively constant pressure by the use of a large capacitance immediately upstream of the bundle. Figure 41 shows the overall test arrangement. The tube bundle in this photo is seen to be slightly modified by the addition of a turbine flowmeter in each of the seven bundle tubes. This revision was necessary in order to

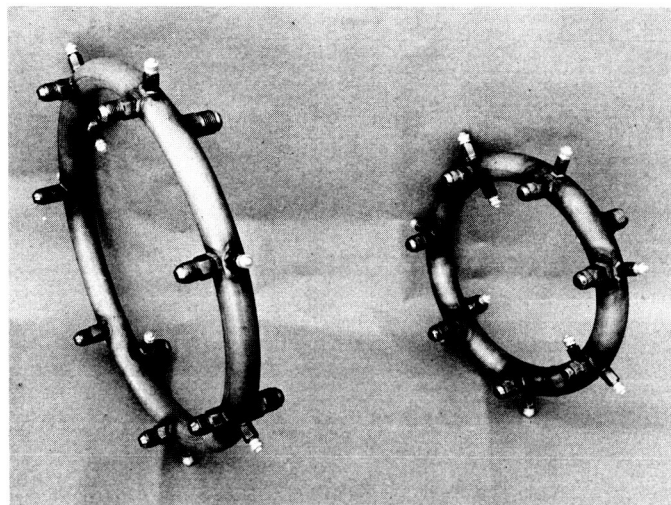


Figure 38. Model tube bundle manifolds

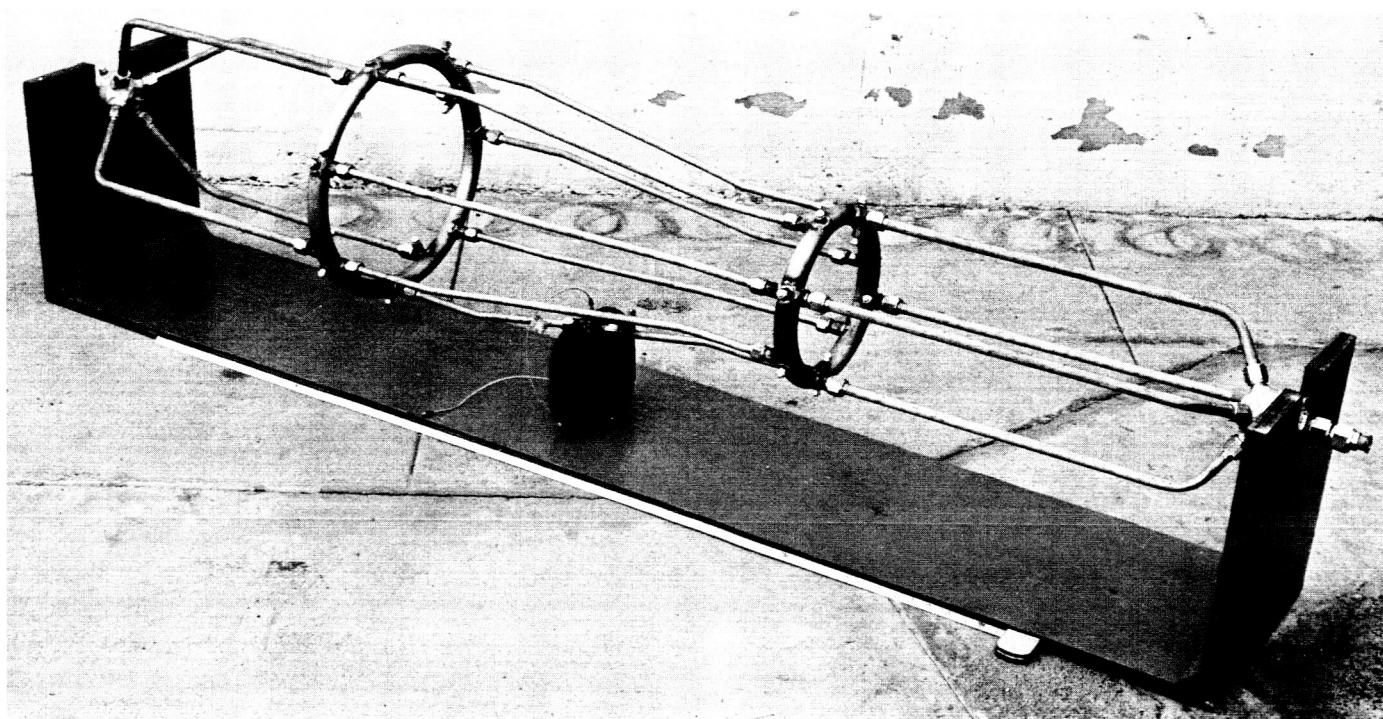


Figure 39. Model tube bundle

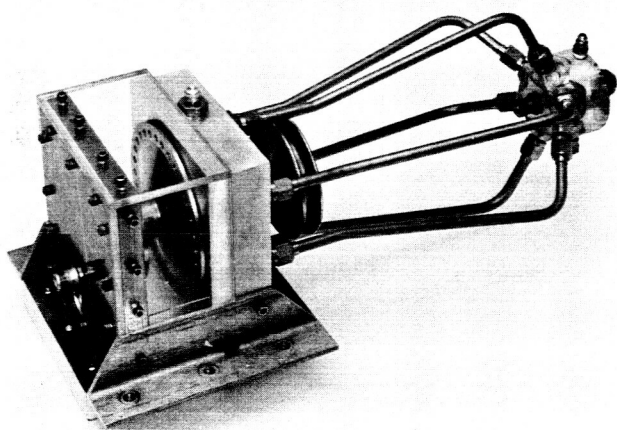


Figure 40. Siren, pressure perturbation generator

measure the steady-state and low-frequency (< 1 cps) flow disturbances as the EMFM electronics possess a drift rate which prohibits accurate measurement in this frequency régime.

Figure 42 represents the pressure drop characteristics of the bundle tubes with and without the flowmeters in the system. Even though the tubes were selected carefully as to dimensions, and formed accurately, there is a maximum $\pm 5\%$ overall variation in these characteristics.

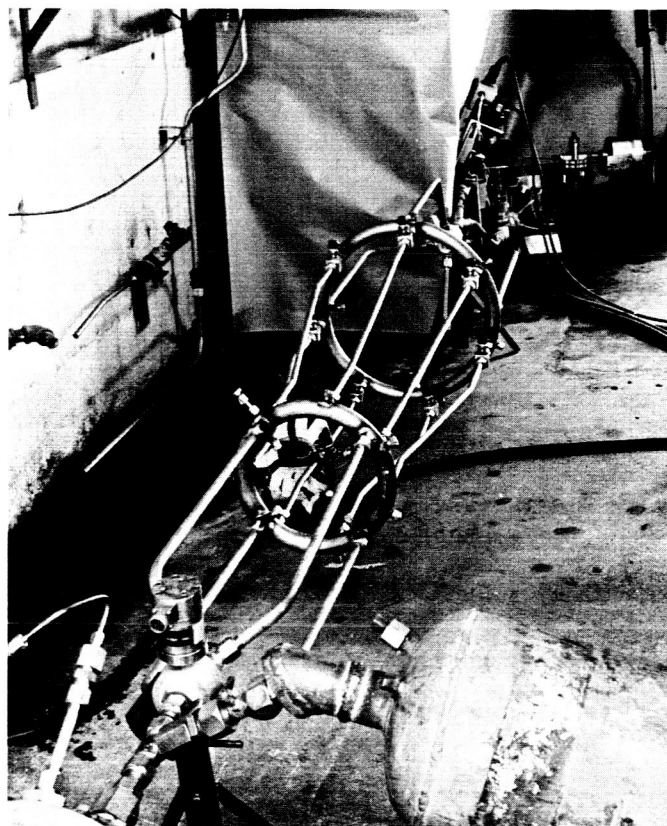


Figure 41. Model tube bundle test arrangement

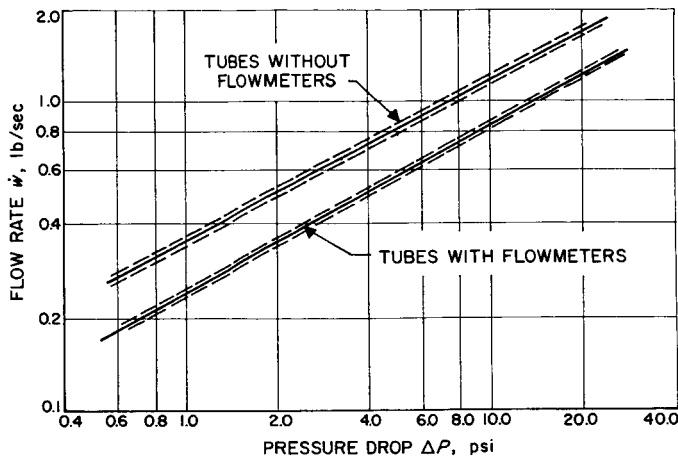


Figure 42. Bundle tubes, pressure drop characteristics

c. Test results. The *steady-state* flow distribution (i.e., mean flow level) of the bundle was determined for frequencies from 0 to 1400 cps and total flow rates from 0.4 to 6.0 lb/sec; i.e., the pressure drops across the bundle varied from 0.1 to 10.5 psi. The results from these tests are presented in Figure 43. For clarity, a polar graph was constructed, the radial scale representing the ratio of total flow rate of the bundle to the flow rate of the individual tubes. Since there are seven tubes, a value of seven represents the *ideal* mean value. Tube No. 1 registers a noticeable increase in flow, i.e., a lower value of the ratio of total to individual flow rate, over the average, due to its being directly in line with one of the inlet tubes. This is the only tube to be so oriented and therefore is unique in this respect. The points are clustered in a band whose width is commensurate with the accuracy of the flowmeters used in gathering this data, i.e., $\pm 0.5\%$. Good agreement was experienced between the summation of the seven indicated flow rates from the individual tubes and the indicated total flow rates as measured at the input to the bundle. These tests were run using a variable-speed fractional horsepower motor to drive the siren because the hydraulic power unit was in the process of construction at this time. The motor was underpowered so that 1400 cps was its maximum frequency capability. The data is grouped gratifyingly closely so that tests at higher frequencies were not deemed to be warranted, when the hydraulic motor-powered siren became available for testing.

The results of this testing indicate that the mean flow rate distribution through the bundle is quite insensitive to both pressure drop through the bundle (provided the tubes are matched relatively closely as to friction factor) and pressure amplitudes up to 150 psi peak-to-peak at frequencies of oscillation up to 1400 cps.

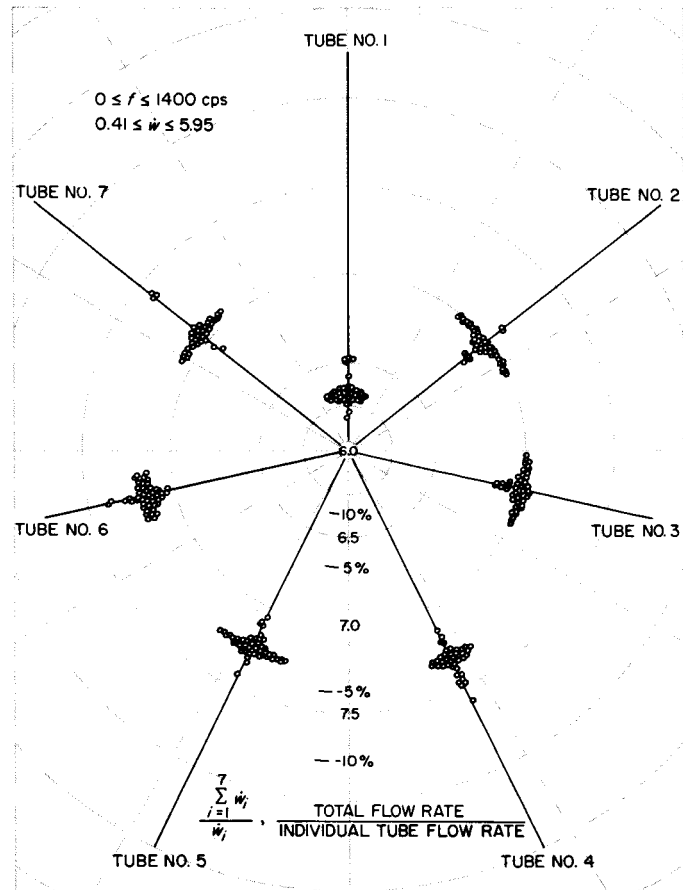


Figure 43. Tube bundle steady-state flow distribution

The analysis of the theoretical dynamic characteristics of the tube bundle indicates that Tubes 2 and 7 are dynamically similar, as are Tubes 3 and 6 and Tubes 4 and 5. It would, therefore, be reasonable to assume that the mean flow characteristics represented by Figure 43 would exhibit this symmetry between tube pairs. However, the dynamic analysis assumed identical tubes, and as there was in actuality a $\pm 5\%$ variation in the pressure drop characteristics between tubes in the model bundle, this caused the asymmetry shown. The spurious data points not falling within the main groupings have been studied. They do not appear to be caused by human or instrumentation error but rather by actual maldistribution occurring in the *steady-state* level over short periods of time.

A series of tests was conducted wherein the steady-state flow level was determined as a function of time under severe pressure disturbances (peak-to-peak amplitudes of 150 psi). A number of records indicated that at least one tube in the bundle could exhibit asymmetric damped vibration from $+31\%$ to -12% of the mean value. These oscillations, occurring at irregular times on the

order of 1 or 2 seconds, last approximately 50 milliseconds. The flow rate between the periods of oscillation was smooth.

These tests were quite severe insofar as pressure perturbation is concerned and are to be repeated at lower perturbation pressure levels commensurate with those occurring in the actual engine, i.e., 15 psi peak-to-peak. It is significant to note that a beat type of phenomena can be exhibited by the model configuration, which would tend to confirm at least qualitatively the postulate as to the failure mechanism.

The frequency spectrum was swept from 0 to 3500 cps in a cursory survey of resonance points, i.e., points where the flow perturbation is greatly amplified by a given outlet pressure perturbation. Definite resonance points were discovered at 350, 550, 850, 1200, and 1950 cps. These data are subject to an experimental error of $\pm 2\%$. As the system studied is lightly damped (low pressure drop) the resonance peaks are quite sharp, in some cases having half-power points (maximum amplitude of peak/ $\sqrt{2}$) separated by 5 cps or less. In order to improve the frequency regulation, a control system is being added to the siren power supply so as to maintain frequency within ± 0.5 cps of a desired value.

This will permit the transfer function, i.e., the ratio of flow perturbation at any given position of any one of the bundle tubes to the outlet pressure perturbation, to be determined and compared with theory.

d. Theoretical program. An analytical study was initiated in conjunction with the experimental program in

an attempt to describe the dynamic behavior of the model configuration.

The one-dimensional wave equation, as applied to a simple circular tube, was modified to take the tube wall's elasticity (but not inertia) and fluid friction into account. For ease of solution, this equation was linearized by assuming small perturbation approximations for the variables in question. The linearization process permitted transform methods to be applied, the Laplace transform being used to yield an equation for the dynamics of a simple tube in the frequency domain.

Working from the assumption of zero pressure perturbation at the inlet end of the tube bundle, known pressure perturbation at the outlet, identical physical properties of the bundle tubes, identical inlet and identical outlet tubes, but different manifold characteristics wherein manifold segments between tube junctures could be represented as straight one-dimensional sections of tubing, a matrix equation representing the transfer function of the tube bundle was developed. This matrix transfer function permits the calculation of the ratio of the flow perturbation in any one of the seven bundle tubes at any position between the manifolds to the outlet pressure perturbation level. It should be noted that any one calculation yields the transfer function for the seven flows through a plane perpendicular to the axis of the tube bundle so that the tube positions for each case considered are identical.

Figure 44 represents the transfer function for a position in the tube bundle along the median plane between

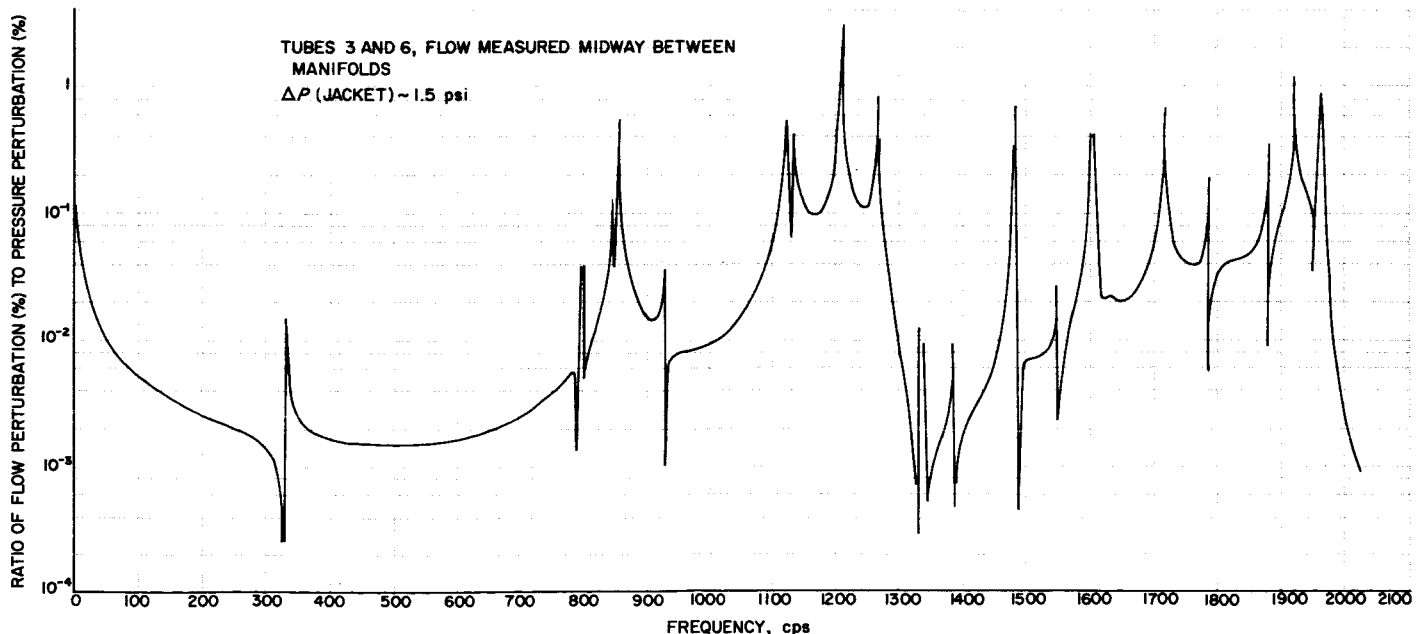


Figure 44. Tube bundle theoretical transfer function

manifolds for Tubes 3 and 6. This corresponds to the approximate position of the throat in the actual engine (expansion area ratio of 3.5). The structure of this transfer matrix indicated that there was symmetry in the dynamics of the flow. If the bundle tubes are numbered such that Tube 1 corresponds to the bundle tube which is directly in line with an entrance feed tube, then Tubes 2 and 7, 3 and 6, 4 and 5 were found to be dynamically identical. Figure 44 is quite representative of the dynamic characteristics of the other tubes in the bundle. A low total flow rate, and therefore low damping, is shown to result in quite *sharp* resonance peaks. Only the frequency range up to 2000 cps was investigated; however, it appears that there will be resonance peaks at higher frequencies having appreciable amplitudes.

The resonance peaks at 350, 850, 1200, and 1950 cps have been experimentally verified. There is a pressure perturbation present at the inlet to the model tube bundle, whereas theoretically, the pressure perturbation at this point is assumed to be negligible. This may account for the fact that a resonance point is experimentally observed at 550 cps while it is not predicted. The experimental arrangement is being modified so as to agree with the assumed boundary conditions imposed upon the theoretical study.

Work is in progress to calculate the time domain flow fluctuation due to a pressure perturbation spectrum typical of the 6K engine.

B. Thrust Chambers

1. Welded-Rib Thrust Chamber

A thrust chamber configuration designated as the welded-rib design, which is suitable for regenerative cooling applications, is being investigated to determine fabrication and operational feasibility as part of the thrust-chamber advanced development program. This type of thrust chamber consists of a continuous sheet metal liner which forms the inner walls of the combustion chamber and nozzle, longitudinal ribs which are brazed on the outer surface of the liner to form the side walls of coolant passages, and a layer of wrapped wire or ribbon to form the outer wall of the coolant passages. Additional details of the construction and fabrication of welded-rib type of thrust chambers may be found in RS 36-1, RS 1 through 6, and CBS 68.

Two completed 20:1 area ratio (serial numbers 30 and 38) and four completed 3.5:1 area ratio (serial num-

bers 29, 41, 44, and 45) thrust chambers are on hand awaiting engine test. All these chambers were fabricated with Solar Aircraft Company nickel braze alloys NX1 and IX1.

As reported in RS 36-1, Thrust Chamber 29, which was fabricated from Inconel, has had 80 seconds of water-cooled engine testing without any sign of failure. No additional tests have been made on this chamber.

Thrust Chamber 41 with the fifteen thermocouples installed along one coolant passage, as reported in RS 36-1, was completed, and two 15-second water-cooled engine tests were made. A photograph of this chamber is shown in Figure 45. The purpose of installing thermocouples along a coolant passage was to secure local heat flux distribution. Results of these tests are reported under heat transfer in Vol II of this summary. After the first test, it was discovered that an error had been made in the measured location of the thermocouples. A second test was made before removing the thermocouples and remeasuring thermocouple locations. During the second test, leaks developed around four thermocouple fittings at the locations where these fittings are brazed to the thrust chamber; consequently an uncertainty of correct coolant flow rate exists for this test. These leaks

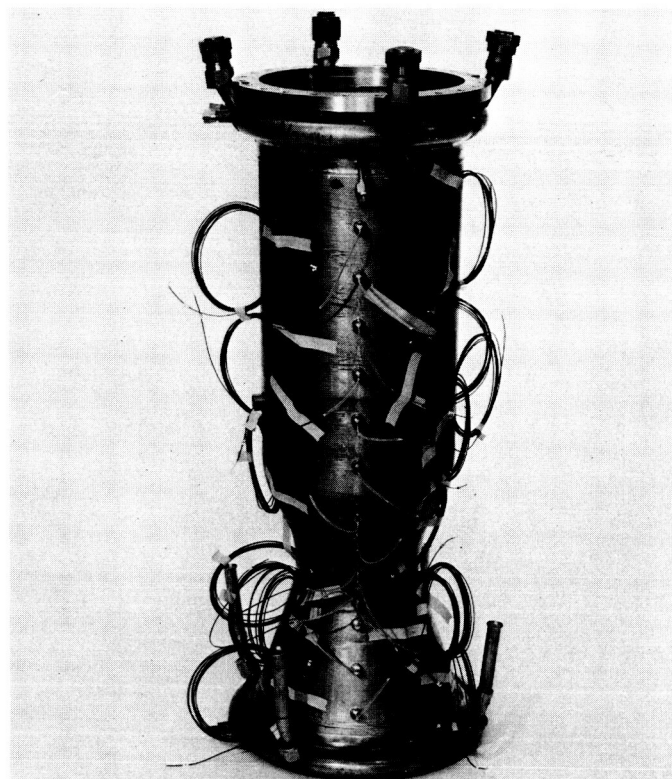


Figure 45. Completed 3.5:1 area ratio welded-rib Thrust Chamber 41

have been repaired with gold solder. More accurate thermocouple location and temperature measurements will be made before additional tests are conducted.

Thrust Chamber 44 was completed with the minimum number of braze cycles, which is three. This was the first chamber that was brazed in the minimum number of cycles. Thrust Chamber 45 required four braze cycles; the extra cycle was required to repair braze on the ribs. Both of these chambers have been pressure-tested at 400 psi in the coolant passages. Coolant passage pressure drop across the manifolds of Chamber 44 was 20.6 psi at a water flow rate of 10 lb/sec. This is a typical value of pressure drop at the given flow rate. Pressure drop has not yet been measured on Chamber 45.

Thrust Chamber 38, which has a contoured expansion section, is shown in Figure 46. A total of six braze cycles was required to complete this thrust chamber. Two of these were for repairs; one was to seal leaks between the ribs and the liner, and the other was to seal leaks between wire strands. Fortunately, there is apparently no adverse effect observed to result from four or five extra braze cycles. The combustion chamber and nozzle contraction section were wrapped with two layers of wire for added strength for the purpose of making a series of tests in

which a large safety factor is required. This chamber weighs 70.5 pounds and has a coolant passage pressure drop of 21.7 psi between manifolds for a water flow rate of 10 lb/sec. The coolant passages have been pressure-tested at 400 psi without any sign of deformation or failure. The difference in weight between the measured 70.5 pounds and the estimated 43.8 pounds reported in CBS 68 is represented by the second layer of wire, added stiffener rings to allow operation with separated flow, and the flange used for bolting on injectors. This thrust chamber has been instrumented with three sets of strain gages for stress measurements and five static pressure taps along the expansion section of the nozzle. The pressure measurements will establish the approximate location of the flow separation point in the nozzle should this occur during operation in the vacuum chamber-exhaust diffuser facility.

Thrust Chamber 30 has been through the braze furnace eight times. Four cycles were required as a minimum number for fabrication, and the other four were for repairs of wire and manifolds. It weighs 76.5 pounds and is heavier than Chamber 38 because it has two layers of wire over the entire length of the thrust chamber. Coolant passage pressure drop was 22.0 psi for a water flow rate of 10 lb/sec. It has only one nozzle static pressure tap located at the exit.

2. Uncooled Thrust Chambers

The role of the Laboratory in deep space exploration requires the development of small thrust devices to provide velocity increments of a few hundred feet per second for midcourse guidance maneuvers of spacecraft. Such thrust devices should be simple and reliable. This Laboratory has previously accomplished as an advanced-development project a demonstration of the feasibility of such units employing monopropellant-hydrazine as a propellant (RS 1, 2, and Ref 19), and is presently developing a monopropellant-hydrazine propulsion system for application in the series of *Agena* spacecraft. In future applications involving heavier spacecraft, it will be desirable to utilize systems producing higher specific impulses. It is believed that an uncooled, bipropellant $N_2O_4-N_2H_4$ propulsion system providing the increased performance could be developed with a minimum increase in complexity and might require no more development effort than required for a system utilizing a more complex and less flexible regeneratively cooled thrust chamber.

In view of the foregoing, a program has been initiated to investigate materials and design techniques for use in uncooled bipropellant thrust chambers. The goal of the program is to obtain sufficient experimental data to allow the development of flight-weight uncooled thrust cham-

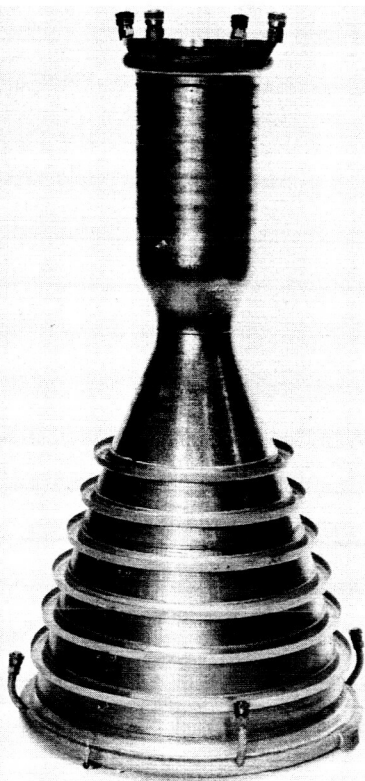


Figure 46. Completed 20:1 area ratio contour welded-rib Thrust Chamber 38

bers in the range of 50- to 500-pound thrust. In addition, it is expected that generalized results will be obtained which will also be applicable to larger thrust units, such as the 6K propulsion system presently under development by the Laboratory.

Materials are being tested in research motors at the 100-pound-thrust level, either as complete thrust chambers or as nozzles attached to a water-cooled chamber. Propellants are N_2O_4 - N_2H_4 at mixture ratios of 0.3 to 1.0. Materials presently under consideration are:

- (a) Ablative (refrasil-phenolic).
- (b) Refractory non-metals (Pyrographite).
- (c) Refractory metals (molybdenum and tungsten).
- (d) Combinations of these.

Testing of ablative thrust chambers has begun. To date, one test has been accomplished at a mixture ratio of 1.0 and initial chamber pressure of 142 psia. Duration was 247 seconds. The chamber pressure remained constant for the first 120 seconds of operation and then decreased linearly to 136 psia at shutdown. Performance

of the ablative material was considered satisfactory, and further testing is planned. The sectioned chamber is shown in Figure 47. Nozzles of Pyrographite, molybdenum, and tungsten are being procured, and additional materials will be investigated if they appear suitable.

C. Heat Transfer and Fluid Mechanics

1. Heat Transfer in Rocket Motors

The magnitude and distribution of local heat flux in combustion chambers and nozzles of rocket engines must be determined accurately in order to facilitate the development of rocket engines for flight use. Measurements of heat transfer from combustion gases to the inner walls of rocket engines have been continued in order to gain a better understanding of this process.

In RS 36-1, Vol I, experimental results of an 8:1 contraction area ratio 1000-pound-thrust nozzle were reported, and comparisons were made with analytical predictions. Those test results and the simplified equation of Reference 20 used to predict the heat transfer have been included on Figure 48. Except for two data points that were obtained near 300-psia chamber pressure and indicated excessively high heat fluxes, the maximum nozzle heat flux was found to vary linearly with chamber pressure. It was reported then that the two data points at excessively high heat fluxes were accompanied by the burned and loosened orifices and the burned injector. Since that report two additional tests using an L^* of 62.8 inches were made near 300-psia chamber pressure with the same nozzle and propellant combination as previously reported to determine if these points at the comparatively high chamber pressure were high because of abnormal conditions. The average c^* was approximately 5350 ft/sec or 0.5% lower than the average value obtained during the previous tests. Furthermore, this time there were no difficulties experienced with the injector. The results of the recent tests indicate that the previous results were high, probably due to combustion effects; it is evident that there is not a severe chamber pressure effect at the higher pressures.

The results of the 62.8-inch L^* tests now show that the analytical prediction of maximum nozzle heat flux versus chamber pressure is a suitable upper limit for the described rocket nozzle configuration operating in the region of the specified conditions.

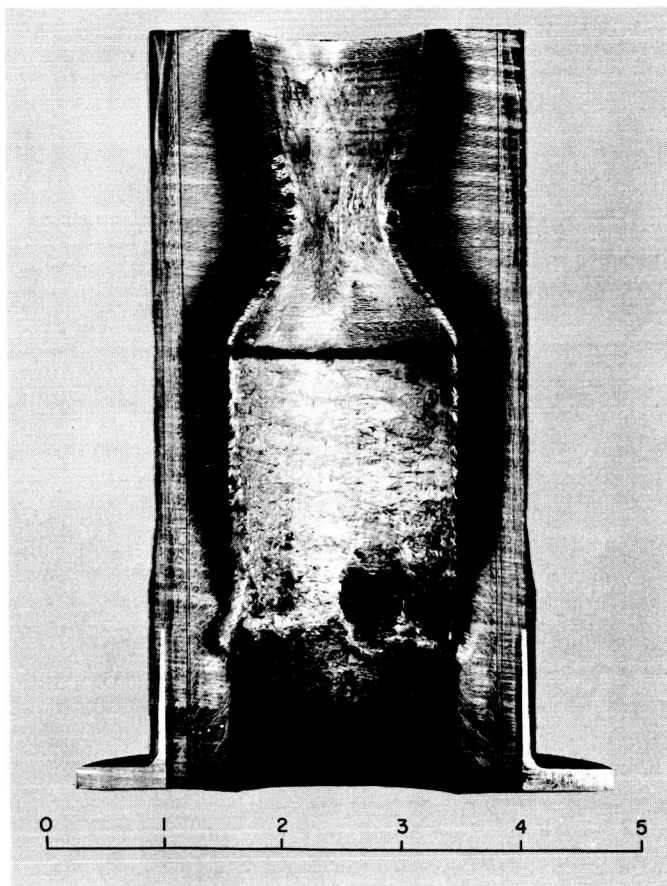


Figure 47. Sectional view of ablative thrust chamber after test

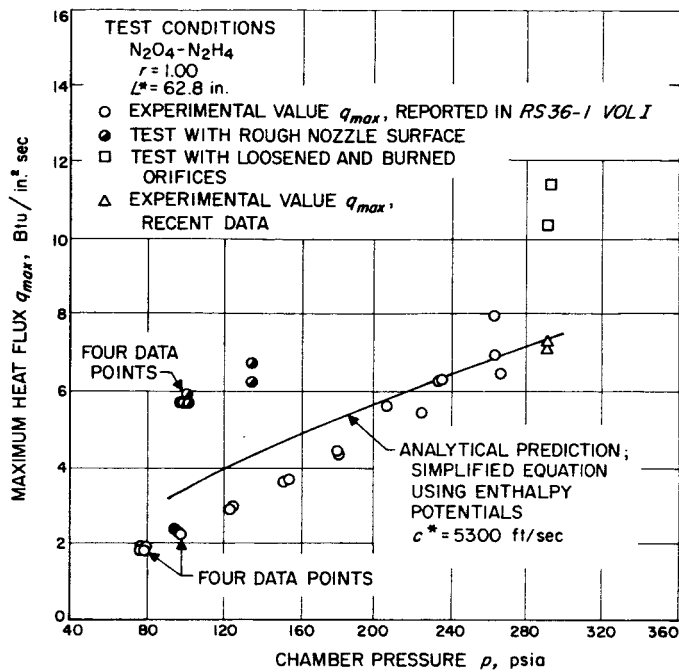


Figure 48. Chamber pressure vs maximum heat flux

2. Diffusers

The necessity of testing at ground level the rocket engines that are designed for high-altitude or space-operation conditions was briefly discussed in RS 36-1. Various means for accomplishing ground-level testing were mentioned. In particular, the rocket engine exhaust diffuser was considered in detail with respect to its feasibility, operational capability, and adaptability to rocket engine testing. Two general types of exhaust diffusers were described: (1) the constant-diameter-duct type and (2) the second-throat type. The history and progress of an experimental exhaust-diffuser program using 0.1-scale models was briefly sketched, and some of the more pertinent data were given. Since the writing of RS 36-1, the model experimental program has been terminated. The most recent data and some preliminary data on the performance of the full-scale diffuser are presented in this report. All results given in this report pertain to bipropellant operation using the combustion products of hydrazine and nitrogen tetroxide.

Configurations 2 and 3, the two second-throat type diffusers shown in Figure 49 and also shown in RS 36-1,

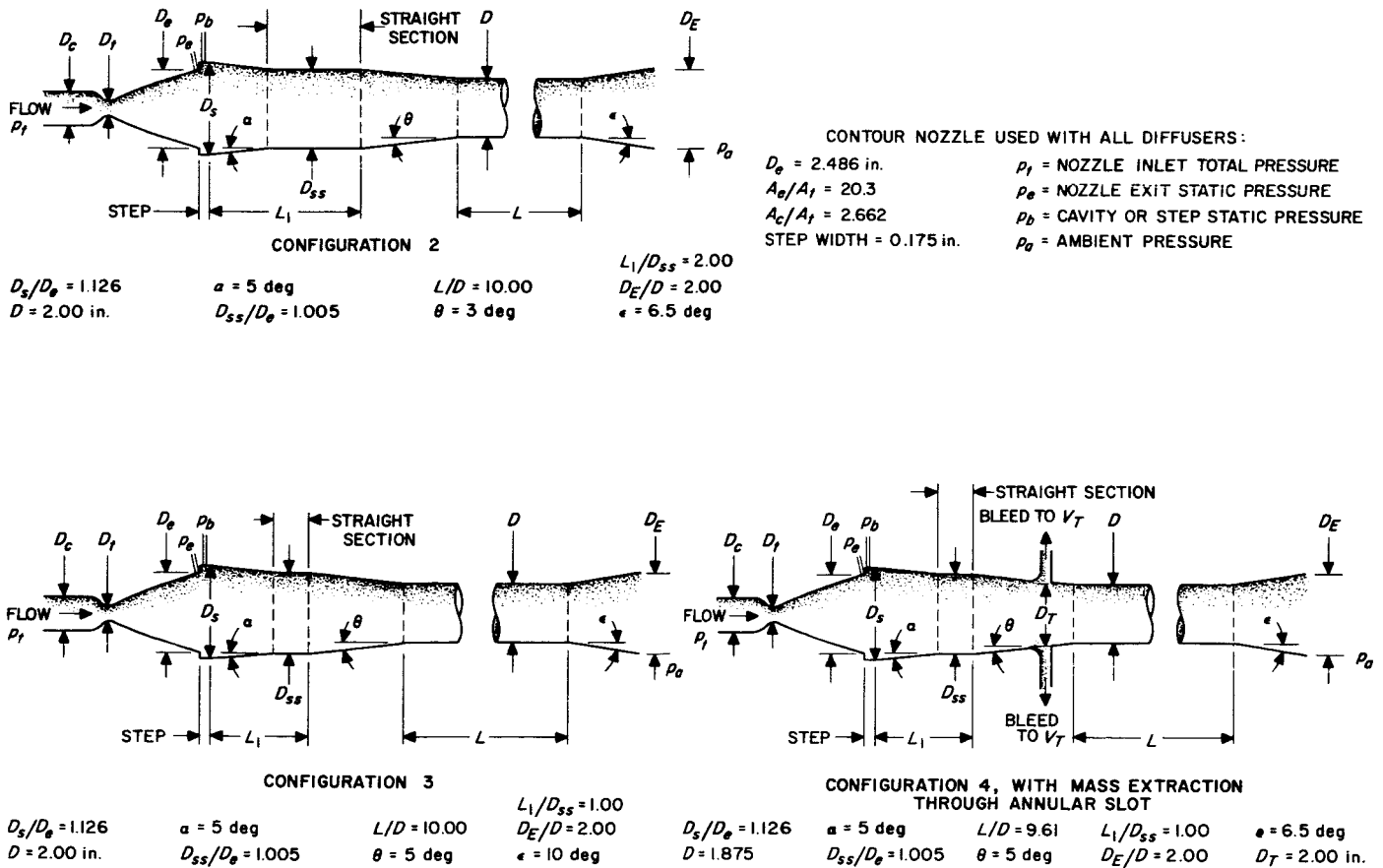


Figure 49. Experimental second-throat type diffuser Configurations 2, 3, and 4

Figure 143, were retested using a smaller cavity diameter which more closely simulated the full-scale exhaust diffuser. The earlier tests were made using a ratio D_s/D_r of 1.035 used on the first full-scale exhaust diffuser. The starting and operating total pressure required for the two configurations, each with two different cavity diameters, are summarized in Table 14. A reduction in cavity size produced no marked changes in diffuser performance; the minimum starting pressure was the same, but the minimum operating pressure was slightly reduced.

Additional experiments were made using mass extraction of primary gas into a vacuum tank on start, as previously described in RS 36-1. This procedure permits starting with a smaller second throat at a lower chamber pressure. Configurations 2 and 3 had a diffuser contraction ratio (nozzle exit area divided by second-throat area) of 1.547; and Configuration 4 (Fig 49), using the mass extraction technique, had a contraction ratio of 1.760.

Table 14. Effect of cavity diameter on performance of two second-throat type of diffusers^a

Parameter	Configuration 2		Configuration 3	
	$D_s/D_r = 1.126$	$D_s/D_r = 1.065$	$D_s/D_r = 1.126$	$D_s/D_r = 1.065$
Minimum starting pressure p_t , psia	220	220	162	162
Minimum operating pressure p_t , psia	167	154	162	157

^a Gas constituents are the combustion products of N_2O_4 and N_2H_4 , $\bar{\gamma} \sim 1.22$.

The minimum starting total pressure of Configuration 4 was the same as that for Configuration 3, or 162 psia, but the minimum operating total pressure was reduced to a value of 133 psia as compared to a value of 162 psia for Configuration 3. A second suction slot was designed for use with an even larger contraction ratio of 2.02. This suction slot differed from the first slot in two respects: (1) it had a larger annular area and (2) was inclined to the direction of flow 40 degrees instead of 90 degrees. Experiments showed that the diffuser could not be started using the second suction slot and a diffuser contraction ratio of 2.02. Although the reason for failure to start is not completely clear, there is a high probability that choked flow conditions existed in the manifolding system between slot and vacuum tank. Such conditions would have prevented primary gas removal at the required rate during the starting sequence.

Diffuser Configuration 5 is shown in Figure 50. This configuration has no abrupt cavity following the nozzle exit; and it features, what is hoped to be, a gradual turn-

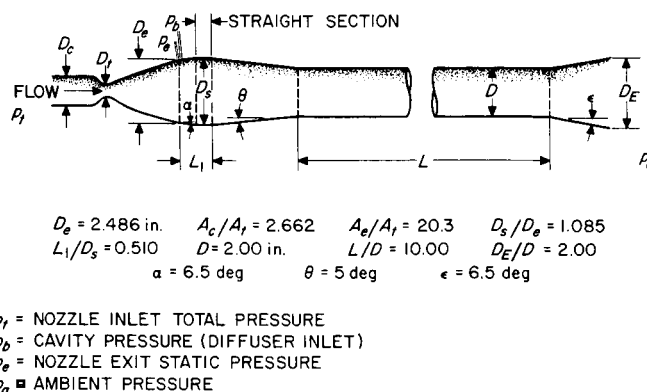


Figure 50. Configuration 5, second-throat type diffuser

ing of the nozzle exhaust flow toward an axial direction before flow contraction occurs in the diffuser. In the case of Configurations 2, 3, and 4, a cavity pressure p_b much lower than the nozzle exit pressure p_e was measured. The pressure denoted as p_b for Configuration 5 in Figure 50 was found to be significantly higher than p_e , although measured values of p_e for Configuration 5 were comparable to those measured for Configurations 2, 3, and 4. This result, which indicates an oblique shock compression at the nozzle exit plane rather than expansion as in the previous cases, is to be expected because of an abrupt decrease in the wall angle. The starting and operating total pressures obtained with Configuration 5 compare favorably with Configuration 3, which has been considered to be the optimum configuration. Table 15 summarizes these results. A photograph of an external view of Configuration 5 is shown in Figure 51 and shows the method of spray cooling which has been successfully employed on previous configurations. Note that the diffuser is bolted directly to the nozzle cooling jacket shown to the left-center of the picture. Static pressure taps are located on top of the diffuser and are connected by copper tubing to a manometer board.

Experiments were also made with canted diffusers to simulate the effect of nozzle gimbaling and its possible effect on diffuser performance. Tests were made using Configuration 3 adapted so that wedges could be inserted

Table 15. Comparison of performance of diffuser Configurations 3 and 5^a

Parameter	Configuration 3	Configuration 5
Minimum starting pressure p_t , psia	162	162
Minimum operating pressure p_t , psia	162	150

^a Gas constituents are the combustion products of N_2O_4 and N_2H_4 , $\bar{\gamma} \sim 1.22$.

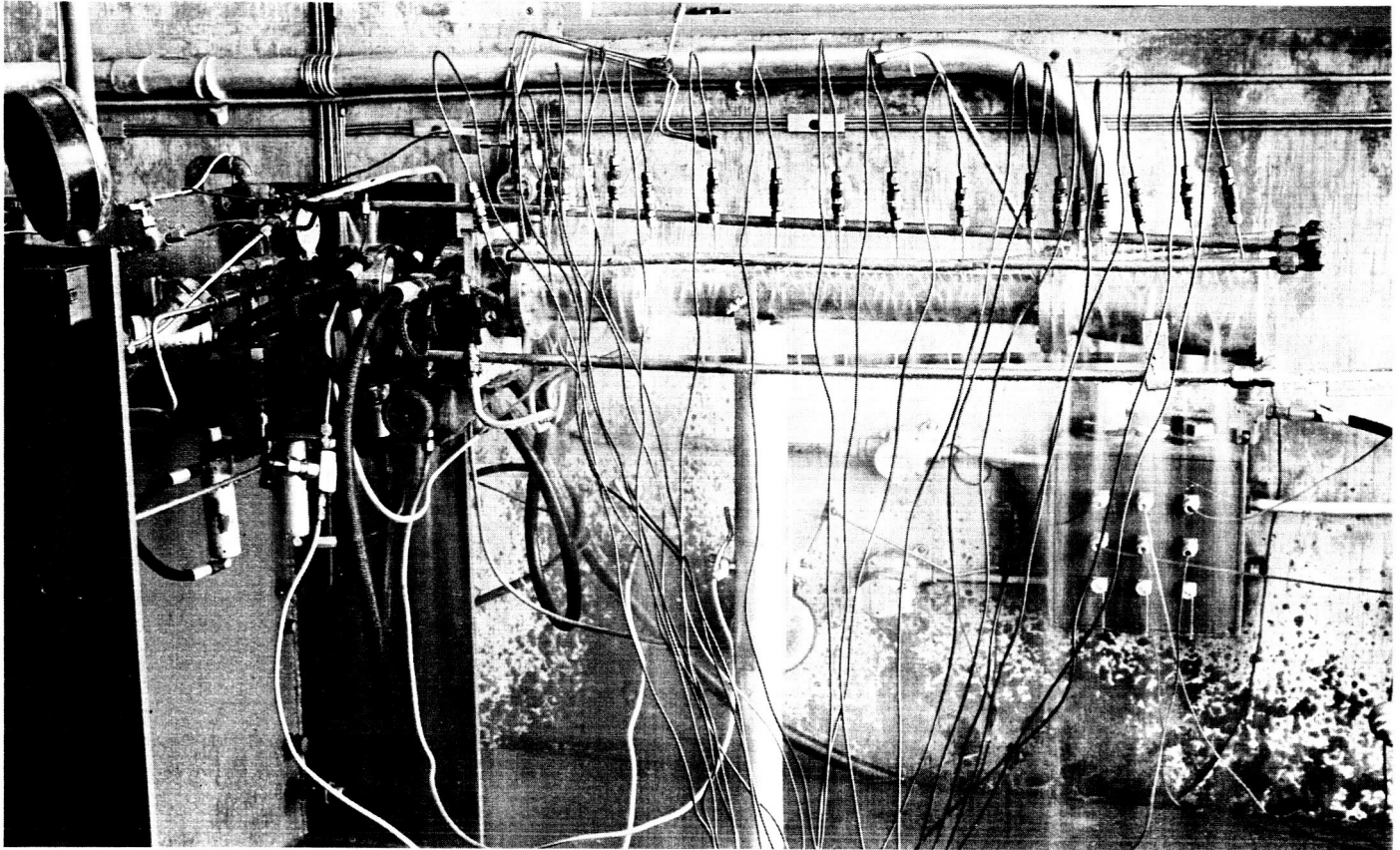


Figure 51. External view of Configuration 5 showing spray-type cooling

between the nozzle exit and the diffuser inlet. Such an arrangement is shown in Figure 52. Wedge angles β of

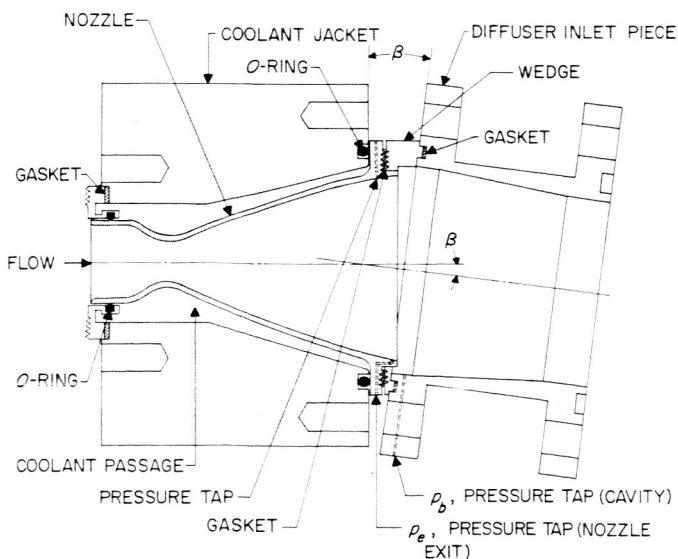


Figure 52. Simulation of nozzle gimbaling by insertion of a wedge between nozzle and diffuser inlet piece

3, 5, and 7 degrees were tested. The effect of wedge angle on diffuser performance is shown in Figure 53. As expected, the minimum starting total pressure increases with wedge angle. Strangely, the minimum operating characteristics are improved for moderate wedge angles. The reason for this phenomenon is not apparent. Aside

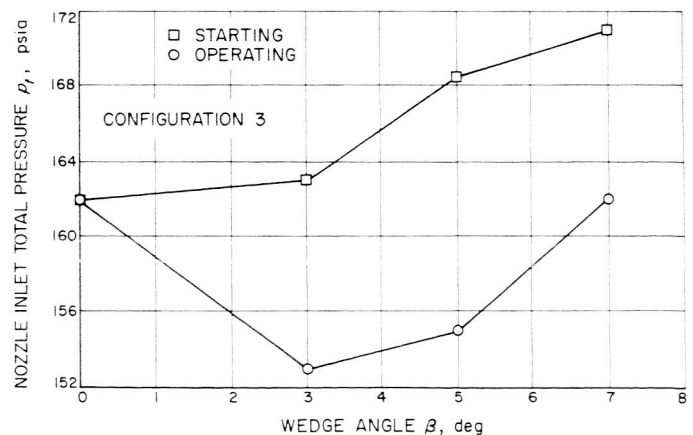


Figure 53. Effect of angular misalignment between diffuser and nozzle axes on diffuser performance

from diffuser performance, another feature of canted diffusers is noteworthy. During the course of this experiment, considerable care had to be exercised to prevent burnouts from occurring in the second throat on the side of the wall inclined toward the direction of the axis of the nozzle. The opposite side of the second-throat wall, inclined away from the direction of the nozzle axis, remained unaffected. Water coolant sprays were carefully directed to impinge in critical locations. Even so, burnouts were narrowly averted in two instances. The position of the hot spots generally moved upstream with increasing wedge angle.

The full-scale diffuser has been operated successfully four times—twice with engines having an 8:1 nozzle area ratio and twice with engines having a 20:1 nozzle area ratio. A schematic drawing of the vacuum chamber and exhaust diffuser facility is shown in Figure 54. This arrangement is of the type shown in RS 36-1, Figure 139b. The diffuser is not mechanically attached to the thrust chamber. Several static pressure taps are located in the vacuum-chamber wall. The flange of the vacuum chamber is fitted with a cooling ring to prevent it from being damaged by the exhaust gases of the engine. Another static pressure tap is located just downstream of this ring. The diffuser itself is fabricated in five short lengths,

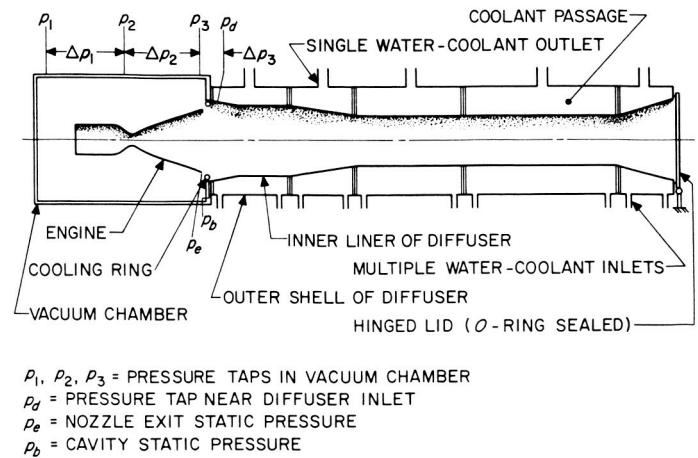


Figure 54. Schematic arrangement of diffuser and vacuum chamber

all of which are double-walled sections. The annular spaces serve as coolant water passages; cooling is accomplished by vortex motion of the water. Since the engine exhaust gases cause an appreciable growth in the length of the diffuser (approx 0.7 inch), an expansion joint has been installed in the outer shell midway between inlet and exit. A photograph of the exit end of the diffuser is shown in Figure 55. The rather complex array of pipes



Figure 55. View of exit end of present full-scale diffuser

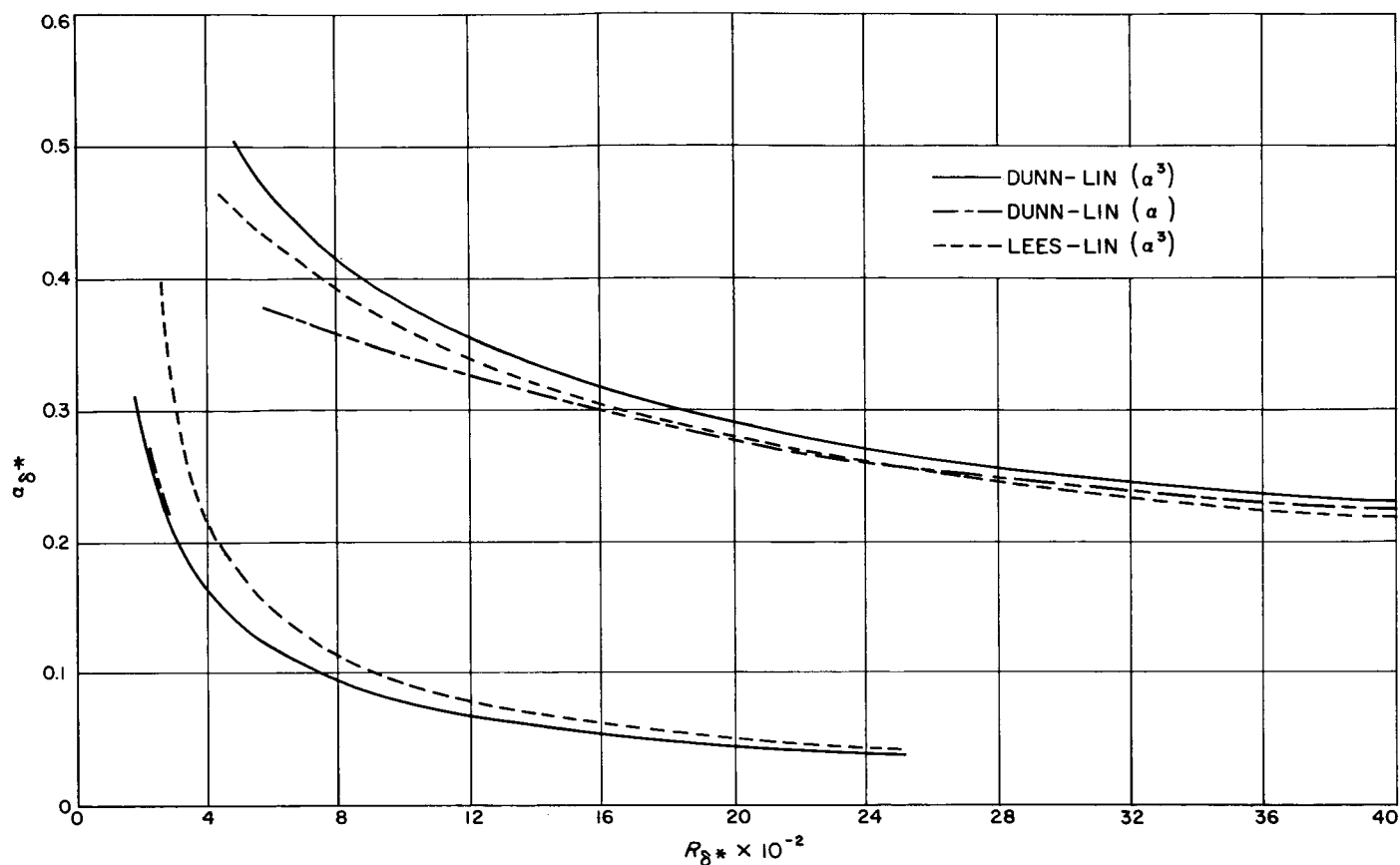
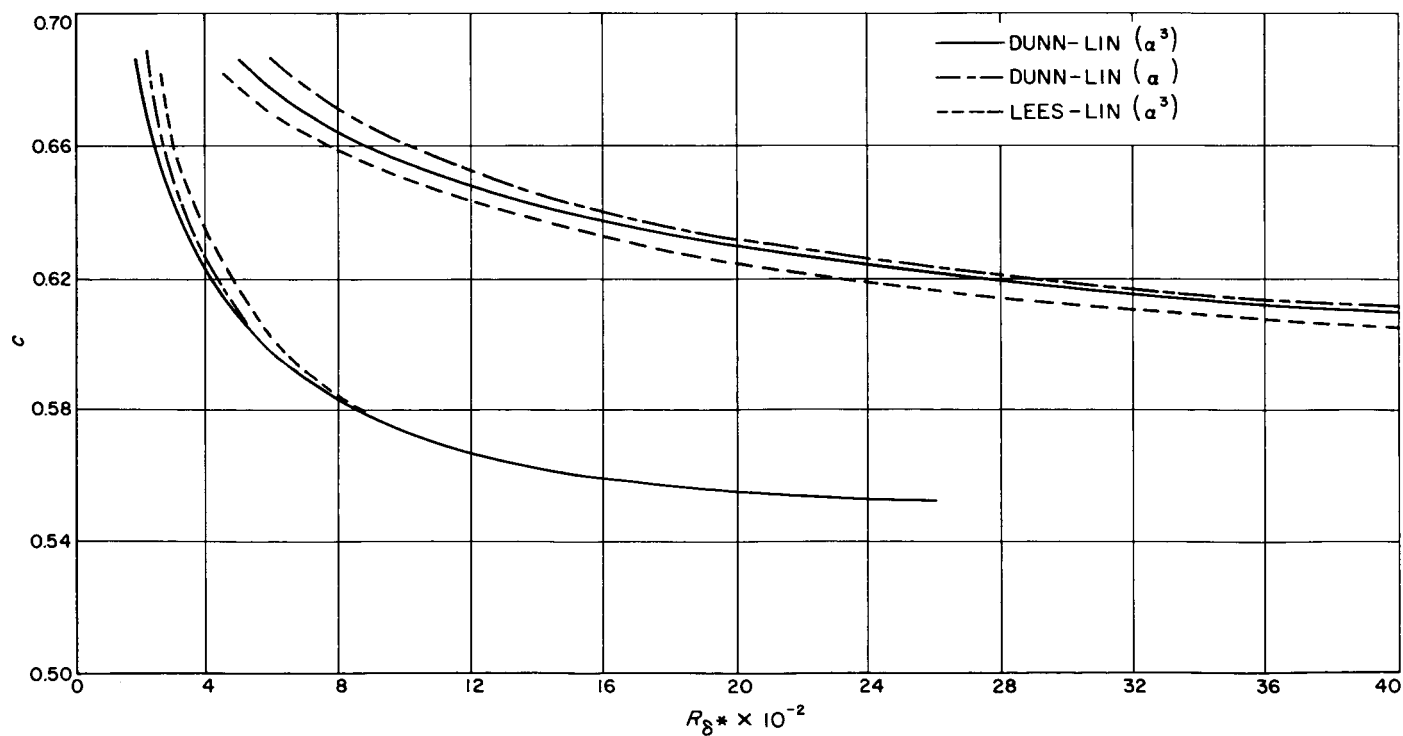
and hoses is used to provide more than adequate cooling of the diffuser. Not shown in the photograph is the hinged lid at the diffuser exit. This lid was installed at a later date to allow vacuum starts of the engine. It is blown open by the momentum of the engine exhaust gases during start. There is some indication, based on actual engine tests, that the vacuum start lessens the large pressure and thrust overshoot that has been experienced by the engine on start. When the diffuser is started without the lid the column of air in the diffuser must be removed very quickly by the engine exhaust gases. The resulting shock type of impact between the gases may possibly account for the large pressure overshoot in the vacuum chamber.

Diffuser performance results are given in Table 16 for both 8:1 and 20:1 area ratio nozzles. These results are not to be taken as representative because they are based on limited data. The starting and operating total pressure values listed are not necessarily minimum values. However, in the case of the 20:1 area ratio nozzle, the listed starting pressure is thought to be close to the minimum because in this case the diffuser took approximately 5 seconds to start. Note that the measured values of the static pressure in the vacuum chamber are quite similar to the measured value of the nozzle exit pressure. Just as in the case of the model tests, p_e is greater than p_b , although the geometrical similarity in the two cases is not identical. A comparison to the performance results of the equivalent model diffuser can be made for the 20:1 area ratio nozzle by consulting Table 14. The appropriate numbers to be

Table 16. Preliminary performance results of the full-scale diffuser^a

Parameter	8:1 area ratio nozzle	20:1 area ratio nozzle
Starting pressure p_t , psia	251	212
Operating pressure p_t , psia	172	172
Nozzle exit static pressure p_e , psia	Not measured	1.03
Vacuum chamber wall pressure, psia	$p_z = 1.77$	$p_z = 1.18$
Cavity static pressure p_b , psia	0.76	0.73
Total run duration, sec	30	25
^a Diffuser design is based on model Configuration 2; gas constituents are the combustion products of N_2O_4 and N_2H_4 , $\gamma \sim 1.22$, $T_c \sim 5000^\circ R$.		

used in Table 14 are in the right-hand column listed under Configuration 2, i.e., for $D_s/D_e = 1.065$. It will be seen that the full-scale diffuser has been started at a nozzle inlet total pressure less than that required by the model diffuser. Conversely, the minimum operating total pressure of the model diffuser has not yet been achieved for the full-scale diffuser. A small, positive pressure gradient, measured from the nozzle exit toward the injector end of the chamber, was seen to occur in the vacuum chamber. This pressure gradient varied somewhat from test to test.

Figure 56. Neutral-stability curves of wave number at $M_1 = 2.2$ Figure 57. Neutral-stability curves of phase velocity at $M_1 = 2.2$

VII. GAS DYNAMICS RESEARCH

A. Stability of Compressible Laminar Boundary Layer

As part of the continuing investigation of the stability of the compressible laminar boundary layer on an insulated flat plate, some additional calculations of the neutral-stability curve at a Mach number of 2.2 have been carried out. The previous computations, which are included in Reference 21, were performed using the simplified eigenvalue equation of the Lees-Lin theory (Ref 22) with the improved viscous solutions of the Dunn-Lin theory (Ref 23). At that time, the correct form of the Dunn-Lin eigenvalue equation was not known. Recently, however, Reshotko (Ref 24) has derived the correct eigenvalue solution, thus permitting the computation of a Dunn-Lin neutral-stability curve. Such a curve differs from the Lees-Lin neutral-stability curve in that it includes the effect of the temperature fluctuations.

In Figure 56 are shown three neutral-stability curves at $M_1 = 2.2$. The dimensionless wave number based on the boundary-layer displacement thickness, δ^* , is plotted against the free-stream Reynolds number, also based on δ^* . The upper and lower branches of the neutral-stability curves, which must join at some $R_{\delta^*} > 0$, are shown unjoined because of limitations in the numerical methods

used. The unstable region lies between the upper and lower branches of the neutral curve. Outside of this region the boundary layer is stable. The solid curve in Figure 56 is the result of the Dunn-Lin theory with the Reshotko eigenvalue equation. The dash-dot curve is from the same eigenvalue equation, but with a simplified form of the inviscid solutions. The remaining curve is the one previously computed from the Lees-Lin eigenvalue equation and the Dunn-Lin viscous solutions, and neglects the effect of the temperature fluctuations. The corresponding neutral-stability curves in terms of the dimensionless phase velocity c are shown in Figure 57. A complete discussion of the numerical computations and the underlying theory is given in Reference 25.

B. New Method to Measure Sphere Drag in Rarefied Supersonic Gas Flows

There is great practical need for drag data on simple bodies moving at supersonic speeds in a rarefied atmosphere. Even for the classical sphere, there are few drag results to be found at Reynolds numbers below about

2000, and the data available show such scatter and are generally in doubt. In fact, the greatest single source of error of satellite re-entry predictions is the lack of accurate knowledge of the drag. A simple method was devised to measure drag of spheres in the low-density gas dynamics facility of this Laboratory, and preliminary results are given here.

1. Experimental Method

Drag data were obtained in a uniformly diverging supersonic nozzle operated continuously with dry air in a Mach number range of 3.9 to 4.4, depending on supply pressure, and at stagnation temperatures around 300°K and test section pressures from about 40 to 100 microns. The sphere models were at equilibrium wall temperature. The method used to determine the drag is shown schematically in Figure 58. The sphere model is a steel or bronze ball bearing supported by 0.5-mil tungsten wire from above at a well-defined nozzle centerline station by sighting with a cathetometer. During tunnel operation, the model is blown backwards until an equilibrium deflection angle δ given by weight and drag is reached. The support point is then moved forward by a traversing mechanism until the sphere has reached its initial posi-

tion. It was found that no stationary conditions could be achieved without damping the sphere motion. A second sphere, called a damper, was attached to the sphere model and was immersed in an oil bath. In the idealized situation depicted in Figure 58, the drag may be determined from the measurement of support wire length L , deflection Δx , and weight of the assembly W . We have for the drag D

$$D = W \sin \delta \quad (1)$$

and we find the deflection angle from

$$\sin \delta = \frac{\Delta x}{L} \quad (2)$$

The value of W in Equation (1) is given by

$$W = W_{\text{model}} + W_{\text{damper}} - S_{DC} V_{\text{damper}} \quad (3)$$

where S_{DC} is the specific gravity of the DC 200 oil in the bath, and V_{damper} is the volume of the damper sphere. The last term in Equation (3) accounts for the buoyancy. In a real situation, as shown in the photograph of Figure 59, a hole is drilled straight through the model for the support wire; and during an experiment, the damper weight is found not to cut through the model center and the same is true for L . Owing to these difficulties, errors were found when $W_{\text{damper}} \gg W_{\text{model}}$, and only those data are accepted that show identical drag values of a given model at given Reynolds and Mach numbers for different damper sizes. Among other considerations are the following: (a) The support wires are so small that free molecular flow conditions apply, and in the range of results shown here the wire drag was estimated to be negligible. (b) The surface tension pull of the oil on the wire emerging from the oil bath is negligible. (c) The Mach number gradient in the nozzle of about 0.1/inch at the model location had no noticeable effects on the drag as found by obtaining identical results for different model sizes. (d) The limiting upper model diameter in relation to the undisturbed free stream was found empirically by accepting only those results that overlapped with drag values of smaller spheres. (e) Experiments on drag of a given model repeated after many hours of continuous operation indicated that the data taken were at equilibrium temperature conditions.

2. Preliminary Results

From the known nozzle calibration, the dynamic pressure q and Reynolds number based on sphere diameter could be determined. The drag coefficient C_D is defined by

$$C_D = \frac{D}{qA} \quad (4)$$

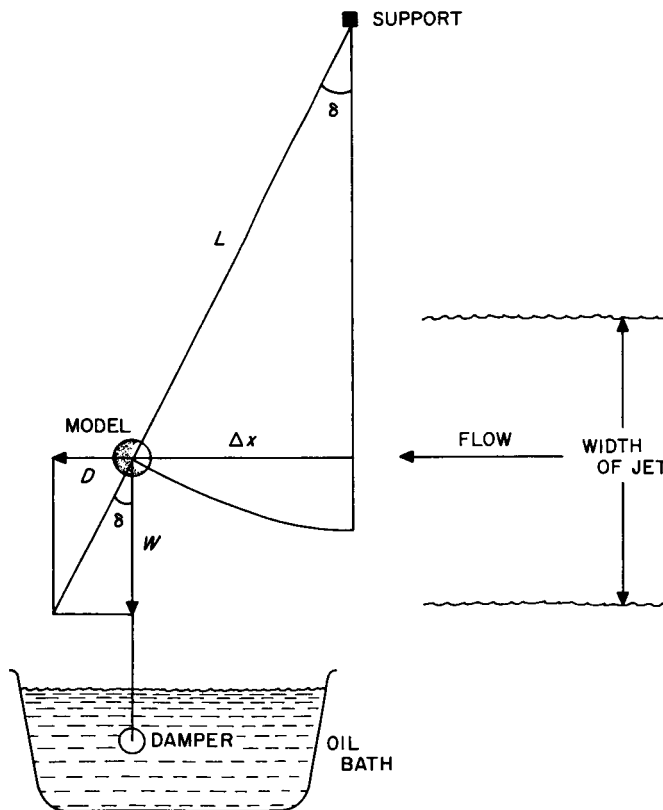


Figure 58. Flow and suspension geometry

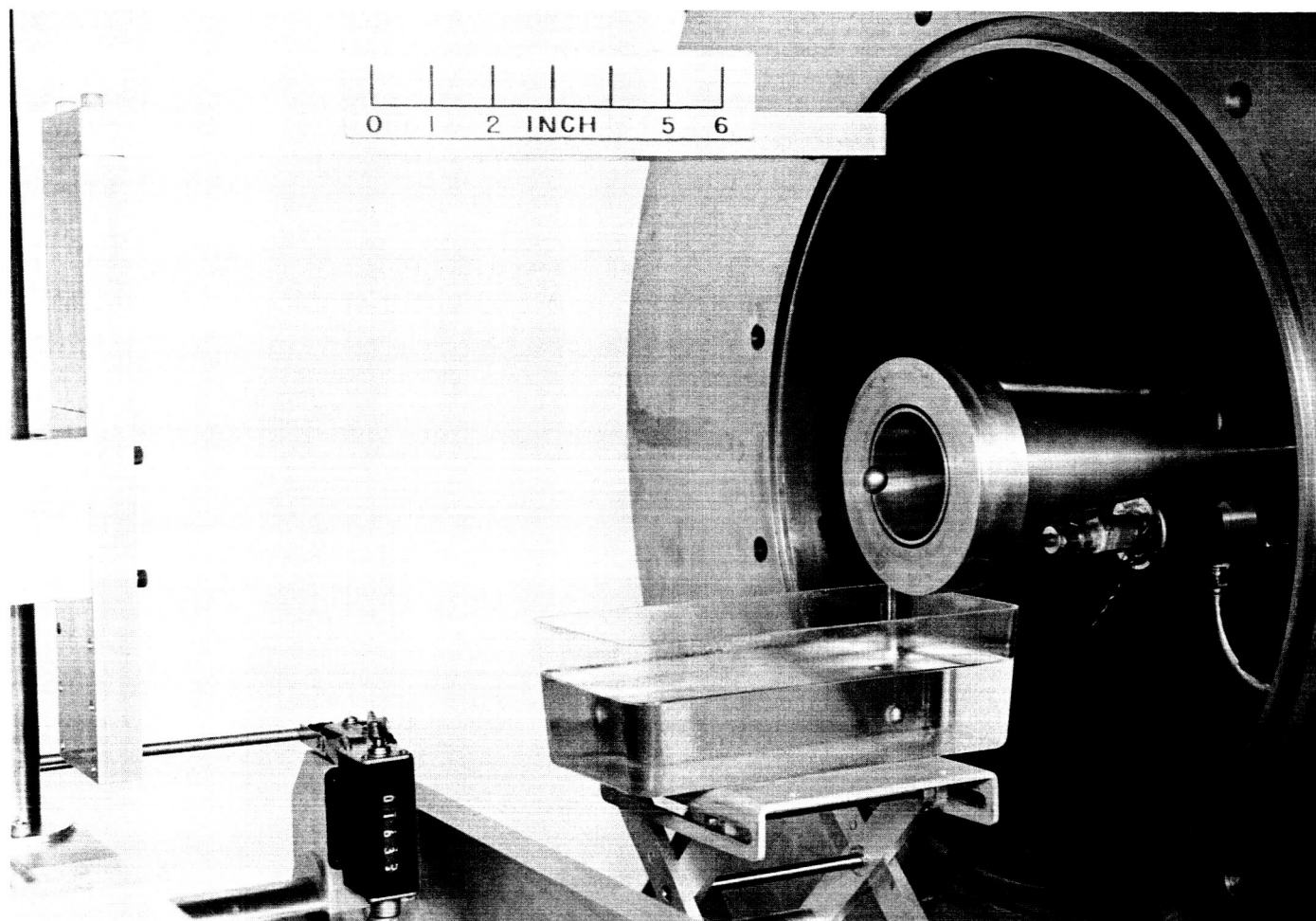


Figure 59. The 0.5-inch-diameter sphere in Mach 4 jet showing viscous damping mechanism

where A is the cross-sectional area of the sphere. Since no noticeable Mach number effect was observed, the final results may be given as $C_D = C_D(Re)$ in Figure 60. In this figure, overlapping sphere drag coefficients are shown for sphere diameters of $\frac{1}{2}$, $\frac{3}{8}$, $\frac{1}{4}$, $\frac{3}{16}$, and $\frac{5}{32}$ inch. The results show remarkably little scatter, and the expected C_D -rise with decreasing Reynolds numbers is clearly seen. Further work is currently being carried out

to verify the results shown with many more experiments and to study sphere drag with surface temperatures above and below the equilibrium value. Finally it will be attempted to experiment at smaller Reynolds numbers than shown.

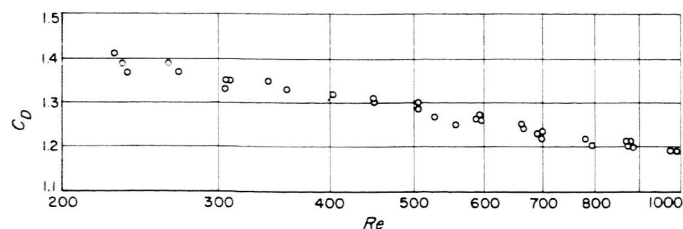


Figure 60. Drag coefficient of spheres at low Reynolds numbers

C. Stability of One-Dimensional Flow of a Real Continuous Fluid

1. Flow of a Viscous, Compressible, Heat Conducting and Chemically Reacting Gas

The purpose of the present investigation is to give a concise yet realistic theory of the one-dimensional flow

of a real continuous fluid. The mathematical implications inherent in the equations governing such flows in particular with regard to its stability are explored in considerable generality. As a concession to mathematical expediency, it was assumed that the Prandtl number is 0.75 and that the Lewis number is unity. The ensuing simplicity of the equations of motion is a reasonable price to pay for a certain lack of generality. The momentum and energy equations are substantially simplified by the introduction of the stream function as a streamwise coordinate. This coordinate transformation will be recognized as the analog to the von Mises transformation, well known in the theory of the boundary layer. The momentum equation (and for that matter the energy and

conservation of species equations) is nonlinear in the space-time plane by virtue of its convective acceleration term and becomes *linear* once the transformation to the stream-function-time plane is carried out. Moreover, it assumes the well-known form of the diffusion equation in a homogeneous medium. The pressure gradient appears as a *forcing function* on the right-hand side. The whole classical apparatus of dealing with this type of equation can now be brought to bear on this investigation. Using the method of Green's function permits one to obtain explicit solutions for velocity and pressure perturbations of a very general nature. It is demonstrated that the flow will be stable within the framework of this (linear) stability analysis (Ref 26).

VIII. HYPERSONIC WIND TUNNEL

Installation of the schlieren optical system for the hypersonic wind tunnel was completed in February. This system (Fig 61), which was designed and built to JPL specifications by the Boller and Chivens Company of South Pasadena, has several novel features that distinguish it from the usual wind tunnel schlieren system. Possibly the most important of these is the totally enclosed and evacuated light path. Elimination of the obscuring action of atmospheric convection currents has produced an increase in sensitivity to density gradients in the flow pattern. Evacuation is accomplished by means of a tube from the enclosure to an opening in the tunnel wall downstream of the test section. The enclosure pressure is thereby similar to that of the test section. The optical system is isolated from enclosure stresses by stainless

steel bellows of many convolutions. These prevent transmission of enclosure distortions resulting from evacuation.

The evacuated light path requires that the system variables be actuated by remote controls. The available range of movements are as follows:

- (a) ± 1 -inch axial movement of the slit and cut-off knife edge from the focal points of their respective mirrors.
- (b) Synchronous 180-degree rotation of the light source, slit and cut-off knife edge.
- (c) ± 0.5 -degree differential rotational control of the cut-off knife edge.
- (d) ± 0.060 -inch translation of the cut-off knife edge, and incremental movement for selection of upper or lower edge.
- (e) 0 to 0.020-inch slit width.
- (f) 0 to 0.75-inch slit length.

The control-room side of the schlieren system is shown in Figure 61, with some of the main features identified.

A problem, peculiar to hypersonic operation, has arisen in regard to temperature gradients that occur in the test section windows. Due to the water cooling in the frame, the edges of the quartz are about 75°F, but the center of the windows may approach 400°F. The resulting lenticular expansion produces an axial shift in the second spherical mirror focus point and, therefore, in the optimum axial position of the cut-off knife edge. The remote control of this position has proven to be indispensable in attainment of a useful image through the Mach and temperature range of the tunnel.

Another distinguishing feature is the provision for scanning the 18-inch diameter area of the test section windows with the 12-inch diameter light path. This is accomplished vertically and horizontally in 2-inch increments by crossfeed controls and simultaneous support leg extensions.

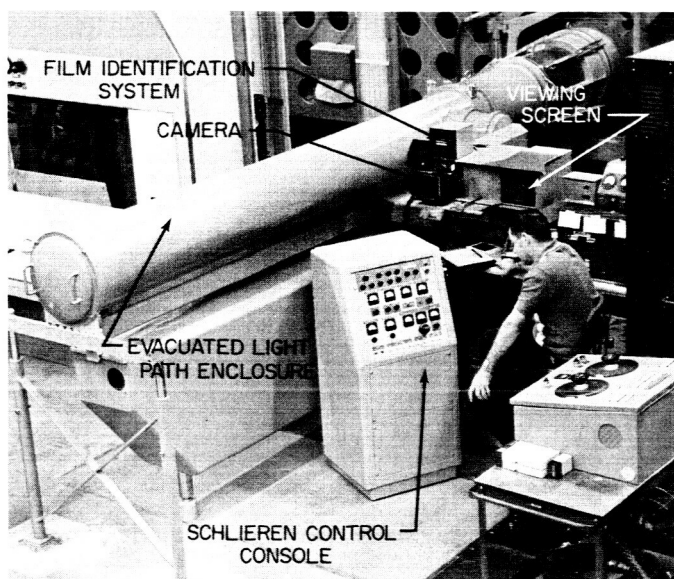


Figure 61. Schlieren system for hypersonic wind tunnel

A choice of Newtonian or Herschellian arrangements of the optical system is also available (Fig 62). In the former arrangement, the two spherical mirrors share a common optical axis. A small decrease in coma may be realized over the Herschellian system, but is offset by the appearance on the viewing screen of the 3-inch diameter flat mirrors used to introduce the light source and exit the image. The Herschellian arrangement is the more familiar z -system that produces an unobstructed light path.

The arrangement of the optical components is shown in Figure 62. The light source consists of an air-cooled mercury vapor BH-6 bulb operating in a horizontal position in a water-cooled housing. Bulb position adjustments are provided for all directions of translation and rotation. The light path rises vertically from the bulb, passes through a quartz disk, and is directed horizontally by a 45-degree front-surfaced mirror through a coated quartz disk into the evacuated enclosure. Rotation of the bulb in a horizontal plane thereby produces rotation in a vertical plane about the system axis during the synchronous rotation process previously mentioned. The light path continues through two 8-inch focal length achromatic condensing lenses, and the bulb image is formed at the slit. This point also coincides with the focal point of the first 12-inch spherical mirror. Nominal slit width used is 0.005 inch. Behind the slit is the slit length device consisting of a rotating disk with a slot of uniformly decreasing width extending around the axis of the disk. The small flat mirror now directs the diverging light path to the first spherical mirror which it leaves as parallel light and passes through the wind tunnel test section air flow and windows to the second spherical mirror. Convergence to the original image takes place at the cut-off knife edge after being redirected by another small flat mirror. Beyond this point, the light passes out of the evacuated enclosure through another coated quartz disk. A front-surface mirror directs the light into a 42-inch focal length f -14 Goerz Artar apochromatic lens. A sequence controlled mirror here directs the light through a negative lens to a 7.5-inch-diameter viewing screen, or to the 4×5 -inch film plane through a Graflex focal plane shutter during the photographic sequence.

Between the shutter and the film plane, and in a corner of the film area, is a 45-degree mirror for transmission of identification data to the film. The identification unit displays a tunnel identity number, the test, run, point, and classification required. The information is presented by rear projection, and the unit contains its own lens, iris, shutter, and exposure control. Functioning is automatic during the photographic sequence and includes two pre-selected exposure times. One is for film used with the

BH-6 light source, and one for film used with the spark source.

The spark source, operating at 7 kv, is located below the system axis between the slit and the first flat mirror. The 0.036-inch-diameter spark image is brought into the optical axis by a small flip-in mirror during the spark photography sequence. The spark orifice is then at the focal point of the first spherical mirror. At the same time, the slit length device moves to zero, thereby completely blocking the BH-6 light. This action is necessary because spark photographs are made by the open flash method where the focal plane shutter momentarily exposes the entire area to the 1-millisecond spark duration. Fogging would result if the BH-6 light were not eliminated.

A light-intensity measuring system assures uniform exposure for photographs made with the BH-6 light source. The light is sampled by a photocell mounted on the first spherical mirror and is read in lumens per square foot on the control panel. Thus, the light measured is affected by the BH-6 output, the slit length and width, but not the cut-off knife edge. This arrangement leaves the cut-off free to control sensitivity, and provides compensation for variation and degradation of light output through the life of each BH-6 bulb.

The photographic sequence, once selected and initiated, is completely automatic. Control panel adjustments are drawn from standardized procedures and operator experience. Change between BH-6 and spark source sequences is accomplished with a single switch. Types of photographs include the following:

- (a) Schlieren, using the BH-6 with system orientation variable from 0 to 180 degrees.
- (b) Schlieren, using the spark source, with similar angular range of the cut-off knife edge only.
- (c) Shadowgraph, using the spark source; 8×10 Super Hypan film may be placed at the test section window for a full-size image of the model and shock pattern, if desired.
- (d) Motion pictures, at normal or high speeds, using the BH-6 and covering all or part of the field.

A Polaroid sheet film back with Polaroid type 52 film has proved useful for proof photos with the BH-6 light source. A Polaroid roll film adapter containing Polaroid 3000 film is used to establish optimum cut-off knife edge setting for spark pictures under various conditions.

Functioning of the system has been highly satisfactory. Wind tunnel tests for JPL projects and outside contractors have utilized the system continuously since its installation. Continued optimization and experience should improve the visualization and recording of flow fields at the very low static pressure levels of the hypersonic tunnel.

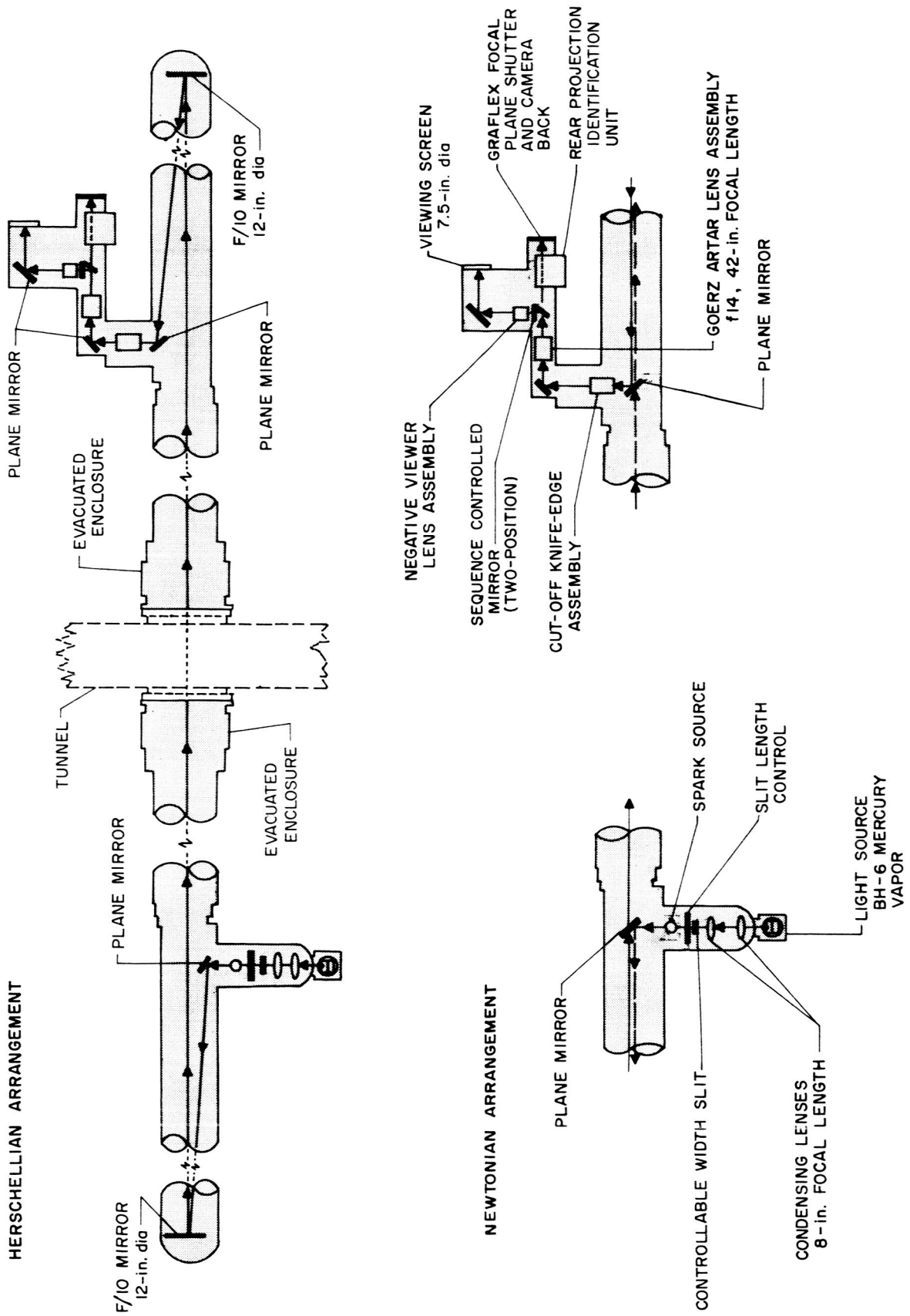
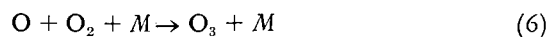
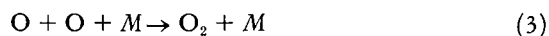
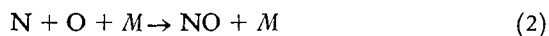
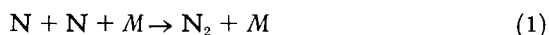


Figure 62. Arrangement of optical components

IX. PHYSICS RESEARCH

A. Upper Atmosphere Reactions

The Earth's upper atmosphere contains oxygen and nitrogen atoms as well as the molecular gases found at sea level. As a prelude to a laboratory program of measuring the three-body recombination rates of these atoms, an analysis of all the interactions between nitrogen-oxygen atoms and molecules has been made with the aid of the IBM 704 digital computer. The following equations describe the major reactions between these species:



where chemical nomenclature is used for the various atoms and molecules, and the symbol M represents any species acting as a third body. The differential equations

governing the rates of change of the concentrations of the five species involved are:

$$-\dot{X} = 2AX^2 + BXY + DXZ + EXW \quad (8)$$

$$-\dot{Y} = BXY + 2CY^2 - DXZ - EXW + FYW + GYU \quad (9)$$

$$-\dot{Z} = -BXY + DXZ - EXW \quad (10)$$

$$-\dot{W} = -CY^2 + EXW + FYW - 2GYU \quad (11)$$

$$-\dot{U} = -FYW + GYU \quad (12)$$

where the algebraic symbols X , Y , Z , W , and U represent atomic nitrogen, atomic oxygen, nitric oxide, molecular oxygen, and ozone, respectively, and the symbols A through G represent the rate coefficients of the seven chemical reactions involved. The laboratory experiment is planned to measure the rate coefficients C and B for the three-body recombinations of atomic oxygen (Reaction 3) and of atomic oxygen with atomic nitrogen (Reaction 2).

For the computer program, these coefficients have been estimated while the remaining coefficients have been taken from the literature (Refs 27 to 31).

The purpose of the computer analysis was (1) to obtain a physical understanding of the net effect of the seven

simultaneous reactions so that the laboratory experiment may be best designed to measure the desired rate coefficients, and (2) to determine the relative importance of each reaction so that approximate analytical solutions may be found to the different equations. The equations were numerically integrated with the following initial conditions: pressure, 6 mm Hg; atomic oxygen concentration, approximately 1%; atomic nitrogen concentration, approximately 0.1%; nitric oxide concentration, approximately 0.0001%; and zero molecular oxygen and ozone concentrations. The integration was carried out from 0 to 1 second reaction time. The results are plotted in Figures 63 and 64.

Figure 63 shows the reaction rates of each of the seven reactions, and Figure 64 shows the change of concentrations of each of the species involved. An examination of these data indicates that the last three reactions (FXW, FYW, and GYU) may be ignored and 1% accuracy will still be valid for the times and pressure considered here. Although Z is not equal to zero, the term BXY is almost equal to DXZ under all conditions. Physically, this means that Reaction 4 rapidly consumes the nitric oxide formed in Reaction 2 and attempts to maintain an equilibrium where the NO concentration would be constant. However, Reaction 3 is slowly consuming oxygen atoms and, hence, removing them from this cycle which causes the NO concentration to slowly decrease. In Figure 64, it may be seen that the changing concentrations of nitric oxide follow the atomic oxygen concentration. If one uses the

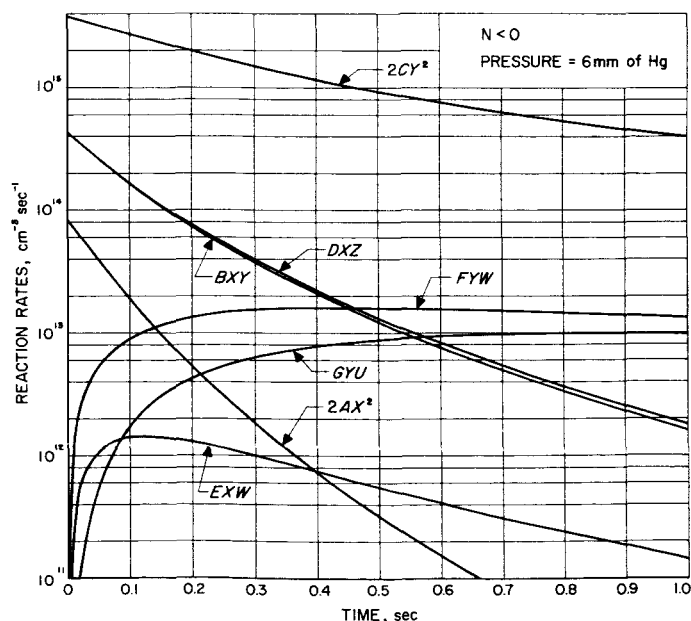


Figure 63. Change of reaction rates with time

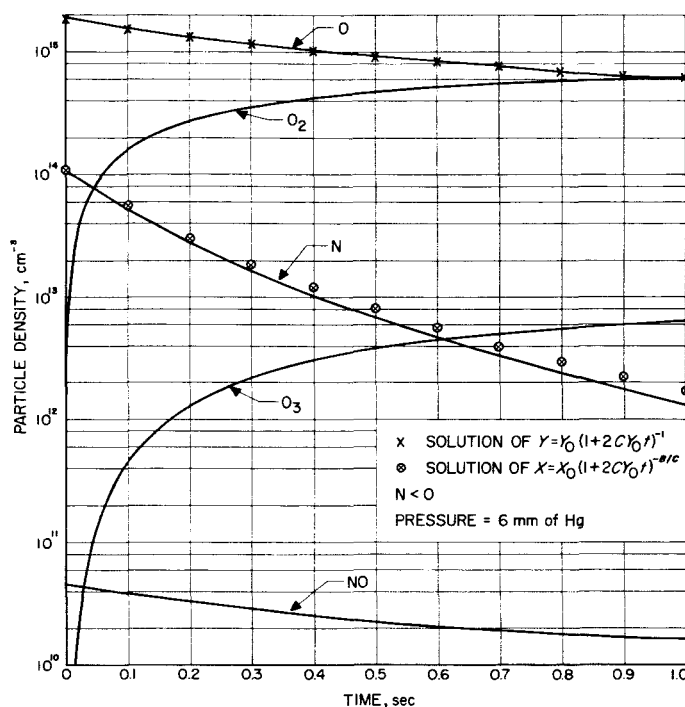


Figure 64. Change of particle densities with time

approximation that $BXY \approx DXZ$, then the differential equation for \dot{Y} becomes:

$$-\dot{Y} = 2CY^2$$

which may be integrated to

$$Y = Y_0(1 + 2CY_0t)^{-1}$$

where Y_0 is the initial concentration, and t the time. Solutions of this equation, for atomic oxygen concentration are plotted in Figure 64. It may be seen that the analytical solution agrees well with the computer solution. Applying the $BXY \approx DXZ$ approximation to the differential equation for \dot{X} gives:

$$-\dot{X} = 2AX^2 + 2BXY$$

For the physical conditions considered here, $2AX^2$ is initially less than one-tenth of $2BXY$ and becomes progressively smaller. The solution to the equation

$$-\dot{X} = 2BXY$$

is

$$X = X_0(1 + 2CY_0t)^{-B/C}$$

Solutions of this latter equation are also plotted in Figure 64. It may be seen that the deviation of solutions of this equation from the computer-calculated atomic nitrogen concentration increases as the reaction time increases.

In summary, a useful analytical solution has been found which may be used to determine C , the three-body

atomic oxygen recombination rate coefficient. The analytical solution for B , the three-body atomic nitrogen-atomic oxygen recombination rate coefficient, is not satisfactory for the accuracy desired and, hence, a computer calculation is necessary for an accurate solution. However, the approximate solution is useful in programming the computer to more quickly find the correct solution.

B. Efficiency of Fission Electric Cell

Work is in progress at a number of laboratories on the problem of direct production of electricity from fission in a nuclear reactor without use of a thermodynamic cycle, aiming toward development of a light-weight spacecraft power supply.

One concept which has been advanced for this purpose is the use of the charged fission fragments themselves to provide the electrical energy. A simplified version of such a fission electric cell is shown in Figure 65. Two metal plates are separated by a vacuum gap large enough to prevent voltage breakdown between the plates. On the upper surface of the lower plate is a layer of fissionable material. The cell is within, or may constitute one fuel element of, a nuclear reactor. As neutrons penetrate the fuel layer on the lower plate, they cause fission to occur, normally creating two high-energy charged fragments per nucleus split. These fragments have an average energy of 80 mev each and have a positive charge equal in magnitude to about 20 electron charges. Half of the fragments will start out in the direction of the upper half plane, the others being lost in the fuel layer backing

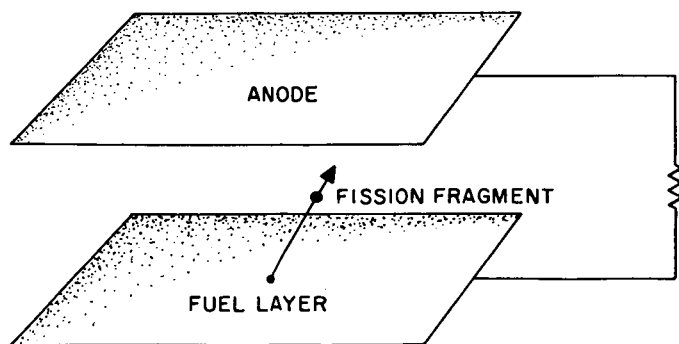


Figure 65. Fission electric cell

plate. The range of these fragments is very short, on the order of 13 microns in uranium, so a significant fraction will penetrate to the vacuum gap only if the layer is extremely thin. Those which reach and cross the gap will create a positive charge on the upper plate, and a net negative charge on the lower; in effect charging the cell as a condenser. The maximum potential which can be created by the fragments is approximately $80/20 = 4$ mev. Steady-state operation at any lower potential can be achieved by connecting to an external load, as shown in Figure 65, matched to the internal current flow of fission fragments.

The first measure of the practicality of such a device is its electrical efficiency; that is, the fraction of total fission power converted to electrical power. This efficiency must be comparable to that achieved by thermoelectric or thermionic converters used in conjunction with nuclear reactors, or the concept will not be competitive in spacecraft power applications. If its efficiency should prove to be as good, it would be an extremely desirable system, since the electrical power output can be had directly from the reactor at a high voltage, in contrast to the low voltage of thermoelectric and thermionic devices.

As a first step in evaluating the possibilities of the fission electric cell concept, calculations have been carried out on the electrical efficiencies as a function of voltage and fuel thickness for plane, concentric cylinder, and concentric sphere electrodes. The efficiency can be defined as

$$\epsilon = \frac{Ve'\eta}{\tau NE'}$$

where V is the steady-state voltage between plates, e' the charge per fission fragment transferred to the anode, η the number of fragments per second reaching the anode per unit area of fuel surface, τ the fuel layer thickness, N the number of fission fragments produced per second per unit volume of fuel, and E' the fission energy released per fragment. As can be seen from the definition, η is proportional to N . Thus the inherent cell efficiency is not dependent upon N , which is a function of neutron flux, atomic density, and fission cross section of the fuel material. The other quantities which enter into ϵ , or at least their average values, are known; therefore, it is necessary only to calculate η in order to obtain ϵ .

The calculations now being completed are based upon several simplifying assumptions: (1) All fragments are assumed to have the same mass, the same constant charge, and equal starting energy. (2) All fragments are assumed to be emitted isotropically, at a constant rate for all

locations in the fuel layer. (3) The energy of a fragment traversing fuel material is taken to be $E = E_0 [1 - r/\lambda]$; where E_0 is initial energy, r the distance traversed, and λ the total (constant) range. (4) Curvature of the fuel layer in cylindrical and spherical cases is ignored. (5) Plane and cylindrical elements are treated as if infinite in extent. The calculation of η then consists simply of an integration:

$$\eta = N \int_{\text{fuel layer}} P_1 P_2 P_3 dv$$

where P_1 is the probability of a fission fragment from volume element dv in the fuel layer starting out in the direction of a particular unit area of the surface (based on isotropic emission), P_2 is the probability of the fragment reaching the surface (based on the linear energy loss assumption), and P_3 is the probability of the fragment crossing the vacuum gap to the anode against the opposing potential V after having reached the layer surface. With the P 's expressed in a coordinate system appropriate to the particular geometry being considered, integration is carried out over the fuel layer of thickness τ as if it were flat and infinite in extent. Analytical solutions have been obtained for the plane and spherical cases, but do not appear possible for the cylindrical. An IBM 704 computer program has been prepared to compute ϵ utilizing a numerical integration; it is now being used for all cases.

The initial and boundary conditions are

$$\begin{aligned} \text{At } t = 0 \quad & V_\phi = 0 \\ & J_r = \frac{I}{2\pi r} \quad \text{for } 0 < Z < L \\ & = 0 \quad \text{at } Z = 0, Z = L \\ \text{At } Z = 0, Z = L \quad & V_\phi = 0 \\ & T_r = 0 \\ \text{At } r = r_1 \quad & V_\phi = 0 \\ & J_r = \frac{I}{2\pi r_1} \quad \text{for } 0 < Z < L \\ & = 0 \quad \text{at } t = 0 \text{ and } Z = L \\ \text{At } r = r_2 \quad & V_\phi = 0 \\ & J_1 = \frac{I}{2\pi r_2} \quad \text{for } 0 < Z < L \\ & = 0 \quad \text{at } Z = 0 \text{ and } Z = L \end{aligned}$$

where I is the total current per unit length of the electrode.

The equations are written in terms of cylindrical coordinates. The idealized model of the rotating plasma used in these calculations is shown in Figure 66 in which the coordinate system is also described.

The solutions for J_r and V_ϕ are eventually expressed by eigen-function expansions; thus,

$$\begin{aligned} V_\phi = & \sum_s \sum_n 4 \frac{\pi^2}{d} \frac{\lambda_s^2 J_1^2(\lambda_s)}{J_1^2(\lambda_s k) - J_1^2(\lambda_s)} \frac{P_h \psi(\lambda_s k)}{n} \\ & \times \left\{ \frac{G_{ns}}{\alpha_{ns}} [1 - e^{-(\phi_{ns} + \beta_{ns})\tau}] + \frac{1}{\beta_{ns} P_{ms}} e^{-\phi_{ns}\tau} \sinh \beta_{ns}\tau \right\} \\ & \times [J_1(\lambda_s \rho) Y_1(\lambda_s) - J_1(\lambda_s) Y_1(\lambda_s \rho)] \sin \frac{n\pi s}{d} \end{aligned}$$

C. Physics of Rotating Plasmas

1. Theoretical Study

The analytical study of a rotating plasma was first given by Chang and Lundgren in a University of California Radiation Laboratory research report. The solutions of the velocity and magnetic field distributions were found by relaxing the non-slip boundary conditions of the plasma at the surface of the two cylindrical electrodes. The present theoretical investigation attempts to give a more exact solution. The differential equations which have been used are the following:

$$\begin{aligned} \mu_r \frac{\partial J_r}{\partial t} - \frac{1}{\sigma} \left[\frac{\partial^2 J_r}{\partial Z^2} + \frac{\partial^2 J_r}{\partial r^2} + \frac{1}{r} \frac{\partial J_r}{\partial r} - \frac{J_r}{r^2} \right] &= -B_0 \frac{\partial^2 V_\phi}{\partial Z^2} \\ \frac{\partial V_\phi}{\partial t} - v \left[\frac{\partial^2 V_\phi}{\partial Z^2} + \frac{\partial^2 V_\phi}{\partial r^2} + \frac{1}{r} \frac{\partial V_\phi}{\partial r} - \frac{V_\phi}{r^2} \right] &= -B_0 J_r \end{aligned}$$

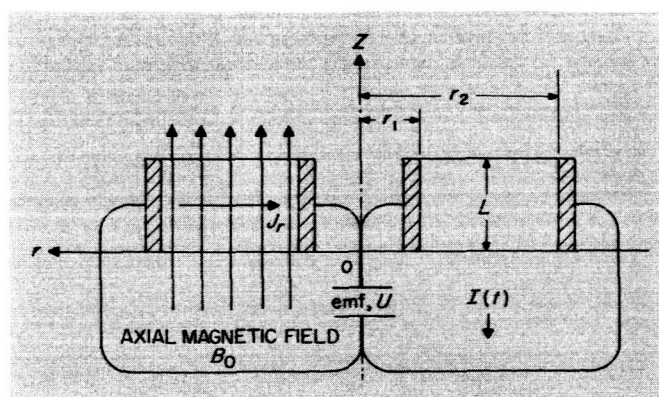


Figure 66. Rotating plasma experimental setup

$$\begin{aligned}
J_r = (J_r)_{t=0} + \sum_s \sum_n 4 \frac{\pi^2}{d} \frac{\lambda_s^2 J_1^2(\lambda_s)}{J_1^2(\lambda_s k) - J_1^2(\lambda_s)} \\
\times \frac{P_h \psi(\lambda_s k) G_n}{n \alpha_{ns}} \left(\frac{n\pi}{d} \right)^2 [J_1(\lambda_s \rho) Y_1(\lambda_s) \\
- J_1(\lambda_s) Y_1(\lambda_s \rho)] \sin \frac{n\pi z}{d} [1 - e^{-(\phi_{ns} + \beta_{ns}) \tau}]
\end{aligned}$$

These results were obtained on the assumption that

$$\mu_e \sigma v [P_h] < 0.1$$

$[P_h]$ is a physical parameter equivalent to the square of Hartmann number

$$[P_h] = \frac{\sigma B_0^2 r_1^2}{\rho v}$$

In most practical cases, this condition is valid.

Numerical computations of the above results are under-way. Of considerable interest will be the comparison of the analytical results with experimental observations now being conducted (see Part 2). A more realistic model with time dependent conductivity and total current I is also under study and will be published in a later Summary.

2. Rotating Plasma Experiment

Orthogonal electric and magnetic fields are applied to an ionized gas in order to induce a drift motion of both ions and electrons in the azimuthal direction. A schematic diagram of the experimental setup is shown in Figure 66.

A system of concentric electrodes, placed in the center of a 2-foot-long Pyrex glass tube of 4-inch-ID, carries a radial discharge current I_r . Simultaneously, a solenoid around the Pyrex tube generates a uniform axial magnetic field B_0 which accelerates the gas by Lorentz forces in the azimuthal direction. Two removable walls are available to seal the sides of the discharge section of the tube and can be used to obtain experimental checks of the boundary conditions assumed in the theory. The emphasis in this experiment is placed on the study of the basic properties of a rotating plasma confined in an annular tube

of rectangular cross section; later, magnetic mirror fields will be applied to confine the plasma. Argon is used for this experiment. The device operates at the comparatively high pressure levels of 50 to 100 μ in order to escape any anode sheath effects.

The peak value of the radial discharge current ranges approximately from 25,000 to 50,000 amperes, and is reached after 5 to 10 microsec. The axial magnetic field B_0 in the solenoid, also generated by discharging a capacitor bank (2200 μ f/3000 v), reaches its peak values of 10,000 to 20,000 gauss in several hundreds of microseconds. To prevent the magnetic field B_0 from oscillating, the circuit shown in Figure 67 is employed. The axial magnetic field B_0 obtained this way rises to a peak value and from thereon decays very slowly in time. The radial discharge current I_r is triggered a few microseconds before B_0 has reached its peak. Thus, both peaks coincide, which results in maximum acceleration of the ionized gas. During the period of the radial discharge current (10 to 20 μ sec) the pulsed axial magnetic field remains practically constant, lasting for some 300 μ sec.

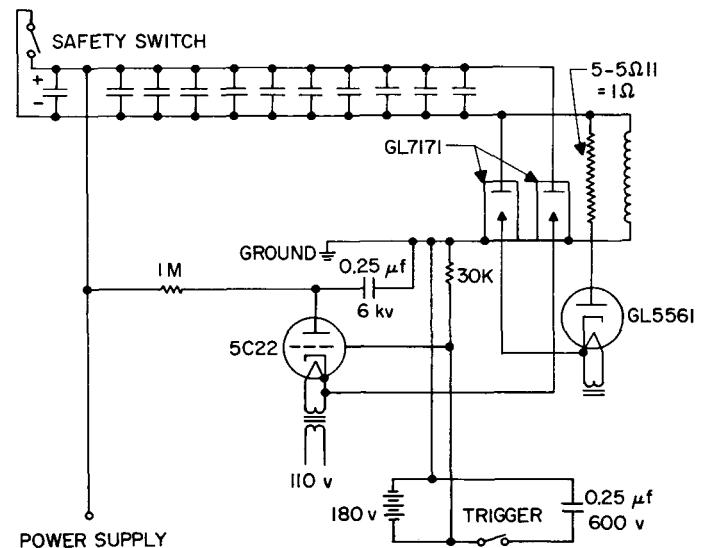


Figure 67. Circuit used to prevent magnetic field oscillations

References

1. Stiefel, E., *Numerische Mathematik*, Band 1, pp. 1-28, Springer Verlag, Berlin, 1959.
2. Skaupy, F., "Über die Carbide des Wolframs und ihre Anwendung," *Zeitschrift für Elektrochemie*, 33:487, 1927.
3. Becker, K., "Die Konstitution der Wolfram Carbide," *Zeitschrift für Electrochemie*, 34:640, 1928.
4. Becker, K., "Über das System Wolfram-Kohlenstoff," *Zeitschrift für Metalkunde*, 20:437, 1928.
5. Neel, L., "Directional Order and Diffusion Aftereffect," *Journal of Applied Physics*, Suppl to 30(4):3s-8s, April, 1959.
6. Martens, H. E., Jaffe, L. D., and Jepson, J. E., *High-Temperature Tensile Properties of Graphite*, Progress Report No. 20-326, Jet Propulsion Laboratory, Pasadena, September 30, 1957.
7. Ferry, J. D., "Mechanical Properties of Substances of High Molecular Weight. VI. Dispersion in Concentrated Polymer Solutions and its Dependence on Temperature and Concentration," *Journal of the American Chemical Society*, 72:3746-3752, 1950.
8. Stuart, H. A., *Die Physik der Hochpolymeren*, Ed., Springer-Verlag, 1956, p. 56 et seq. in Chap. 1 by A. J. Staverman and F. Schwarzl, and Chap. 6 by J. D. Ferry.
9. Mason, P., *Journal of Applied Polymer Science*, 1:63, 1959; *Transactions of the Faraday Society*, 440:1461, 1959.
10. Landel, R. F., Stedry, P. J., and Smith, T. L., *18th Meeting Bulletin Joint Army-Navy-Air Force Panel on Physical Properties of Solid Propellants*, p. 127, Solid Propellant Information Agency, Applied Physics Laboratory, Johns Hopkins University, Silver Spring, Maryland, June 1959 (Confidential); also Publication No. 30-2, Jet Propulsion Laboratory, April 29, 1959 (Confidential).
11. Martin, G. M., Roth, F. L., and Stiehler, R. D., *Transactions of the Institute of Rubber Industry*, 32:189, 1956.
12. Smith, T. L., "Dependence of the Ultimate Properties of a GR-S Rubber on Strain Rate and Temperature," *Journal of Polymer Science*, 32:99, 1958.
13. Williams, M. L., Landel, R. F., and Ferry, J. D., *Journal of the American Chemical Society*, 77:3701, 1955.
14. *Thrust Vector Control by Secondary Injection*, NOTS IDP 765, Naval Ordnance Test Station, September 14, 1959 (Confidential).
15. Rupe, J. H., *Bridging the Gap Between Injector Hydraulics and Combustion Phenomena in Liquid Propellant Rocket Engines*, Jet Propulsion Laboratory, Pasadena, September 17, 1959.
16. Rupe, J. H., *A Correlation Between the Dynamic Properties of a Pair of Impinging Streams and the Uniformity of Mixture-Ratio Distribution*, Progress Report No. 20-209, Jet Propulsion Laboratory, Pasadena, March 28, 1956.
17. Elverum, G. W., and Martinez, J. S., *Results of Performance Calculations for N_2O_4 - N_2H_4 Bipropellant System*, Memorandum No. 20-174, Jet Propulsion Laboratory, Pasadena, July 3, 1958.
18. Elverum, G. W., and Staudhamner, P., *The Effect of Rapid Liquid-Phase Reactions on Injector Design and Combustion in Rocket Motors*, Progress Report No. 30-4, Jet Propulsion Laboratory, Pasadena, August 25, 1959.
19. Lee, D. H., et al, *A Monopropellant-Hydrazine Thrust Unit for Velocity Control of Extraterrestrial Vehicles*, Memorandum No. 30-161, Jet Propulsion Laboratory, Pasadena, February 3, 1958 (Confidential).
20. Bartz, D. R., "A Simple Equation for Rapid Estimation of Rocket Nozzle Convective Heat-Transfer Coefficients," *Jet Propulsion*, 27:49-51, January 1957.
21. Laufer, J., and Vrebalovich, T., *Stability of a Supersonic Laminar Boundary Layer on a Flat Plate*, Report No. 20-116, Jet Propulsion Laboratory, Pasadena, December 1958.
22. Lees, L., and Lin, C. C., *Investigation of the Stability of the Laminar Boundary Layer in a Compressible Fluid*, Technical Note No. 1115, National Advisory Committee for Aeronautics, Washington, D. C., September 1946.
23. Dunn, D. W., and Lin, C. C., "On the Stability of the Laminar Boundary Layer in a Compressible Fluid," *Journal of the Aeronautical Sciences*, 22:455-477, July 1955.
24. Reshotko, E., *Stability of the Compressible Laminar Boundary Layer*, Ph. D. Thesis, California Institute of Technology, Pasadena, 1960.
25. Mack, L. M., *Numerical Calculation of the Stability of the Compressible Laminar Boundary Layer*, Report No. 20-122, Jet Propulsion Laboratory, Pasadena, April 1960.

26. Menkes, J., *Stability of One-Dimensional Flow of a Real Continuous Fluid*, Technical Release No. 34-50, Jet Propulsion Laboratory, Pasadena, June 1, 1960.
27. Harteck, P., et al, "Rate of Recombination of Nitrogen Atoms," *Journal of Chemical Physics*, 29:608-610, 1958.
28. Reeves, R. R., et al, "Rate of Recombination of Oxygen Atoms," *Journal of Chemical Physics*, 32:632, 1960.
29. Kistiakowsky, G. B., and Volpi, "Reactions of Nitrogen Atoms. I. Oxygen and Oxides of Nitrogen," *Journal of Chemical Physics*, 27:1141-1149, 1957.
30. Kistiakowsky, G. B., and Volpi, "Reactions of Nitrogen Atoms. II. H_2 , CO, NH_3 , NO, and NO_2 ," *Journal of Chemical Physics*, 28:665-668, 1958.
31. Benson, S. W., and Axworthy, A. E., "Mechanism of the Gas Phase, Thermal Decomposition of Ozone," *Journal of Chemical Physics*, 26:1718-1726, 1957.